Next generation biophotonics technologies for clinical applications in detecting Gastric cancer: A comprehensive review.

Jodie Chuan Yue Foo[1,#], Rabia'tul A'dawiah[1,#], Keertana Vinod Ram[1], Nuraini Zailani[2], Derrick Yong[1,2], Jayakumar Perumal[1,*], Malini Olivo[1,*], U. S. Dinish [1,*]

[1]Translational Biophotonics Laboratory, A*STAR Skin Research Labs (A*SRL), Agency for Science, Technology and Research (A*STAR), 31 Biopolis Way, #07-01, Nanos, Singapore 138669, Republic of Singapore.

[2] Endofotonics Pte Ltd, Singapore

*Correspondence: Jayakumar_Perumal@asrl.a-star.edu.sg; Malini_Olivo@asrl.a-star.edu.sg; Dinish@asrl.a-star.edu.sg

[#]These authors contribute equally to this work.

Abstract

Gastric cancer (GC) is a major pressing global health issue as it ranks as the fifth most common cancer and resulted in around 769,000 fatalities globally in 2020. This comprehensive review centers on the progress in biophotonics technologies for early detection of GC over the last decade, aiming to address the constraints posed by traditional endoscopic tools and proteomics analytical methods for the detection. Herein, an array of diverse techniques such as, narrow band imaging, confocal laser endomicroscopy, Raman spectroscopy, surface enhanced Raman spectroscopy, Fourier transform infrared spectroscopy, diffuse reflectance spectroscopy, fluorescence spectroscopy, optical coherence tomography, polarization optical spectroscopy and other technologies are reviewed and their relative merits and demerits for GC detection and diagnosis are provided by comparing their sensitivity, ease of use, and methodology in operation. This paper explores the advancements and future perspectives of technical improvements needed in biophotonics technologies for the early detection of GC. Through interdisciplinary collaboration and validation studies, we envision that biophotonics technologies could achieve the full spectrum of benefits for all the stake holders. We anticipate that this will bring about a significant improvement in early detection of GC with the potential for widespread clinical adoption.

1. Introduction

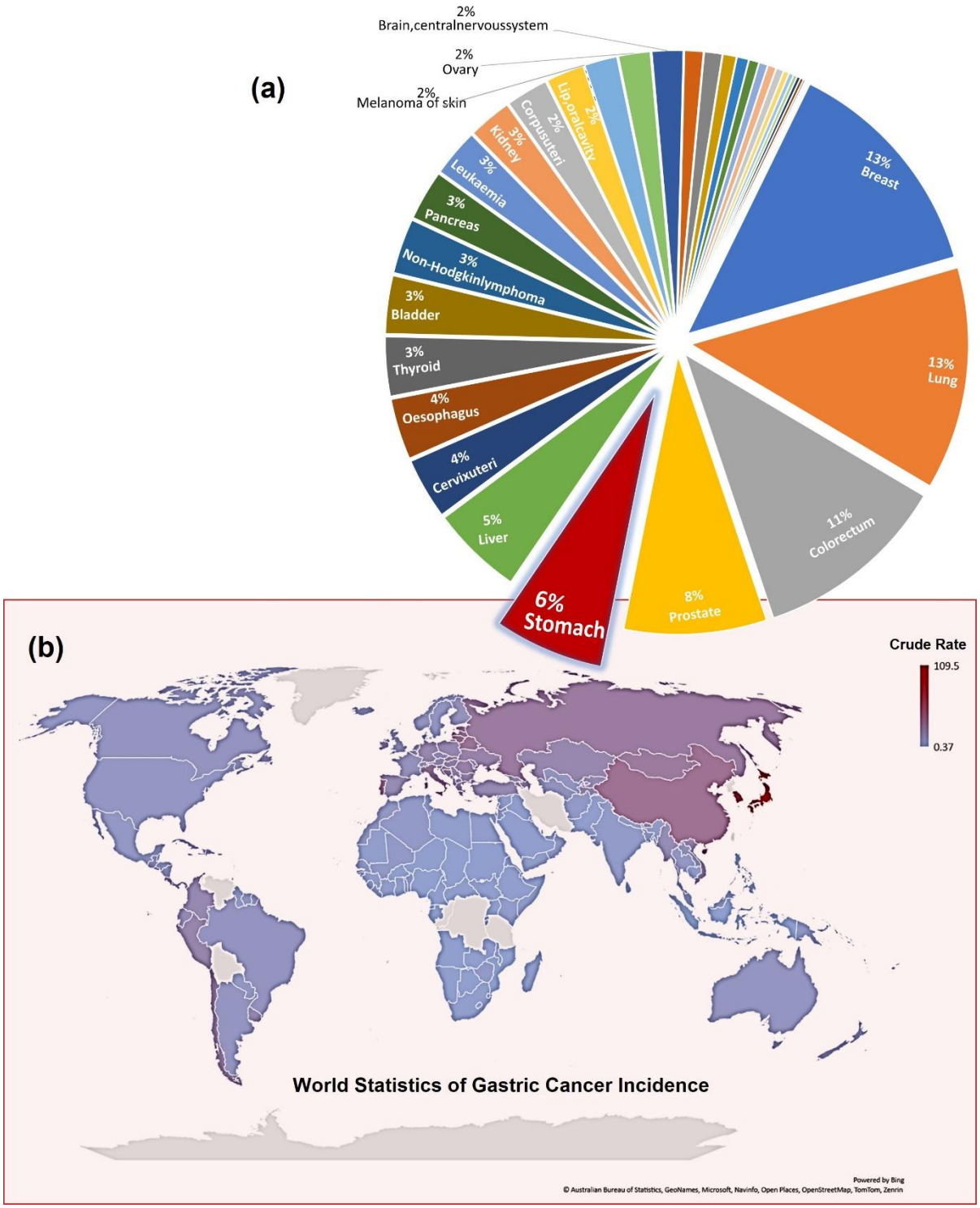

Figure 1. a) Pie Chart depicting the prevalence landscape of various cancers as of 2020 worldwide. b) Incidence of stomach cancer in the world represented based on the crude rate which gives the overview of disease burden in a particular population as of 2020. CRUDE RATE = (Number of cases/ Total population at risk) *100000. [1] IARC International Agency for Research on Cancer. Global Cancer Observatory. Available online: https://gco.iarc.fr/ (accessed on 22 November 2023)

Gastric cancer (GC), often known as stomach cancer, continues to be a prevalent and global health concern. In 2020, it stood as the fifth most common malignancy and fourth for mortality worldwide, causing approximately 769,000 fatalities. [2,3] Notably, as seen in **Figure 1a**, GC accounted for 6% of newly diagnosed cancer cases globally in 2020, further emphasizing it as a substantial health concern. Furthermore, Japanese males exhibit the highest incidence rates, showcasing the critical need for vigilant surveillance and effective mitigation strategies. [4] This noteworthy trend is depicted in **Figure 1b**, where Eastern Japan and Europe displayed higher prevalence of GC. [1] Detecting early GC can pose challenges since it frequently manifests with subtle or nonspecific symptoms, causing delayed diagnosis. Consequently, most patients are diagnosed in advanced stages, which contributes to elevated mortality rates.

The prevalence of this disease is further underscored by a troubling surge in incidence, particularly among younger populations, emphasizing the pressing need for early detection, precise diagnosis, and tailored treatment strategies. Recognizing the critical role of early detection in improving GC patient survival rates, research in South Korea demonstrates a significant enhancement in the five-year survival rate, rising from 46% to 75% with the implementation of a biennial screening program. [5] Notably, South Korea and Japan exhibit five-year survival rates exceeding 60%, in stark contrast to Western Europe and the United States, where advanced-stage diagnoses result in a mere 30% survival rate. Globally, early detection shows promise for reducing GC mortality by 30-65%. [6] The notable disparities in survival rates underscore the crucial importance of early detection and diagnosis in addressing the impact of GC.

At present, upper gastrointestinal endoscopy and endoscopic biopsy serves as the established gold standard for diagnosing GC. [7,8] Endoscopy relies on the principles of light reflectance, fluorescence, and light absorption. The endoscope's light source illuminates' internal structures, utilizing reflected light for surface characteristics, fluorescence for enhanced visualization with and without contrast agents, and absorption for differentiation based on endogenous tissue characteristics. These principles collectively contribute to the creation of detailed images, facilitating the identification of abnormalities and neoplastic changes within the digestive tract. The continuous evolution of technology in this mature field has led to remarkable advancements in endoscopic imaging, enabling enhanced visualization of subtle abnormalities and early-stage lesions. More advanced techniques such as magnifying narrow-band imaging (M-NBI) [9–18], blue-light imaging [19–24], and chromoendoscopy [25–29] have significantly improved the diagnostic precision of endoscopy by providing detailed views of the mucosal surface, vascular patterns, and contrast-enhanced images. In addition, there is a growing emphasis on the integration of artificial intelligence (AI) [13,14,30–36] algorithms in endoscopic procedures. Incorporating AI holds promise for real-time analysis and automated detection of suspicious lesions, potentially reducing the invasiveness of procedures and enhancing diagnostic accuracy. This transformative approach not only augments the capabilities of endoscopists but also opens avenues for improved

efficiency and accessibility in diagnosing GC. However, despite these promising developments, endoscopy is not without its inherent disadvantages, including invasiveness, patient discomfort, and the risk of complications. The invasiveness and cost associated with such methods present formidable challenges for the implementation of routine screening, necessitating the exploration of alternative approaches.

Other clinical approaches involve the detection for blood tumor markers such as carcinoembryonic antigen (CEA), carbohydrate antigen (CA19-9) and carbohydrate antigen 72-4 (CA72-4), which have shown potential as being markers for GC. [37,38] Yet, none of them demonstrate high levels of diagnostic accuracy, specificity, and sensitivity. Imaging modalities used for GC detection includes double contrast barium x-ray, computed tomography and magnetic resonance imaging. [39–41] Due to their low sensitivity and high cost, it proves to be difficult for early diagnosis. [42,43] While these techniques have significantly contributed to our understanding, detection and ultimately GC diagnosis, they remain marred by inherent limitations such as limited sensitivity, and accuracy. [40,44,45] These limitations can render them less effective in early-stage cancer diagnosis, especially when dealing with visually elusive, non-localized, or small tumors. Consequently, this hinders timely detection, which is crucial for optimizing patient prognosis.

To detect GC in its early stages, numerous comprehensive studies have been conducted to identify various biomarkers using proteomics techniques in order to gain a deeper insight into underlying mechanisms. [46–49] Despite the valuable insights in advancing diagnostic possibilities gained from proteomics, such studies are often in their preliminary stages. Due to the heterogenous nature of GC, discovery, and validation of its biomarkers for clinical use remain particularly challenging. Additionally, the identification of effective markers is complicated on account of the complexity of biological samples such as in plasma, which is due to its high dynamic range, variability among patients, and the scarcity of sensitive analytical techniques. Although circulating markers hold potential for non-invasive early GC detection, they often fall short when used individually and lack specificity. [50] Significant challenges in routine clinical adoption of proteomic techniques remain in identifying the most promising and reliable protein biomarkers and its cost-effective detection. As a result, there is a pressing need to explore alternative technologies that can address these limitations and offer more robust diagnostic solutions.

To tackle these significant challenges, a transformation pivoting towards innovative and minimally invasive solutions of diagnosing GCs is essential. This shift is embodied in biophotonics technologies, which encompass a diverse array of modalities, ranging from Raman spectroscopy (RS) / surface enhanced Raman spectroscopy (SERS), confocal laser endomicroscopy (CLE), fluorescence spectroscopy, Fourier transform infrared spectroscopy (FTIR), diffuse reflectance spectroscopy (DRS), and optical coherence tomography (OCT) to polarization optical spectroscopy (POS), along with other

techniques like hyperspectral imaging (HSI), terahertz (THz) imaging, surface plasmon resonance (SPR) spectroscopy, and photoacoustic imaging (PAI). These technologies hold significant promise in detecting GC at various stages, including early detection, by offering non-invasive, real-time, and highly precise diagnostic capabilities. In recent years, these technologies have displayed the potential to redefine the landscape of GC detection by offering real-time, non-invasive, cost-effective, and highly precise diagnostic capabilities, thus overcoming the intrinsic shortcomings of traditional approaches.

Biophotonics technologies provide advantages beyond convenience, with precision and real-time capabilities, this enables early lesion detection, informed treatment strategies, and improved patient prognoses. For instance, the utilization of RS allows for molecular-level analysis of tissue composition, providing invaluable insights into cancerous alterations without the destructive aspects of traditional histological methods. Additionally, OCT implemented with endoscopy for non-invasive tissue imaging and characterization, facilitating early detection by providing detailed, cross-sectional images of the gastrointestinal mucosa, and aiding in the identification of potential precancerous lesions. [51] Moreover, these technologies can also be employed in detecting various stages of cancer, including during cancer staging and surgical procedures, thereby enhancing the overall management of the disease.

Furthermore, the detection of tumor cells can be achieved through autofluorescence, a process that involves the emission of light by endogenous fluorophores in response to excitation by light. In some applications, this fluorescence detection is carried out through the biopsy channel of the endoscope, offering a minimally invasive approach to identify cancerous cells. Alongside diagnosis, fluorescence spectroscopy and imaging play crucial roles in accurate tumor marking and lymph node detection during in-vivo procedures such as sentinel node navigation surgery (SNNS) and laparoscopic surgeries. These optical techniques contribute to the precision and effectiveness of surgical interventions, enhancing the overall management of GC patients.

Several recent review articles have focused on GC. Among these, Coda et al. offers a comprehensive overview of biophotonics endoscopy for clinical applications, Liu et al. explore the applications of RS, and Wan et al. on optical spectroscopy in the context of gastrointestinal neoplasms. [52–54] As such, optical technologies transcend the limitations and inconsistencies intrinsic to proteomic detection methods, giving a promising future marked by more dependable and accurate diagnostic results.

While acknowledging the existing literature on GC detection, our review stands out by focusing on the most recent and updated developments, and their implications. By comparing the relative merits and demerits of various biophotonics techniques, including sensitivity, ease of use, and operational methodology, this review provides a nuanced understanding of the current state of these technologies. Importantly, we take a forward-looking approach by highlighting future perspectives on technical advancements and addressing the research gaps that must be filled to transition biophotonics technologies into a routine, label-free, and easily adoptable diagnostic platform. In doing so, this review

contributes not only to the understanding of current technologies but also guides the trajectory of future research and clinical applications in this dynamic field.

2. Biophotonics technologies for GC detection

Among the various biophotonics technologies, some are already used routinely in clinical studies in an in-vivo manner, while others are explored in an in-vitro/ex-vivo mode. This section is categorized into in-vivo and in-vitro/ex-vivo modalities used for the detection of GC.

2.1. In-vivo modalities

2.1.1. Narrow Band Imaging (NBI)

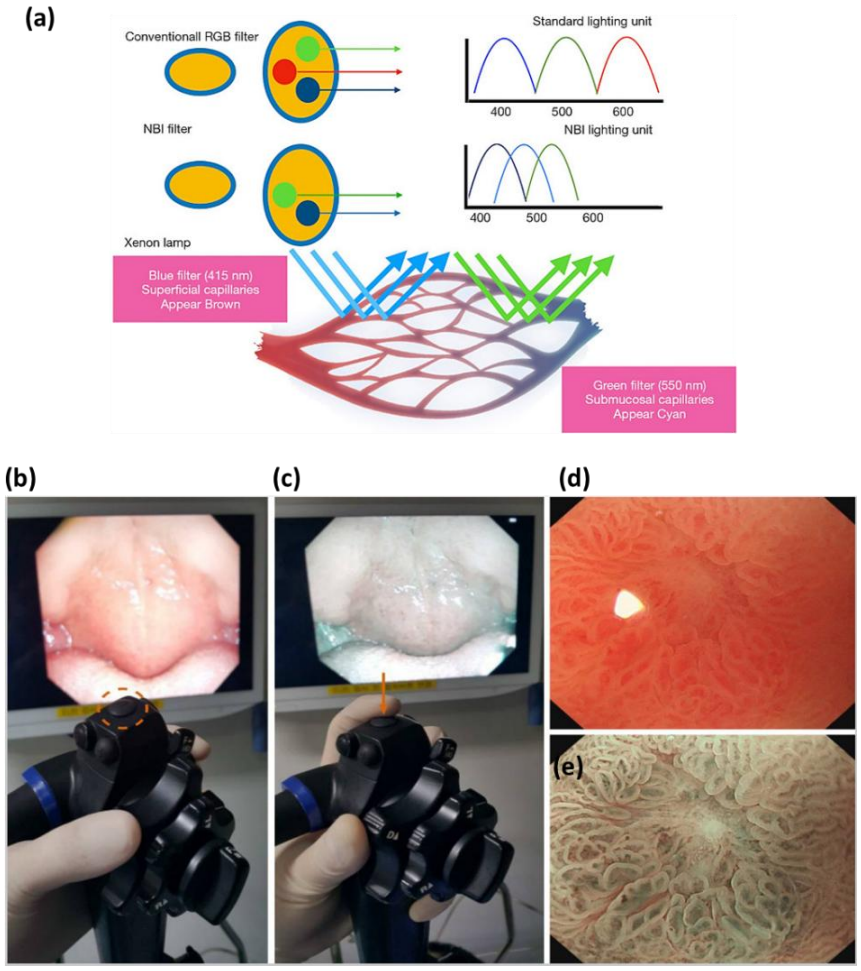

Figure 2. a) The fundamentals of NBI involve using specific blue and green light to highlight blood capillaries in brown and veins in cyan, enhancing contrast with non-vascular structures within the mucosa. *Reproduced with permission under the terms of the CC BY NC-ND 4.0 license.* [55] *Copyright 2022, The Authors published by Pubmed*; (b-e) Comparison of endoscopic images obtained from (b) and (d) conventional white light endoscopy (WLE); (c) and (e) M-NBI mode. (b-e) *Reproduced with permission under the terms of the CC BY NC 4.0 license.* [56] *Copyright 2020, The Authors published by Baishideng Publishing Group Inc*

Endoscopy, acknowledged as the gold standard in GC diagnostics, employs light-tissue interactions to unveil the microstructural intricacies of the gastric mucosa. This mature technology utilizes optical phenomena such as light reflectance and absorption to discern surface characteristics between normal and pathological mucosal entities. Various wavelengths meticulously elucidate subtle alterations in texture and color, offering early indications of potential malignancies. Biochemical probing facilitated by light absorption reveals the molecular composition of gastric tissues, enabling lesion discrimination and early-stage detection.

NBI plays a pivotal role in endoscopic technology optimization, operating on the principles of selective light absorption. It utilizes specific narrow bands of blue (390 – 445 nm) and green (530 – 550 nm) light, capitalizing on the selective absorption properties of hemoglobin to accentuate the contrast between blood vessels and the surrounding mucosa. [57] The heightened contrast enables a detailed examination of mucosal vascular patterns, crucial for identifying subtle changes in color and morphology essential for early-stage gastric lesion detection.

NBI's real-time imaging capabilities, coupled with dynamic adjustment of optical filters and advanced digital processing, contribute to its role as a powerful tool for precision diagnostics. The magnifying capabilities of M-NBI further enhance its diagnostic prowess, allowing for an in-depth visualization of mucosal details and a deeper understanding of microstructural changes. The additive effect of M-NBI has demonstrated benefits, as reported by Horiuchi et al. [12] This approach has proven effective, increasing the possibility of reducing additional surgeries resulting from the misdiagnosis of histological types of GCs. **Figure 2a** illustrates the fundamental concept of NBI imaging and the enhanced contrast in images achieved through the M-NBI mode seen in Figure 2b and d contrasting with conventional white light endoscopy (WLE) observed in Figure 2c and e.

Fujiwara et al. and Asada-Hirayama et al. both demonstrated the superior diagnostic performance of M-NBI compared to chromoendoscopy for detecting and delineating small GC lesions. [26,27] Fujiwara et al. found M-NBI to have higher accuracy (88.3% vs. 69.9%), sensitivity (78.0% vs. 43.7%), and specificity (92.9% vs. 81.6%) in detecting GC. [26] Asada-Hirayama et al. showed M-NBI's 100% accuracy in determining the extent of early GC (EGC) lesions, outperforming chromoendoscopy, which had significant errors (13% for elevated and 33% for depressed lesions). [27] These studies highlighted M-NBI as a more effective tool for diagnosing and assessing the extent of GC.

Horiuchi et al. tackled the challenge of delineating undifferentiated-type EGCs, which often present vague symptoms and poorer prognoses. [11] They hypothesized that eradicating *H. pylori*, a major cause of inflammation in GC patients, could improve EGC demarcation. [58] Their study revealed high diagnostic accuracy rates for M-NBI: 92.2% in the *H. pylori*-eradicated group, 100% in the *H. pylori*-

uninfected group, and 60.6% in the *H. pylori*-infected group, suggesting that *H. pylori* eradication enhances diagnostic accuracy and prognosis for EGC patients.

Kanesaka et al.'s multi-center prospective study indicated that M-NBI had limitations in diagnosing flat or depressed EGC lesions compared to traditional WLE in 167 EGC patients. [59] Furthermore, Horiuchi et al. found endocytoscopy with NBI to be far superior to M-NBI. [15] Despite potential biases and the exclusion of borderline lesions, their single-center study, handled by a specialized cancer doctor and evaluated by numerous endoscopists, offered valuable insights into real-world clinical scenarios, and suggested a degree of generalizability.

In another important study, Horiuchi et al. conducted an extensive study on detecting EGC, focusing on both the performance of M-NBI instruments and optimizing the diagnostic process using convolutional neural network (CNN) classification on M-NBI images. [13] The study involved training a deep neural network (GoogLeNet) on 1492 EGC and 1078 gastritis images and testing it on 151 EGC and 107 gastritis images, achieving impressive results: an accuracy of 85.3%, sensitivity of 95.4%, specificity of 71.0%, positive predictive value (PPV) of 82.3%, and negative predictive value (NPV) of 91.7%. Despite the high sensitivity of reducing false-positive cases, the study's single-center, retrospective design, and reliance on clear images could affect real-life performance. Future research should expand to multiple centers and adopt a prospective methodology to test robustness in diverse clinical settings.

Additionally, Horiuchi et al. extended this work by exploring M-NBI with a computer-aided diagnosis (CAD) system to distinguish between benign and cancerous endoscopic images.[14] Using the same GoogLeNet CNN, the CAD system demonstrated high accuracy, specificity, sensitivity, PPV, and NPV, outperforming two experts and matching the performance of eight others, slightly below one expert's accuracy. This AI integration with M-NBI showed significant potential, effectively distinguishing between GC and gastritis patients, and streamlining the diagnostic process.

In tandem with these endeavors, Li et al.'s approach integrated CNN with M-NBI to discern between non-cancerous and cancerous gastric lesions, presenting a notable advancement. [30] They employed the Inception-v3 model within the Keras deep learning framework and trained on a dataset consisting of 386 non-cancerous lesions images and 1702 EGC lesions images, with the CNN system showcasing superior performance Horiuchi et al.'s reported accuracy, sensitivity, and specificity. [13] Expanding on these advancements, Tang et al. employed YOLOv3, a real-time object detection algorithm, trained on a substantial dataset of 21,785 NBI images collected from five different centers. [34] Impressively, the YOLOv3 model exhibited even higher accuracy, sensitivity, and specificity compared to previous models such as Inception-v3 and GoogleNet, partly due to the utilization of a larger dataset. Beyond superior metric performance, the AI system developed by Tang et al. stands out for its real-time diagnostic capabilities, representing a significant advancement over previous AI models.

The landscape of AI in GC diagnosis saw a pivotal development when Wang et al. proposed a state-of-the-art classification model using an attention mechanism and feature fusion deep learning model. [36] This cutting-edge AI model demonstrated remarkable automation in classifying various types of lesions with unprecedented accuracy (94.5%), specificity (96.5%), and sensitivity (93.0%) compared to existing models. Remarkably, Wang et al.'s model is the first to integrate feature fusion technology and an attention mechanism into automatic gastric lesion detection. The incorporation of feature fusion, involving the combination of diverse features, has significantly enhanced the model's overall performance, proving particularly effective in diagnosing diverse lesions during the early stages of GC.

The integration of M-NBI and AI in endoscopic technology presents significant advancements in GC diagnostics. The high accuracy, sensitivity, and specificity of M-NBI, particularly when enhanced by CNN and CAD systems, significantly improve the detection and delineation of gastric lesions, as demonstrated by numerous studies. These technological advancements facilitate more precise diagnostics, potentially reducing unnecessary surgeries and enhancing patient outcomes. Nevertheless, certain limitations persist, such as the dependency on high-quality images and the predominance of single-center, retrospective study designs. Expanding research to incorporate multi-center, prospective studies and a more diverse array of image sets will be essential for validating these technologies in real-world clinical settings. Despite these challenges, the ongoing innovation in AI-driven endoscopic techniques represents a promising frontier in the early detection and diagnosis of GC.

2.1.2. Confocal Laser Endomicroscopy (CLE)

Identifying GC in its early stages poses a significant challenge for clinicians due to the need to spot subtle changes in the stomach lining's appearance. Conventional WLE, along with virtual chromoendoscopy are continuously improving. Nevertheless, the effectiveness of a single endoscopic biopsy with WLE remains limited in terms of high sensitivity and specificity. [60] Although NBI can reveal microvascular patterns and microsurface abnormalities, its effectiveness is inherently dependent on the high reflectivity of mucosal surface as well as hemoglobin's strong absorption capacity of narrow band light. [61] In contrast, CLE has emerged as a significant advancement, enabling the simultaneous observation of both microscopic and macroscopic features of the mucosa, offering high magnification and resolution of the mucosal layer in the GI tract for real-time histological diagnosis. [62] In CLE, a laser is focused on to a specific depth and the reflected light emitted is collected and analyzed. The technique utilizes a confocal aperture to exclude out-of-focus light, resulting in the acquisition of sharp, high-contrast images at a microscopic level, giving valuable insights into the tissue's microstructure. [63]

There are two main types of CLE: endoscope-based CLE and probe-based (pCLE). The former requires an endoscope with a miniaturized confocal scanner integrated into the distal tip, which enables simultaneous endoscopic imaging. [64] The latter involves directing a laser onto the mucosa through

optical fibers in a small probe. The mini probe's tip, comprised of lenses, allows for confocal imaging, and can be seamlessly introduced into the endoscope's channel, enabling simultaneous visualization alongside macroscopic imaging. [65]. The application of pCLE extends across diverse medical specialties, providing valuable insights into both structural and functional information. This section will present a comprehensive overview of CLE technology in the specific context of GC, shedding light on its diagnostic potential and clinical implications.

Park et al. explored the potential of pCLE as an imaging technique to enhance the likelihood of identifying cancer cells in endoscopic biopsy samples for undifferentiated GC compared to WLE. [66] A confirmatory study was conducted to differentiate 61 poorly differentiated adenocarcinoma or signet ring cell carcinoma samples. Their pCLE pilot and confirmatory study resulted in a higher proportion of cancer cells in biopsy samples than traditional WLE (pilot: median proportion, 65% versus 30%, P = 0.010; confirmatory: mean ± standard deviation, 49.5 ± 29.3 vs 29.3 ± 13.7, P = 0.002). Moreover, they selected genes and noncoding RNA associated with GC and conducted qRT-PCR to measure expression ratios for tumor markers such as CEA, GW112, Hox transcript antisense RNA and H19, all of which were highly expressed in cancer tissues and a higher expression ratio in the pCLE group. However, it is important to acknowledge the study's limitations. Different biopsy samples were used for histopathological examination and tumor marker assessments, which could lead to discrepancies within the subgroup of differentiated cancers between histopathological examination and tumor marker assessment. Another limitation pertains to the potential learning curve associated with pCLE examinations, which may impact the generalizability of the findings. Consequently, further studies are warranted to validate these results. Nevertheless, these findings serve as a foundation for expanding the applications of pCLE and suggest its utility as a preliminary diagnostic tool before biopsy to ensure adequate tissue sampling.

As a pioneering group in exploiting pCLE, Capuano et al. aimed to provide a prompt and accurate evaluation of pattern and efficiency of intra-tumoral vessels via a non-invasive method. [67] The study involved pCLE imaging captured in 57 patients. This yielded high-quality video and provided real-time imaging of more than 2 thousand frames. Vascular alterations in GC were primarily characterized firstly by leakage, secondly, the presence of tortuous and large vessels. Lastly, the efficiency of blood flow in the vessel. Notably, the first factor was detectable in 81% of the cases and the second was present in 67% patients. In contrast, defects in blood flow were rarely detected, and no significant associations were found between angiogenic score, gastric tumor site and histological type. Subsequently, pCLE results were further evaluated by immunofluorescence using different vascular markers. Notably, they reported that CD150, Multimerin-2 and GLUT1 could distinguish between normal and cancerous gastric mucosa. Overall, these findings show that pCLE can effectively detect functional and structural angiogenic features of the tumor blood network. The real-time assessment of tumor vasculature may offer valuable diagnostic indicators and tailored therapeutic approaches for GC patients.

Similarly, Fornasarig et al. used pCLE to identify specific vascular patterns in high-risk and early-stage GC. [68] Employing high-definition white light and NBI to enhance visibility, they conducted pCLE imaging. The proposed technique demonstrated the ability to distinguish patients based on vascular profiles, revealing higher vascularization characterized by an increased number of tortuous vessels in gastritis patients. Atrophic autoimmune gastritis exhibited a higher prevalence of leaky capillaries. For EGC patients, tortuous vessels, unlike those detected in atrophic gastritis, appeared patchy, resembling neoplastic gastric tissues. Importantly, vascular changes were observed even in areas without lesions, supporting the notion that vascular alterations may create a favorable microenvironment for carcinogenesis. These results suggest that the presence of tortuous vessels with a slightly irregular spatial distribution, along with vascular leakage in precancerous conditions, could hold prognostic value for identifying patients at high risk for developing GC.

For practical clinical applicability, Gong et al. conducted a comparative analysis between CLE and magnifying endoscopy with NBI . [69] Their study involved 82 patients who underwent WLE to identify any superficial elevated, depressed, or uneven lesions. Subsequently, these lesions were examined using both proposed techniques. In magnifying endoscopy - NBI, the diagnostic criteria involved the vessel plus surface and was further categorized into differentiated and undifferentiated based on the appearance of fine network and corkscrew pattern. In CLE, gastric pit pattern and a 2-tiered classification were employed to categorize gastric lesions into noncancerous and cancer/high grace intraepithelial neoplasia, whereby the latter typically shows irregular surface, disorganized patterns, disordered dark cells and unusual shaped micro vessels. For discriminating between cancerous and noncancerous lesions, M-NBI displayed accuracy, sensitivity, and specificity of 93.75%, 91.67% and 95.45% respectively, compared to 91.86%, 90% and 93.48% respectively, for CLE. Thus, M-NBI appeared to be the superior method in this case. Regarding the differentiation of GC, CLE demonstrated a numerically higher accuracy but was not statistically significant compared to M-NBI (81.25% vs 73.33%). Using histopathology as the ‘gold’ standard, both methods showed nearly perfect agreement (M-NBI, k = 0.87; CLE, k = 0.84). However, the study had several limitations. Recruitment included patients with previous diagnoses, leading to an increased proportion of cancerous lesions. Moreover, AGC patients were excluded. As a single-centered study, cost-effectiveness between the two modalities was not evaluated. Nevertheless, both techniques could detect GC lesions and while CLE did not prove superior to M-NBI, a unified diagnostic strategy and consensus on criteria for both techniques in diagnosing GC lesions are expected to be proposed in the future.

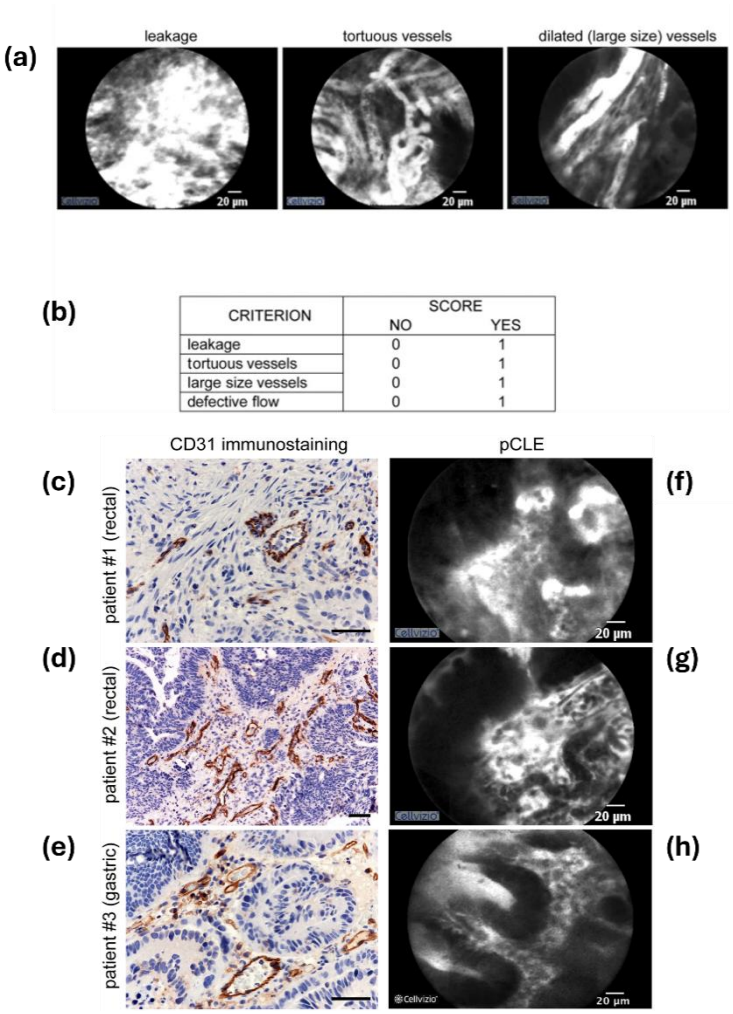

Figure 3. (a) pCLE endomicroscopy images displaying vessel leakage, tortuous vessels as well as dilated blood vessels. (b) Table of criteria used to generate an angiogenic score, i.e. the sum of scores of each parameter, to which a value of 0 represents absence and 1 indicating present. (c-e) Immunohistochemical staining of the tumor sections from 2 rectal patients and 1 gastric patient respectively. (f-h) pCLE endoscopic images obtained from the same 2 rectal patients and 1 gastric patient respectively. *Reproduced with permission under the terms of the CC BY 4.0 license. [70] Copyright 2017, The Authors published by Springer Nature.*

In Spessotto et al.'s study, pCLE was employed for the evaluation of tumor angiogenesis in rectal and GC. [70] 126 patients with locally advanced cancer (35 GC and 91 rectal carcinoma) underwent both endoscopy and pCLE analyses. In all patients, pCLE provided clear visualization of blood vessels and successfully identified typical abnormal features of tumor-associated vessels. These included enlarged, twisted and leaky microvessels with disrupted blood flow, as shown in **Figure 3**a. Three factors were assessed: 1) mucosal architecture; 2) vascular density and vessel morphology; 3) blood flow efficiency. An angiogenic scorefrom 0 (indicating normal vasculature) to 4 (indicating aberrant vasculature) was then assigned; the scoring criteria are outlined in Figure 3b. The results indicated high angiogenic scores in both cancers, characterized by the presence of large and tortuous vessels along with fluorescein leakage into highly vascularized tumoral tissue. To validate their results, a comparison was made with immunohistochemical staining, demonstrating a clear qualitative overlap between both results, and

confirming the dependability of pCLE, as seen in Figure 3c-h. Additionally, a preliminary examination of tumor blood vessels post-chemotherapy revealed a small remission in 27% of GC patients and the unaltered angiogenic score suggested a potential limitation in treatment efficacy. In summary, the study shows the potential of pCLE not only in providing real-time insights into vascularization density and efficacy, but also in enhancing the diagnostic landscape. This technique offers vital information for assessing treatment effectiveness.

Bok et al. studied the effectiveness of pCLE compared to conventional endoscopic forceps biopsy for accurate diagnosis of superficial gastric neoplasia. [71] The study, involving 46 patients, evaluated the overall accuracy of endoscopic, in-vivo pCLE, and offline pCLE diagnoses by comparing them with post endoscopic resection. Among the 54 superficial gastric lesions examined through histopathology, 3 were non-neoplastic lesions, 19 were gastric dysplasias, 22 were differentiated and 10 were undifferentiated adenocarcinomas. Agreement with histopathology was substantial for conventional biopsies ($k = 0.617$) and excellent for in-vivo pCLE ($k=0.824$) ($P<0.001$). Concerning the accuracy of adenocarcinoma diagnosis, pCLE exhibited a higher accuracy of 91.7% compared to conventional biopsies at 85.2% ($P=.065$). The combined accuracy for both methods was 98.1%. The interobserver agreement for offline pCLE diagnosis was excellent ($k = 0.931$). However, the study is limited by several factors. Firstly, the first endoscopist's performance of in-vivo pCLE diagnosis may introduce bias influenced by the endoscopic appearance of lesions. Secondly, biopsy specimens obtained from referring hospitals were subjected to various physicians, leading to inconsistent results.

In summary, pCLE introduced here offers real-time histological insights for GC. Studies demonstrate its potential in enhancing biopsy yield, evaluating vasculature, and discerning vascular patterns. However, CLE for GC diagnosis faces several limitations. The diagnostic accuracy is highly dependent on the user's experience and training, resulting in a steep learning curve for less experienced practitioners. [72] Moreover, due to its high cost, this further imposes a barrier for clinical adoption. [62,73] Despite these challenges, it is notable that pCLE outperformed conventional biopsies in Bok et al.'s study and was successful in differentiating vascular and tumoral vessels. With further research and standardization, along with the integration of AI model training, CLE could potentially be incorporated into routine clinical practice for GC diagnosis.

2.1.3. Raman Spectroscopy (RS)

The principle behind RS is rooted in the inelastic scattering of light when it interacts with matter. This phenomenon, known as the Raman shift, describes the changes in wavelength during the scattering of light. The energy difference between the scattered and incident light serves as an indicator of molecular vibrations in the sample upon light excitation. [74] This unique energy pattern, resulting from specific molecular vibrations, forms a characteristic Raman spectrum, often referred to as a molecular fingerprint (FP). RS emerges as a powerful analytical tool for detecting GC, as it can identify the

chemical and biological composition of different samples without requiring reagents or extensive preparation. This is crucial since the content, structure, and conformation of various cell components change during carcinogenesis.

RS holds significant promise for the in-vivo detection of GC by enabling real-time, non-invasive analysis of molecular changes directly within the body. In-vivo RS can provide immediate feedback during medical procedures, offering a powerful tool for early diagnosis and real-time monitoring of cancer progression. By capturing the unique Raman spectra of gastric tissues, clinicians can identify biochemical markers indicative of cancerous changes, without the need for tissue extraction or extensive preparation.

To date, the bench-top system for RS poses a challenge for in-vivo clinical diagnosis due to weak tissue Raman scattering and lengthy acquisition times. [75] Substantial progress has been made by integrating fiber probes with endoscopic platforms, translating RS into real-time in-vivo applications across various organ sites such as colon [76,77], esophagus [78–81] and so forth. In the forthcoming discussions, we will delve into specific articles that illuminate the technological potential of this integration under in-vivo applications, shedding light on its transformative impact in the realm of medical diagnostics. An earlier study by Bergholt et al. evaluated the use of fiber-optic RS to monitor the progression of intestinal-type gastric carcinogenesis during in-vivo endoscopic examinations. [82] By integrating RS with endoscopy, the study successfully identified gastric tissue pathologies, including normal mucosa, intestinal metaplasia, dysplasia, and adenocarcinoma, with diagnostic accuracies ranging from 79.69% to 94.92%, showcasing its potential for real-time, non-invasive detection of precancerous and cancerous gastric lesions.

Wang et al. and Duraipan et al. conducted studies investigating the use of RS for early GC detection during clinical endoscopic examinations. [83,84] Wang et al. compared the diagnostic performance of two endoscope-based fiber-optic Raman probes—beveled and volume probes—for detecting gastric dysplasia. The beveled probe demonstrated superior diagnostic accuracy (93%) compared to the volume probe (88.4%), with improved tissue Raman signal capture and specificity. Duraipandian et al. developed a real-time, automated RS system integrated with multimodal imaging for in-vivo GC diagnosis. This system reported a diagnostic accuracy of 85.6% and achieved 80% accuracy in prospective clinical tests, highlighting its feasibility for real-time diagnostics during live examinations. Both studies emphasized the potential of RS to enhance early GC detection.

Furthermore, the same research group developed a rapid, image-guided Raman endoscopy system for in-vivo tissue diagnosis.[85] This real-time method was tested for precancer detection, with results compared against histopathological examinations. Raman spectral data were obtained using a 785 nm diode laser and a 1.8 mm flexible endoscopic probe, which could pass through conventional endoscope channels, enabling real-time Raman measurements. Observations revealed a relative percentage change

between normal and dysplastic mucosa at peaks 1004, 1265, 1335, 1445 cm^{-1} similar to Li et al.'s study [86], 1655 cm^{-1} similar to Luo et al.'s study [87] and 1745 cm^{-1}. Notably, dysplastic tissue displayed intense Raman peak at 1004 cm^{-1}, associated with phenylalanine, demonstrating an increase in protein contents [85]. Using a Raman endoscopic database of over 400 gastric patients, partial least squares discriminant analysis (PLS-DA) and leave-one-patient-out were employed for online prospective diagnosis of dysplasia in 4 patients to give a sensitivity and specificity of 81.5 and 87.9% respectively.

Similarly, Bergholt et al. used a trimodal image-guided Raman spectroscopic platform along with the same confocal-type endoscopic fiber-optic probe to conduct real-time, in-vivo tissue measurements on a cohort of 5 gastric patients. [88] Noteworthy spectral differences particularly at 936, 1004, 1655 and 1745 cm^{-1} were observed when comparing normal and dysplastic gastric epithelium. These findings align with the outcomes of Huang et al.'s study, reinforcing the credibility of both studies. [85] Further analysis using PLS-DA modeling revealed a promising real-time identification of gastric dysplasia with a sensitivity and specificity of 81.3% and 88.3% respectively. On a lesion basis, the successful identification of all dysplastic lesions underscores the technique's robustness. While both studies showcase the potential of Raman endoscopy as a clinical tool, further evaluation of its clinical merits using this multimodal image-guided technique on a larger sample cohort is deemed necessary to solidify its place in future medical diagnostics.

The research group advanced their studies on gastric abnormalities using the real-time rapid fiber-optic RS system. Wang et al. focused on detecting gastric dysplasia and adenocarcinoma in a larger cohort of 191 patients, collecting 5,792 spectra and demonstrating high diagnostic performance, with 96% sensitivity for normal tissue and 81.8% for dysplasia. [89] Lin et al. extended the application of the RS system to target early detection of gastric intestinal metaplasia, collecting 4,520 spectra from 157 patients, achieving a sensitivity of 89.3% and specificity of 92.2%. [90]The key distinction between the two studies lies in their clinical focus—while Wang et al. concentrated on identifying more advanced stages of gastric disease, such as dysplasia and cancer, Lin et al. emphasized early detection of intestinal metaplasia, showcasing the system's versatility and broader diagnostic potential across different stages of gastric pathology. This progression highlights the group's continued efforts to enhance the RS system's clinical utility, from early-stage detection to more advanced gastric diseases.

Despite its potential, the development and application of in-vivo RS systems for GC detection remain limited. The challenges are multifaceted, including the need for miniaturized, flexible endoscopic probes that can deliver and collect Raman signals within the complex environment of the gastrointestinal tract. Additionally, ensuring sufficient signal-to-noise ratio, avoiding interference from surrounding tissues, and maintaining patient safety are critical considerations. Current research efforts are focused on overcoming these technical hurdles, such as enhancing probe sensitivity, integrating advanced data processing algorithms, and validating the accuracy of RS in clinical settings. As these

technological advancements continue, in-vivo RS is expected to become a more viable and effective method for GC detection, offering a less invasive alternative to traditional biopsy and histopathology. However, further studies and development are necessary to fully realize its clinical potential and ensure its reliability and efficacy in routine medical practice.

2.1.4. Fluorescence Spectroscopy and Imaging

Fluorescence is emitted when a substance gets excited to a higher energy state upon absorption of photons of a particular absorption band from the incident radiation. [91] The molecules that exhibit fluorescence can be endogenous fluorophores within the tissues or exogenous fluorescent dyes or nanoparticles. This section includes diagnostic, staging and lymph node detection methods using fluorescence in-vivo through endoscopy. Notably, studies have highlighted the use of 5-aminolevulinic acid (5-ALA) based photodynamic diagnosis (PDD).

Loshchenov et al. studied the usage of laser spectral and video fluorescence images for diagnosis of stomach tumors. [92] For such a fluorescence diagnosis or photodynamic action, a photosensitizer (PS) is a key component as the change in its concentration and dynamics with time is measured to understand the tissue properties. This is the basis of PDD and therapy. The PS used was 5-ALA which triggers the formation of porphyrins. As the concentration of 5-ALA increased, highly fluorescent protoporphyrin IX (PPIX), an intermediate product of heme formation, accumulated in the tumor cells. To facilitate their investigation, they used a fiber optic device with a Y-shaped end with input He-Ne laser source of 632.8 nm. The probe was designed to be introduced into the biopsy channel of an endoscope. The study also employed video analysis for white light examinations along with fluorescence imaging. It was tested on 43 patients, 25 stomach cancer, 14 gastric ulcer and 4 chronic gastritis. The findings indicated that this spectroscopic approach achieved a penetration of 3-4 mm, enabling non-invasive scanning of mucous and submucosal stomach layers. The fluorescence registration with video analysis offers real-time results, which could assist surgeons in estimating dubious stomach tissues and perform accurate site biopsies. Additionally, the simplicity and safety of video fluorescence diagnosis can be advantageous to be employed in existing endoscopic examinations. This can give a clear intraoperative assessment of tumor size, extent and identify the carcinomatous foci during laparoscopy.

Some studies highlighted here compare exogenous and endogenous fluorophores in diagnosis and intraoperative lymph node imaging. These studies demonstrate better detection with exogenous fluorophores while also addressing their drawbacks. Angelova et al. measured intrinsic autofluorescence and exogenous fluorescence both in-vitro and in-vivo, aiming to enhance the effectiveness of diagnosis. [93] In this section, we discuss the in-vivo experiment where measurements were done using gastro endoscopy. The excitation wavelengths used were 405, 530, and 630 nm. The exogenous 5-ALA/PPIX fluorophores were administered orally 6 hours prior, effectively differentiating

between normal and abnormal tissues in 1D spectroscopic regime, though less successfully in 2D images. They concluded that while autofluorescence provided a high sensitivity of greater than 90% and was considered safer, a low specificity of 55-60% was observed. Conversely, the usage of 5-ALA/PPIX obtained a sensitivity and specificity greater than 90%, presenting itself as a potential tool for gastric tumor diagnosis and tumor/lymph node resection in clinical applications. Using a similar methodology, Isomoto et al., used an endoscopy with 410 and 450 lasers, former for excitation in PDD and the latter for generating white light through a phosphor in upper GI tumors . [94] The study involved 27 GI tumors (25 gastric lesions and 2 adenocarcinoma) and the subjects were administered with ALA 3 hours prior to the procedure. This blue illumination at 410 nm was able to detect red fluorescence in upper GI tumors in 23 of 27 cases. The intensity of the emitted fluorescence signal differed significantly between depressed and elevated tumors, allowing them to be distinguished.

To study the benefits of ICG-based NIR fluorescence imaging of lymph nodes during robotic gastrectomy, Cianchi et al. assessed intraoperative visualization improvements. [95] They compared the outcomes of 37 patients who received submucosally injected ICG the day before surgery with 37 patients who underwent the same robotic surgery without ICG injection. The surgery was carried out with a da Vinci Si surgical system and an NIR fluorescence imaging system was used for ICG detection. The ICG group exhibited a higher number of lymph nodes (mean: 50.8) as compared to the group without ICG (mean: 40.1). This suggests that ICG-based NIR intraoperative imaging detects additional nodes, aiding in the removal of residual lymph nodes after lymphadenectomy and enhancing cancer staging accuracy. However, the low accuracy, sensitivity, and specificity for metastatic lymph node detection, which are 62.2%, 52.6%, and 63% respectively raises concerns for real-world application reliability. This limitation may stem from the obstruction of lymphatic vessels by cancer cells, leading to an inability to stain positive lymph nodes. Consequently, this drawback is particularly pronounced in gastric tumors ≥ T2 (the stage where the tumor would have infiltrated the muscularis propria), which are highly metastatic.

In a demonstration of the usage of fluorescence in guided GC surgery, Baiocchi et al, introduced ICG as a fluorescent tracer during lymphadenectomy. [96] The study was done on 13 patients with GC where ICG was injected a day before the surgery or through the submucosal, sub serosal route. An infrared camera using a wavelength of 750 nm for ICG excitation was used. The video collected was then reassessed for lymph node fluorescence. The residual ICG nodes after the lymphadenectomy were analyzed and classified both in-vivo into ICG+ (fluorescent nodes) and ICG- (non-fluorescent nodes), and ex-vivo into metastatic and non-metastatic. The comparison of ex-vivo pathology report and the fluorescent imaging system showed that none of the ICG- nodes were metastatic and an average of 38 nodes were removed per subject. Lymphatic drainage from the ICG injection sites were observed in 11 out of 13 subjects which showed 84.6% success rate. These results were promising for a new technique of fluorescence-guided GC lymphadenectomy that has a high feasibility and ease of use.

2.2. In-vitro/ Ex-vivo modalities

2.2.1. Raman Spectroscopy (RS)

RS is increasingly utilized in the ex-vivo and in-vitro detection of GC due to its ability to provide detailed molecular insights without the need for complex sample preparation or staining. Ex-vivo and in-vitro methods leverage RS to analyze tissues and biological samples outside the living organism, enabling precise control over experimental conditions and repeated measurements. This approach allows researchers to identify specific biochemical changes associated with malignant tissues, such as alterations in proteins, lipids, and nucleic acids, which manifest as distinctive spectral signatures. By employing advanced analytical techniques and machine learning algorithms, RS can discern between normal and cancerous samples with high accuracy. Additionally, the non-destructive nature of RS preserves the integrity of samples for further analysis. The combination of RS's molecular sensitivity and its applicability in controlled environments underscores its potential as a powerful tool for early GC detection and diagnostic research, paving the way for future in-vivo applications.

Several studies have investigated unique spectral peaks present in cancer samples and compared peak ratios as a diagnostic tool. One example by Luan et al., employed fiber optic RS on specimens obtained through endoscopic submucosal dissection from EGC patients. [97] The study involved 13 EGC patients, obtaining 55 sets of Raman spectral data comprising lesional, high-grade intraepithelial neoplasia (HGIN), adenocarcinoma and non-lesional tissues. In contrast to non-lesional samples, lesional tissues exhibited a distinctive peak at 1324 cm^{-1} attributed to the bases of deoxyribonucleic acid (DNA). HGIN displayed extra peaks at 826, 838, and 1253 cm^{-1}, while adenocarcinoma tissues exhibited peaks at 820, 948, 1293, 1517, and 1531 cm^{-1}. The integral energy ratio (noncontinuous and continuous frequency bands) underwent analysis using an independent-samples t-test, revealing a significant difference between the two datasets ($P < 0.01$). Given the assignment of 1560 cm^{-1} to tryptophan, it may serve as a potential tumor marker due to a significantly higher peak intensity ratio in EGC tissues. Overall, the integral energy ratio demonstrated superior sensitivity and specificity, indicating its potential as a diagnostic indicator for EGC.

In Zhou et al.'s study, RS was applied for ex-vivo detection of GC in the high wavenumber (HW) region and compared its diagnostic potential with that of FP region. [98] Distinctive variations in Raman spectra between normal and cancerous tissues (38 normal and 37 GC) were evident at 853, 879, 1157, 1319, 1338, 1448, and 2932 cm^{-1}, associated to proteins, lipids, nucleic acids, collagen, and carotenoids within the tissue. Using PLS-DA and cross validation, they developed diagnostic algorithms, finding the FP region model to outperform the HW region in receiver operating characteristic (ROC) analysis. Despite FP region advantages, leveraging both regions are recommended for comprehensive GC diagnosis, with future studies needed to validate and adapt these findings for in-vivo applications.

Ikeda et al. proposed using RS for GC diagnosis on unstained pathological samples, revealing elevated intensity ratios in cancerous tissues compared to normal samples at specific wavelengths (782/620, 782/756, 782/1250, and 782/1263 cm^{-1}). [99] The study highlights limitations such as small sample size, suboptimal sample preparation, and single-wavelength laser constraints, necessitating optimized spectroscopy protocols and validation against gold-standard methods. Chen et al.'s RS study demonstrated the analysis of genomic DNA, nuclei, and tissue components in GC development, identifying distinct spectral changes between normal and GC samples across various wavelengths (950-1600 cm^{-1}). [100] Their findings underscore RS's potential in elucidating GC tumorigenesis mechanisms and enabling early diagnosis, suggesting broader clinical applications for RS in understanding biochemical alterations in mucosal tissues.

Guleken et al. utilized Fourier Transform RS to analyze serum samples from GC patients and healthy controls, identifying elevated levels of tumor markers such as CEA, AFP, CA-125, CA-15-3, and CA19-9 in GC patients. [101] Their study, involving 70 participants, applied PCA to distinguish between control and GC groups based on Raman spectra dynamics, revealing characteristic peaks at 1182, 1280, 1560, and 1665 cm-1 indicative of GC. ML and ROC analysis demonstrated over 95% accuracy, highlighting FT-RS as a promising tool for predicting GC markers. In another interesting study, Cao et al. corroborated these findings, emphasizing the significance of CEA and CA19-9 as potential protein biomarkers for GC. [102] Their proteomic analysis of serum samples from gastrointestinal cancer patients showed upregulation of these biomarkers in GC compared to controls. Additionally, studies by Feng et al. and Zhou et al. supported these observations, linking elevated CEA and CA19-9 levels to poor prognosis in GC patients undergoing radical gastrectomy and proteomic investigations. [103,104] These collective findings underscore the potential of serum biomarkers like CEA and CA19-9 in enhancing early detection and prognostic evaluation of GC.

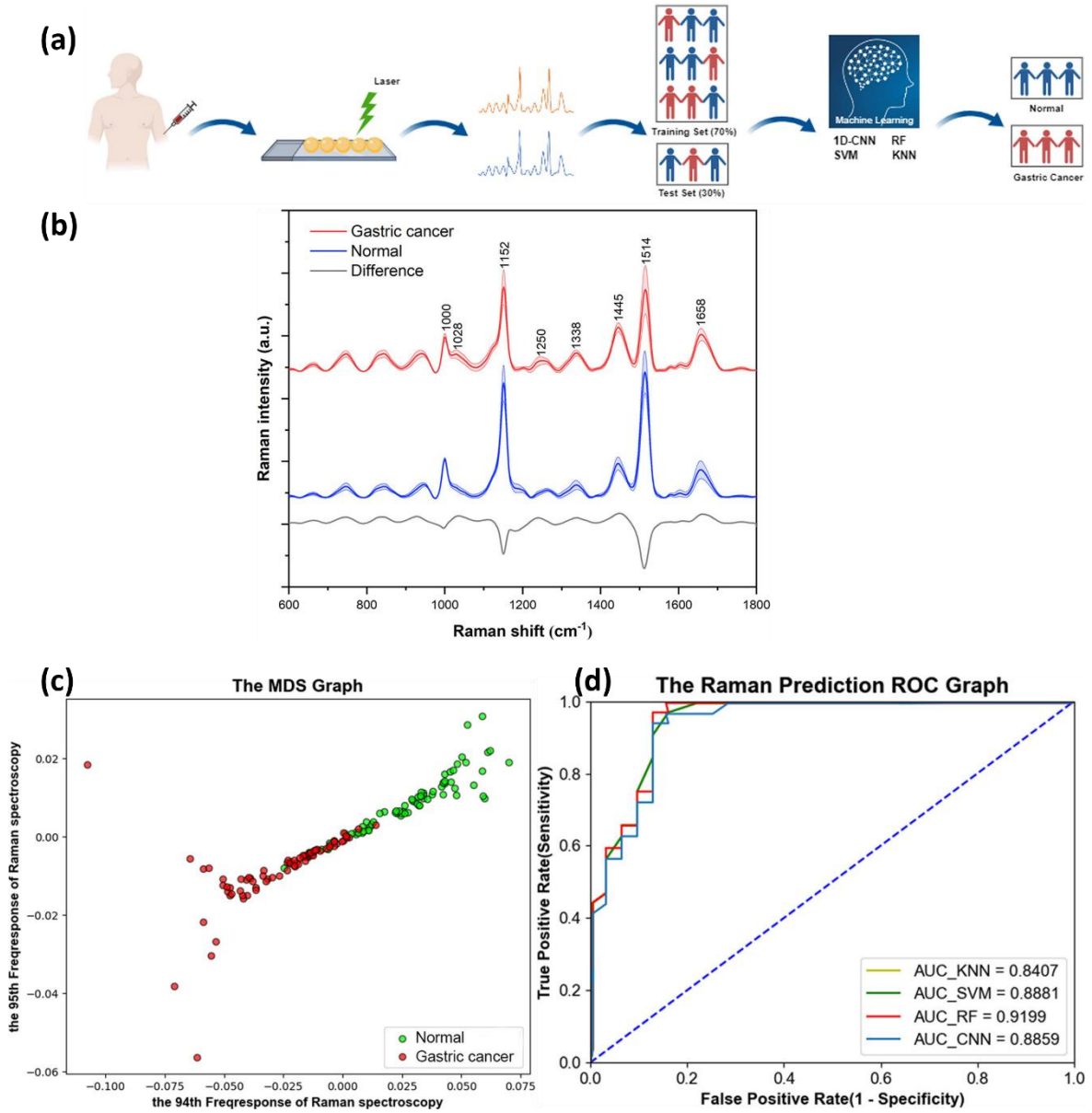

Figure 4. a) Schematic overview of serum RS in combination with various ML methods for non-invasive GC screening. B) A comparison of normalized average Raman spectra of normal (blue) and GC (red) samples. Shaded regions depict standard deviations. Additionally, bottom section displays the spectral difference between GC and normal, with spectra offset for clarity. C) A scatter plot of GC (red) and normal (green) groups based on spectral frequency response characteristics in RF classification model. D) Receive operating characteristic curve of serum Raman spectra using four ML models. *Reproduced with permission under the terms of the CC BY 4.0 license.* [86] *Copyright 2021, The Authors published by Frontiers.*

Several studies have delved into the application of ML and algorithms to discern between cancerous and normal groups, showcasing a growing interest in leveraging computational techniques for enhanced diagnostic precision. This is evident in the research conducted by Li et al., combining RS with various ML methods. [86] They employed serum samples from 109 GC patients across different cancer stages and 104 healthy volunteers. A schematic overview of this study can be found in **Figure** 4a. Subsequent comparison of average Raman spectra revealed lower peak intensities at 1000, 1152, 1514 cm^{-1} in GC patients, while 1445 and 1658 cm^{-1} were higher, as seen in Figure 4b. To analyze the difference in serum metabolism, four ML methods – k nearest neighbors (KNN), support vector machine (SVM), 1D-CNN

and random forest (RF) – were employed. Among these methods, RF stood out as the most effective in distinguishing serum Raman spectrum for GC with accuracy, sensitivity, and specificity of 92.8%, 94.7% and 90.8% respectively. Notably, the Multidimensional Scaling graph in Figure 4c highlighted the effective discrimination of most samples, despite some minor overlap. However, this also accentuates and method's limitation in robustly classifying all samples solely based on the 94th and 95th Raman spectral bands. Further diagnostic evaluation by ROC curve was performed to give an area under the curve of 0.9199, as depicted in Figure 4d. This reinforces RF as the superior ML method in this context. While these results show promise, incorporating more clinical samples and expanding the sample size for training could enhance the robustness of the algorithms. Furthermore, to bolster the reliability of GC diagnosis in clinical settings, future investigations should include patients with gastritis, gastric ulcer, and other benign gastric lesions, thereby establishing a more dependable detection methodology. Overall, this study presents a non-invasive and rapid pre-screening method, offering potential implications for the early diagnosis of GC before moving on to the combined diagnosis of gastroscopy biopsy for precise evaluation.

Bahreini et al. proposed an in-vitro screening method for GC using multivariate data analysis on serum samples. [105] They employed RS coupled with a thermoelectrically cooled spectrometer via optical fiber. The study assessed serum constituents like cholesterol, triglycerides, glucose, and lipids using enzymatic tests, achieving a strong correlation coefficient of 94% between Raman spectra and enzymatic results through partial least squares regression. Classification with PLS-DA on a cohort of 60 patients (40 healthy, 20 GC) demonstrated an accurate detection rate of 87.5 ± 2.5%. While confirming RS's potential for distinguishing between healthy and GC subjects and its promise in GC screening, the study emphasizes the need for comparison with other diagnostic technologies such as tissue histopathology or upper endoscopy for definitive clinical diagnosis. Building onto ML techniques, Luo et al. developed a diagnostic algorithm using RS to differentiate normal, adenomatous polyp, and GC tissues. [87] They identified significant Raman bands indicative of tissue changes, such as peaks at 853, 936, 1032, 1174, and 1208 cm^{-1}. Diagnostic algorithms integrating PCA-naïve Bayesian classifier achieved high sensitivity and specificity for tissue classification, demonstrating RS's potential as a noninvasive screening tool despite technical challenges.

In Li et al.'s study, SENet-LSTM framework was introduced to classify gastric mucosa using RS, focusing on distinguishing normal and cancerous tissues based on Raman spectral differences. [106] Their approach highlighted significant differences at various wavelengths associated with biochemical components. The framework showed impressive classification performance with high accuracy, sensitivity, and specificity, suggesting its potential for pre-cancerous screening. Similarly, Liu et al. developed a comprehensive Raman spectral database using GC and normal cell lines. [107] Their stacking ensemble learning model, SL-Raman, demonstrated remarkable differentiation accuracy by integrating predictions from various classification models, enhancing the representativeness and accuracy of RS in

detecting GC. Meanwhile, Wang et al. utilized Euclidean distance-based RS (EDRS) to establish a prognostic prediction model for GC using paraffin-preserved tissue samples. [108] They successfully categorized patients into prognostic groups based on Raman spectral heterogeneity, demonstrating effective classification and survival analysis capabilities. With further validation in larger cohorts, EDRS offers a promising, cost-effective tool for clinical cancer prognosis, potentially guiding personalized treatment strategies and improving patient outcomes.

Innovatively, Liu et al. combined stimulated Raman scattering (SRS) microscopy with deep learning to achieve single-shot femtosecond SRS (femto-SRS) images for chemical-specific analysis of native biomolecules in fresh gastric biopsies. [109] Using a non-portable SRS system, they measured fresh gastric biopsies and employed a deep learning algorithm, U-Net, to convert single-shot femto-SRS into dual-channel pico-SRS, generating hyperspectral images. In comparison to traditional H&E staining, U-Net generated multi-colored femto-SRS, and femto-stimulated Raman histology images, revealing high agreement with H&E on fresh biopsy tissues but showing distinct structural features due to better preservation of histoarchitecture in gastric tissues. Further classification using CNN achieved a diagnostic accuracy of 96.4% in identifying cancerous lesions, with high concordance ($k = 0.899$) with true pathology. Despite these accomplishments, the study suggests the need for advanced deep-learning models to reduce labeling workload and errors and calls for future work focusing on miniaturizing the SRS system for near real-time intraoperative diagnosis.

The extensive research and promising results of RS in ex-vivo and in-vitro detection of GC highlight its potential as a powerful diagnostic tool. RS's ability to provide detailed molecular insights without complex sample preparation allows for precise control over experimental conditions and repeated measurements. Studies have demonstrated the effectiveness of RS in identifying biochemical changes associated with malignant tissues, leveraging advanced analytical techniques and machine learning algorithms to achieve high diagnostic accuracy. Furthermore, RS's non-destructive nature preserves sample integrity, enabling further analysis. However, despite these advancements in ex-vivo and in-vitro applications, the development of in-vivo RS systems remains limited. Challenges such as miniaturizing the technology for endoscopic use, ensuring adequate signal-to-noise ratio, and maintaining patient safety need to be addressed. Future research must focus on overcoming these technical barriers to enable real-time, non-invasive GC detection in clinical settings. Continued innovation and validation are essential to fully harness RS's potential, paving the way for its integration into routine diagnostic practices and ultimately improving early GC detection and patient outcomes.

2.2.2. Surface Enhanced Raman Spectroscopy (SERS)

While the Raman scattering process provides informative data, its magnitude is typically tens of orders of magnitude lower than that observed in fluorescence, limiting its practical application in clinical settings. [110] To overcome this challenge, SERS has emerged as a pivotal solution, significantly

enhancing the Raman signal to create a high-resolution, sensitive, and stable analytical tool. The method achieves an enhancement of the Raman signal by 9-14 orders of magnitude compared to conventional RS. [111] SERS is well-suited for biological samples as it effectively quenches fluorescence, a common challenge encountered in such samples. SERS offers distinct advantages over conventional proteomic methods such as polymerase chain reaction (PCR), ELISA, and Western blot. In contrast to PCR, SERS enables direct protein detection. [112] Moreover, ELISA can be susceptible to background signals from non-specific binding with varying sensitivity while SERS provides a detailed molecular profiling. [113] Additionally, SERS requires minimal sample material, in contrast to the substantial quantities often needed for Western blot. The non-destructive and label-free nature of SERS preserves sample integrity. In general, SERS offers enhanced sensitivity, specificity, and versatility, making it a powerful tool for GC research and diagnostics compared to traditional proteomic techniques.

SERS relies on the adhesion of target molecules onto noble metal substrates, typically nanoparticles. When exposed to light, electrons from the conduction band of the metal substrate undergo resonant oscillation, inducing a significant electromagnetic enhancement near the substrate surface. [114] The selection of the SERS substrate is pivotal in determining the extent of Raman signal enhancement, necessitating characteristics such as high stability, sensitivity, ease of preparation, and cost-efficiency. **Figure 5a** shows the visualization of the principles underlying SERS and its application in detecting GC.

Recent advancements in SERS investigations have focused on optimizing signal enhancement via various substrates. Zhang et al. used a graphene oxide-supported gold nanocomposite for SERS-GC detection on 44 salivary samples (24 GC, 20 healthy), effectively distinguishing GC patients from healthy controls by analyzing eight salivary amino acid biomarkers. [115] Lu et al. synthesized a stable gold nanocone array, addressing the instability of traditional SERS substrates for GC detection. [116] Wei et al. developed gold nanoparticles/silicon nanowire arrays to analyze SERS spectra of 50 serum samples (26 GC, 24 healthy), identifying higher SERS intensities in GC samples, indicating increased nucleic acids and decreased protein levels. [117] Similarly, Chang et al. created an ultrasensitive SERS system with a novel nanoprobe substrate, demonstrating superior targeting and sensitivity towards MGC-803 cancer cells due to folic acid conjugation. [118]

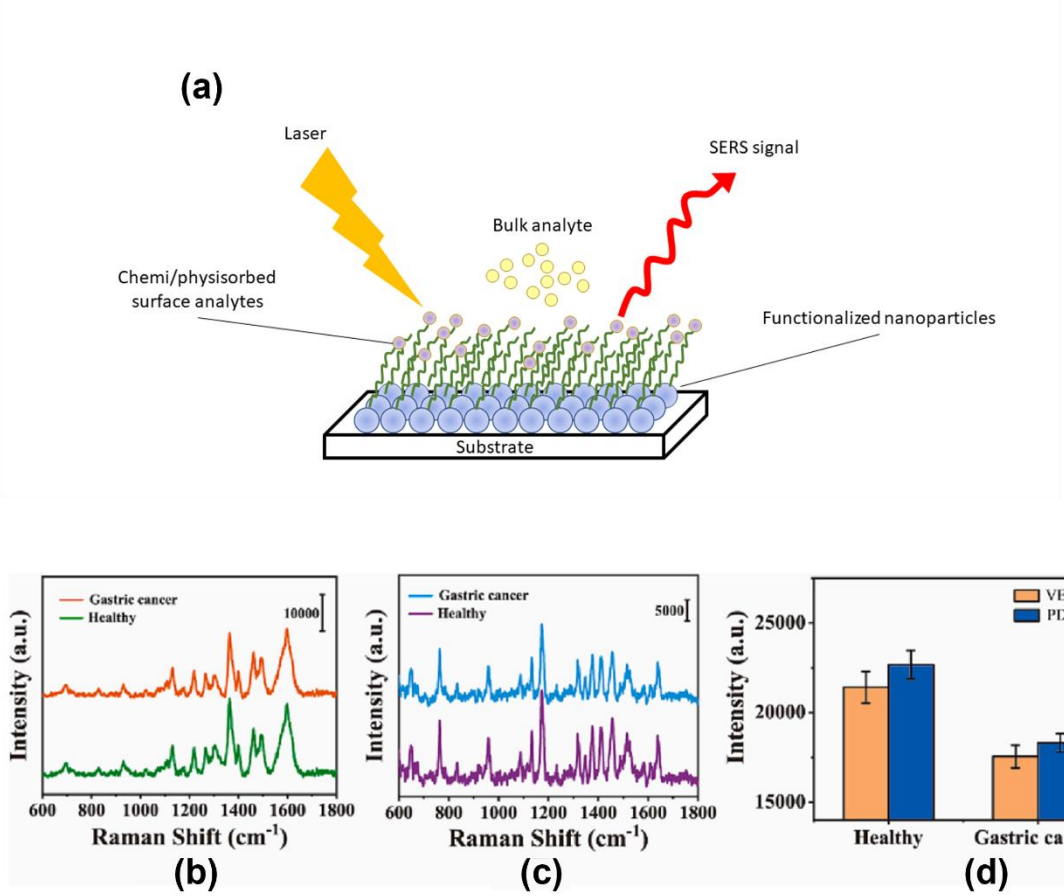

Figure 5. a) Visualization of the SERS phenomena. Functionalized noble metal nanostructures on the substrate enhance weak Raman scattering signals while concurrently suppressing fluorescence. Analyte molecules selectively adhere to the functionalized nanoparticle substrate. Due to proximity, SPR in the noble metal substrate generates an amplifying electromagnetic field, significantly intensifying Raman scattering signals. This innovative substrate design serves the purpose of facilitating the sensitive detection of low-concentration analytes. b, c) Spectra of samples obtained from healthy and GC subjects; d) the concentration of biomarkers VEGF and PDGF-B derived from peak intensities in the spectra. (b-d) *Reprinted with permission [119], Copyright 2023, Elsevier.*

Key biomarkers such as Vascular Endothelial Growth Factor (VEGF), CEA, micro ribonucleic acid (mRNA), miR-106a, and Platelet-Derived Growth Factor-B (PDGF-B), serve as integral indicators of molecular changes associated with GC progression. [120–122] Their aberrant expression underscores their significance as diagnostic targets. VEGF, a key pro-angiogenic factor, is often overexpressed in GC, promoting tumor vascularization and metastasis. CEA, a glycoprotein, exhibits elevated levels in GC patients and correlates with tumor aggressiveness. miR-106a, demonstrates dysregulation in GC, influencing cell proliferation and apoptosis. PDGF-B, involved in cell growth and angiogenesis, is upregulated in GC, contributing to tumor development. The abnormal expression of these biomarkers highlights their pivotal role in GC pathogenesis, establishing them as vital targets for diagnostic applications.

In a significant contribution to this research field, Huang et al. introduced a cutting-edge approach, using a capillary-driven SERS microfluidic chip with gold nano-sheets functionalized with 4-MBA-antibody conjugates. [123] The incorporation of 4-MBA conjugated antibodies enabled the capture of

upregulated GC biomarkers, specifically VEGF and CEA, resulting in a discernible Raman frequency shift. The study established a linear relationship between Raman intensity and biomarker expression levels. Further comparisons between blood serums of healthy individuals and those with GC was performed, revealing elevated levels of VEGF and CEA in GC subjects compared to healthy subjects. The results were validated and showed good agreement with the gold-standard method of detection, ELISA, with relative errors of less than 8%. The SERS system exhibited high reproducibility and sensitivity, particularly on low-concentration biomarkers compared to ELISA.

Similarly, Chen et al. developed a lab-on-a-chip SERS (LoC-SERS) technique to identify potential serum biomarkers such as VEGF and PDGF-B for GC diagnosis. [119] It features 3 parallel channels that comprise 2 detection chambers each, for simultaneous biomarker detection. Firstly, the aptamers of the two biomarkers were modified on the gold nanobipyramids array. Then, two complementary DNA labeled with Raman reporter will bind with the corresponding aptamer on the array. During analysis, these DNA complexes will be released, allowing the aptamers to capture the target biomarkers through competitive binding on the array. By monitoring Raman intensity and fitting it with the logarithm of concentration, a mathematical relationship could be correlated between the two factors. Given the complexity of serum composition in clinical diagnosis, they evaluated the reliability of the SERS system to be used in a clinical context, a comparison was made with ELISA using 60 serum samples (30 healthy and 30 GC). An average SERS spectrum of the two groups can be seen in Figure 5b and c. The intensity changes for VEGF and PDGF-B at 1363 cm^{-1} and 1174 cm^{-1} respectively depicted in Figure 5d, were substituted into a linear equation to determine their concentrations. Results obtained from the calculations showed a slight variance compared to ELISA, with relative errors under 10%, affirming the dependable nature of the sensing system. Therefore, the proposed LoC-SERS system could potentially be an effective tool for diagnosing GC due to its high accuracy and sensitivity.

Exosomes offer a unique avenue for GC detection, offering a wealth of tumour-related information which position themselves as potential candidate for effective diagnosis. While conventional methods lack sensitivity and require advanced equipment, Pan et al. introduced a new SERS nanoprobe, gold nanostars-decorated molybdenum disulfide, capable of tethering onto exosomes to enhance their Raman signal. [124] The system efficiently captured exosomes with a detection limit of 17 particles μL^{-1} and demonstrated good reproducibility with relative standard deviations under 9%.

Some works explored SERS as a DNA-related biosensor. For example, Ge et al. proposed a novel SERS substrate, Au@SiO_2, designed to detect the activity of DNA CpG methyltransferase (M.Sssl), a key enzyme in GC-associated DNA methylation processes. [125] The substrate was fabricated by picking up Au nanoparticle array and finite-different time-domain simulation using a monolayer SiO_2 array. For clinical applicability, 150 serum samples (30 breast cancer, 30 prostate cancer, 30 GC, 30 cervical cancer and 30 healthy) were analyzed to show a lower level of M.Sssl activity in healthy subjects,

associating its activity with cancer development. This innovative approach harnesses the sensitivity of SERS to monitor enzymatic activity, offering valuable insights into epigenetic modifications that could potentially serve as biomarkers for early GC detection.

Revolutionary work reported by Zhang et al. integrated clustered regularly interspaced short palindromic repeats (CRISPR) and branched hybridization chain reaction to form a novel one-pot signal amplification strategy (CRISPR/Cas13a) system. [126] The CRISPR/Cas13a system enhances the precision of the SERS technique, offering a powerful tool for detecting specific genetic sequences associated with GC. Additionally, the use of branched hybridization chain reaction (HCR) spontaneously pairs up in the presence of a single-stranded target nucleic acid, forming numerous hairpin structures, offering efficient signal amplification compared to traditional HCR. This process is valued for its simplicity and efficiency in amplifying signals without the need for complex enzyme reactions. [127–130] In their study, GC-related miR-106a was used to analyze serum samples (12 healthy, 12 atypic hyperplasia gastric mucosa and 24 GC). SERS spectra able to achieve a fast 60 min read-out for the detection of miR-106a in serum samples, even at low concentrations. This system can not only distinguish GC patients from healthy subjects, but also from atypic hyperplasia gastric mucosa patients, brightening the prospects of highly sensitive, fast, and non-invasive clinical diagnosis of early GC.

Wang et al. used SERS to detect increased Interleukin 8 gene (IL-8) expression in tumours, including gastric and breast cancer. [131] IL-8, crucial for angiogenesis and tumour development, is an important biomarker. [132] They developed a gold nanoparticle substrate with anti-IL-8 for capturing and used gold nanocages with modified anti-IL-8 as SERS tags. Higher IL-8 levels were observed in cancer patients' serum compared to healthy donors, validated by ELISA. However, the system couldn't differentiate between cancer types due to IL-8's non-specific expression, indicating a need for more specific biomarkers.

Small extracellular vesicles (sEVs) have emerged as promising biomarkers for GC due to their integral role in intercellular communication. Released by numerous cells, including cancer cells, into the extracellular environment, sEVs carry molecular cargo, including proteins, nucleic acids, and lipids, reflecting the physiological state of their cell of origin. [133,134] The distinctive molecular signatures present in sEVs hold the potential to unveil crucial information about the underlying pathology of GC. [135–137] Adding a captivating twist to the landscape of SERS-GC detection research, Liu et al. not only delved into the exploration of elevated levels of a novel sEVs. [138] The pioneering approach not only seeks to detect sEVs but also employs advanced ML techniques to discern the specific Raman spectral features indicative of GC-associated sEVs. This strategy not only contributes to the expanding repertoire of GC biomarkers but also showcases the potential synergy between SERS and ML in advancing the field of cancer diagnostics. Their ML algorithm demonstrated an impressive accuracy of 90%, 85%, and 72% when applied to tissue, blood, and saliva samples, respectively. It showcased the

ability to identify nine distinct types of small sEVs across these diverse sample types. Intriguingly, the study revealed that none of the nine identified sEV types were universally shared among all GC patients. The authors attribute this observation to the constrained sEV sample size inherent in their SERS system, emphasizing the need for larger and more diverse sample sets for comprehensive insights.

PCA is commonly used to reduce the dimensionality of SERS spectra and improve GC diagnostic accuracy. Several studies have investigated its application in optimizing performance or identifying superior methodologies. For instance, Guo et al. compared PCA with the characteristic ratio method (CRM) for distinguishing GC in SERS spectra from human serum samples. [139] CRM proved simpler and faster than PCA by utilizing intensity ratios directly from spectral peaks. Lin et al. utilized a PCA-Linear discriminant analysis (PCA-LDA) hybrid method to differentiate colorectal, gastric, and liver cancers from normal tissues. [140] Their study demonstrated the efficacy of SERS and PCA-LDA in detecting and distinguishing gastrointestinal cancers, corroborated by subsequent research. [141] Li et al. explored various classification algorithms, including PCA integrated with LDA, SVM, and CART, to differentiate GC from healthy and atrophic gastritis subjects. [111] Their findings highlight the nuanced performance and potential of ML-based methods like PCA-SVM and PCA-CART, despite CART's susceptibility to instability.

Recent research has broadened GC diagnostic biomarker discovery beyond traditional blood serum samples to include urine, saliva, and breath. Chen et al. utilized gas chromatography-mass spectrometry (GC-MS) to identify 14 volatile organic compounds (VOCs) in breath samples for distinguishing GC from healthy individuals, while Huang et al. employed a tubular SERS sensor system to detect eight VOC biomarkers indicative of GC. [142,143] In saliva, Chen et al. employed high performance liquid chromatography-mass spectrometry (HPLC-MS) to identify ten biomarkers and utilized SERS for spectral analysis, with Aslam et al. integrating these biomarkers into ML models to enhance GC detection accuracy. [144,145] These advancements signify the feasibility and efficacy of using alternative biofluids for GC detection, offering non-invasive methods that could revolutionize early diagnosis and staging. The integration of SERS sensor systems enhances sensitivity and specificity in detecting VOC biomarkers, promising broader applications in personalized medicine and population-wide screening programs.

In summary, SERS emerges as a transformative and versatile tool in the realm of GC research and diagnostics. Overcoming the limitations of conventional RS, SERS provides a powerful solution with its ability to enhance the Raman signal, enabling high-resolution and sensitive analysis. The application of SERS in GC detection not only outperforms traditional proteomic methods but also showcases remarkable progress in diverse sample types, including breath, urine, saliva, and blood serum. While challenges remain ongoing research attempts hold the promise of further refining SERS applications, making it an indispensable tool for precise and early diagnosis of GC in clinical settings. The dynamic

landscape of SERS in GC detection underscores its potential to overcome existing challenges and reshape the future of cancer diagnostics.

2.2.3. Fourier Transform Infrared Spectroscopy (FTIR)

FTIR is an analytical technique commonly employed to characterize a wide range of materials. [146] FTIR measures the interaction of molecules with infrared (IR) radiation at specific wavelengths and captures the vibrational and rotational modes of these molecules. This results in an IR absorption spectrum that acts as a unique FP of the sample. [147,148] Recent clinical research studies have delved into the utilization of FTIR as a diagnostic tool for various cancer types, capitalizing on its noninvasive, rapid, and cost-effective attributes. [149–151] In this section, we will delve into the prospective clinical applications of FTIR in the detection of GC and its potential for integration into clinical practice.

The capabilities of FTIR can be optimized through the incorporation of diverse accessories designed to meet specific requirements, including transmission, transflection and attenuated total reflection (ATR) modes. [152] While the transmission mode in FTIR spectroscopy enables the measurement of the entire sample thickness, it is important to note that the thickness for aqueous solutions is typically limited to 6 μm due to the strong absorbance of water. [152] As ATR-FTIR measures reflected light, it proves to be effective in analyzing samples with high absorption and thickness, which may hinder the transmission of IR radiation. [153] Moreover, it offers a shallower penetration depth and enables direct measurements of gases or fluids without complex sample preparation.

Shifting focus to the practical applications, Akin Geyik et al. explored the feasibility of attenuated total reflection-Fourier transform mid-infrared (ATR-MIR) spectroscopy coupled with chemometrics on paraffin-embedded tissues to rapidly diagnose gastric and colon cancers. [154] As the sole focus for this paper is GC, results regarding GC and healthy patients (22 GC and 20 healthy/gastric control patients) will be reviewed. To obtain diagnostic value in the molecular level, spectral parameters such as band area and its ratio, band position, band intensity (%T)/frequency and bandwidth were evaluated. To observe quantitative changes, spectral band area ratios showed an increase in band area ratios for lipid/protein, nucleic acids + phospholipids/ nucleic acids and total nucleic acid/ total protein in cancer groups. On the other hand, a decrease in lipid acyl chain length and amide-I/amide-II was reported. For qualitative information, analysis of band width values and position displayed a shift in lipid related band positions for cancer group. Similarly, the same trend was observed in protein, nucleic acid, and phospholipids related regions. These findings were compatible with the results in band area and intensity (%T)/frequency and band ratio. Thus, showing that the band position parameter could be implemented as a spectral biomarker for early diagnosis of GC. To identify spectral changes and differences between healthy and cancerous groups, they reported that the usage of unsupervised (PCA and hierarchical cluster analysis) multivariate data analysis showed successful separation. Moreover, soft independent modeling of class analogies was the ideal classification for diseased and control

groups, with 5% significance level and a total of 97.75% of tissue samples were correctly discriminated by LDA. However, further research on large patient cohort is necessary for clinical diagnosis.

Building onto the chemometric technique, Popescu et al. used a 2-dimensional infrared correlation spectroscopy to determine specific biochemical characteristics. [155] Their study utilized gastric malignant tissues obtained from 15 patients diagnosed with stage 3 and 4a GC. To classify tissue samples at a molecular level, they employed IR spectroscopy and observed higher band intensities at 1460, 1416, 1240 and 1087 cm^{-1} in normal tissues. In malignant tissues, they noted the absence of bands at 1380 cm^{-1} and the emergence of new band at 1210 cm^{-1}. Furthermore, there was a decrease and a slight shift from 1120 to 1121 cm^{-1}. Diving deeper, they computed spectral differences of band intensity ratios and band positions at I1640/I1550, I1640/I1460, I1400/I1460, I1310/I1240, I1160/I1120, I1080/I1240 and I1055/I1460 and were found to be a potential discriminant between malignant and normal tissues. For a more precise evaluation, they utilized two-dimensional infrared correlation spectra to obtain information regarding structural changes. Synchronous spectra displayed similar patterns at various stages of cancer evolution while asynchronous spectra were reported to have clear discrimination. Hence, the proposed data discrimination tool could be used as a screening tool for discriminating against cancer evolution stages. Despite promising results, the study suggests the need for further investigations using a larger sample cohort. Combining the 2-dimensional infrared correlation spectroscopy with proteomics or metabolomics methods would provide a more comprehensive understanding of biochemical changes associated with cancer.

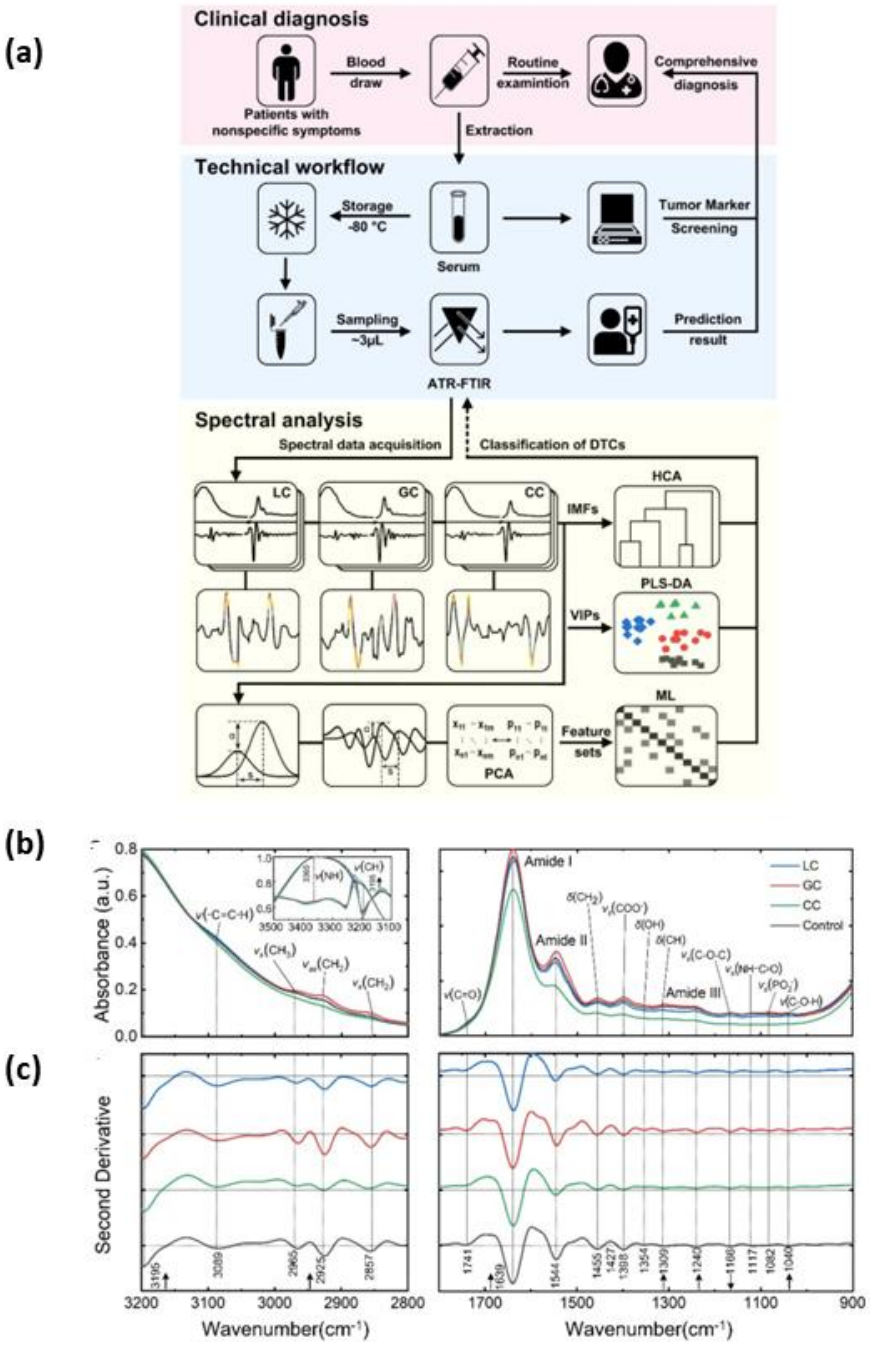

Figure 6. a) Schematic diagram of ATR-FTIR spectroscopy for serum sample testing and data mining pathways for accurate diagnosis of digestive tract cancers (DTC). The colored symbols (triangle, squares, etc.) represent different groups. b) Average ATR-FTIR spectra of different liquid DTCs, including control and liver cancer (LC), GC and colorectal cancer (CC) serum samples, labelled with absorption peaks corresponding to major molecular vibrations, including ν stretching, δ bending, s symmetric, and asymmetric vibrations. c) Average 2-derivative-FTIR spectra of DTCs and control samples, characterized by variations in the positions and relative contents of significant molecular compositions. *Reproduced with permission under the terms of the CC BY 4.0 license.* [156] *Copyright 2022, The Authors published by MDPI, Basel, Switzerland*

Guo et al. designed a data mining pathway using ATR-FTIR spectroscopy as a diagnostic tool for digestive tract cancers (DTC), which consists of: liver, gastric and colorectal cancers. [156] They

conducted in-depth analysis on 252 blood serum samples, focusing on in-situ FTIR spectroscopic variations, spectral peak absorbance, and wavenumber shifts. The proposed multi-dimensional diagnostic pathway can be observed in **Figure 6**a, employing various data mining techniques to reveal comprehensive information. Potential spectral markers were identified through quantitative variations in band location and relative absorbance of IR molecular FPs related to DTCs as depicted in Figure 6b. Compared to the control group, calculated second derivative-IR revealed biomacromolecule variations mainly in amide bands (1240, 1544, 1639 and 3365 cm^{-1}) as shown in Figure 6c, with significant red shift in amide I band by 2 cm^{-1}. These results were used to build a 2-dimensional second derivative IR spectrum dataset and compared with clinical tumor markers, primarily CEA and CA19-9 for GC detection. The GC group revealed an increase of 4.5% in relative absorptions at 1508 cm^{-1} and 1040 cm^{-1}, mirroring clinical CEA tests. Similarly, a significant increase was also observed in CA tests, where abnormal levels of CA19-9 were present. This mutual validation demonstrates that the 2-dimensional second derivative IR-based ML protocol enhances DTC classification performance. By employing selected data mining methods, PLS-DA and backpropagation neural networks were found to be highly effective in differentiating between DTCs and their stages with high sensitivity and specificity of 100%.

In a similar investigation, Guleken et al. looked into metabolic processes and how PCA could differentiate protein secondary structure. [157] The study utilised a diamond ATR crystal plate to assess 133 serum samples (45 colon, 45 GC and 43 control). Biochemical assays and spectroscopic results suggested that the total protein expressions were significantly lower in gastric and colon patients compared to the control group. Typical tumor markers for digestive organ cancers, including CEA, CA-125, CA 15-3, CA19-9, and AFP levels, were also examined to identify diagnostic serum protein markers. CA-19-9 was found to be a common tumor marker for both cancer groups. Furthermore, significant differences in CA-125, CA15-3 and CA19-9 were observed between the two cancer groups, with higher levels of CA19-9 in colon cancer patients. In order to differentiate between the two cancer groups, FTIR results showed structural and difference in amount for amide I and amide III. Using PCA analysis, scatter plots were clustered together with different magnitudes and directions. This indicated that metabolic processes were more pronounced in GC patients compared to colon cancer. Therefore, FTIR spectroscopy, along with curve-fitting analysis of amide I profile, could potentially be employed as tools for diagnosing both colon and GC patients.

Another study by K et al. utilized ATR-FTIR spectroscopy as a potential screening tool based on mathematical data manipulation techniques for distinguishing malignant and normal GC samples. [158] Paraffin-embedded tissues from 30 patients were scanned and displayed differences in absorption intensities at around 1200-1800 cm^{-1} and 3700 cm^{-1}. Malignancy was characterized by peaks mainly related to amide III and protein structure around 1285 cm^{-1} and 1339 cm^{-1}, δ (CH_2), lipids, fatty acids and δ (CH) at around 1439 cm^{-1}. They performed data modeling using PCA, SVM and KNN on 60 GC spectra and was able to distinguish normal and malignant samples to about 81.7%. While the study

demonstrates significant potential, further research is needed to examine whether samples encompass other types of cancers to confirm their validity.

Building onto the exploration of data manipulation techniques, Li et al. introduced a novel algorithm to discern between four distinct pathological categories of gastric tissues: normal, superficial and atrophic gastritis and GC. [159] The study comprised a cohort of 103 gastric tissue samples (35 chronic atrophic gastritis, 29 chronic superficial gastritis, 20 healthy individuals and 19 GC). FTIR data showed obvious differences in peak shape, intensity, and frequency between the four tissue groups. As conventional algorithms struggle to identify and classify closely related objects, they proposed the use of entropy weight local – hyperplane KNN based on frequency domain information. The algorithm combines adaptive weight local-hyperplane KNN with fine Fourier transform information in the frequency domain to distinguish similar targets. Hence, the proposed algorithm obtained the highest classification accuracy for GC, chronic atrophic gastritis, chronic superficial gastritis, and healthy tissues at 95.1%, 86.4%, 88.3% and 99% respectively, showing its effectiveness in classifying different tissue types. Similarly, Li et al.'s study explored the use of SVM in assessing the performance of FTIR for distinguishing between 54 gastric tissues (24 normal, 30 cancerous). [160] Using leave-one out cross validation, they evaluated the discrimination of SVM to have an accuracy of 92.2%, sensitivity of 100% and specificity of 83.3%. Both studies present promising evidence for GC diagnosis. However, coupling with other methods such as mid-infrared fiber optic spectroscopy or stomach endoscopy, along with expanding the study with a larger sample size could open promising avenues for clinical implementations.

By employing both light microscope and an FTIR spectroscope, Ullah et al. aimed to diagnose various cancer types, including, liver, stomach, breast, and ovary. [161] They adapted the microscope by using a He-Ne laser to capture 2-D images. Tissue samples were prepared, processed, and stained with H&E staining for microscopy imaging. Under light microscope, normal tissues typically exhibited regular arrangements while cancerous tissues tend to have several abnormalities in size and shape. In the case of GC, they observed irregular shape and fused neoplastic glands with intraluminal mucus and debris. Furthermore, FTIR data offered spectral information that claimed to effectively distinguish between normal and cancerous tissues. However, to enhance the comprehensiveness of the study, a more detailed explanation and conducting thorough comparison with normal samples should be done. Additionally, the inclusion of statistical analysis would further contribute to the overall strength and conclusiveness of the study.

In a pioneering study, Yi et al. introduced the use of Fourier transform near infrared (FT-NIR) spectroscopy to distinguish GC tissue samples. [162] Among 30 samples, FT-NIR revealed distinct differences between cancer and normal tissue in the CH-stretching second overtone (9000-7000 cm^{-1}), CH-stretching first overtone (6000-5200 cm^{-1}), and CH-stretching combination (4500-4000 cm^{-1})

regions. PCA of near infrared (NIR) spectra showed clear cluster trends, indicating a clear distinction between normal and cancerous tissue. Furthermore, through unsupervised pattern recognition, spectral data was able to be classified with accuracy, specificity, and sensitivity of 81.1%, 68.2% and 100% respectively. Hence, CH-stretching second overtone, CH-stretching first overtone and CH-stretching combination regions could be potential diagnostic biomarkers for GC.

Interestingly, Liu et al. explored the potential of FTIR spectroscopy on differentiating between normal and cancerous red blood cells. [163] They measured samples from 70 patients and identified four key peak-area ratios that differed significantly between the two groups. These ratios, A1653/A1543 (protein secondary structures), A1543/A2958 (relative content of protein and lipids), A1106/A1166 (structural and content changes in sugar) and A1543/A1106 (relative content of proteins and sugars), showed higher values in cancer patients compared to normal individuals. Further analysis using curve fitting revealed distinct differences in protein secondary structures and sugars between the two groups. Employing canonical discriminant analysis, FTIR spectroscopy was able to diagnose GC with sensitivity, accuracy, specificity, and PPV of 95%, 84.2%, 70% and 80.9% respectively. While these results suggest the potential of FTIR spectroscopy as a diagnostic tool, it is crucial to compare its performance against other established methods to validate its efficacy. Additionally, with 95% sensitivity and 70% specificity, the method may not be sufficiently reliable for clinical implementation. Exploring alternative ML data analysis techniques could potentially enhance the overall data results. Despite these limitations, the study provides some interesting preliminary evidence to be a potential diagnostic tool for GC.

Like many other cancers, GC spreads to the lymph nodes during its progression before advancing to other organs. This is explored in Dong et al.'s study, using FTIR as a diagnostic tool. [164] They obtained fresh lymph node tissues (80 normal and 80 metastatic) from 60 patients and measured using mid-infrared radiation with an ATR accessory. In malignant samples, they observed significantly higher signals at 1080 cm^{-1} related to nucleic acids, while signal at 1740 cm^{-1} related to lipids were lower compared to normal lymph nodes. Subsequent analysis using PCA, and Fisher's discriminant analysis showed that spectral results for the two groups could be classified. In lymph node metastasis, signals at 1080, 1400, 1740 cm^{-1} were decreased, while signal at 3260 cm^{-1} was higher. The identification algorithms could discriminate with a sensitivity and specificity of 96.6% and 93.8% respectively, demonstrating the potential of FTIR for diagnosing and potentially advancing GC treatment.

FTIR spectroscopy emerges as a promising diagnostic tool for GC, showcasing its ability to delineate spectral markers and molecular variations. From traditional FTIR to specialized techniques like ATR-FTIR or ATR-MIR, the method exhibits potential in discerning healthy and cancerous tissues. However, translating this technology into routine clinical practice requires larger patient cohorts encompassing various cancer stages and grades to validate its efficacy. Although recent studies have utilized diverse

sample types, the biological variability inherent in these complex specimens may lead to significant large background absorbance, potentially masking subtle spectral changes and hindering biomarker identification. [165] Nonetheless, with its noninvasive and label-free nature, FTIR stands out as a rapid and effective means for EGC detection.

2.2.4. Diffuse Reflectance Spectroscopy (DRS)

DRS is a valuable analytical tool for studying optical and physiological properties of biological tissues. DRS employs a broadband light source that results in tissue scattering and absorption. The latter is closely related to tissue chemical composition, while scattering is related to subcellular morphology. [166] The reflected light is then collected and transmitted via optical fibers to a spectrometer. Since the system uses white light, components are usually inexpensive and simple to manufacture. Additionally, the wavelength range of illumination falls between 320-900 nm, ensuring the safety of the method by filtering out ultraviolet (UV). [167] DRS offers a non-invasive, rapid, and cost-effective approach that has been instrumental in advancing cancer diagnostics. By analyzing the optical and physiological properties of tissues, DRS provides critical insights that aid in the detection and characterization of cancerous tissues. [168] While it has been explored for in-vivo for various cancer types, to our knowledge, no in-vivo studies have been conducted in GC patients until now. [169,170] Nevertheless, the potential applications of DRS in cancer diagnosis are vast and exciting. This technology can guide surgical procedures, ensuring more precise removal of tumors and reducing the likelihood of residual disease. Additionally, DRS can monitor the effectiveness of treatments by detecting changes in tissue properties over time, allowing for timely adjustments in therapeutic strategies.

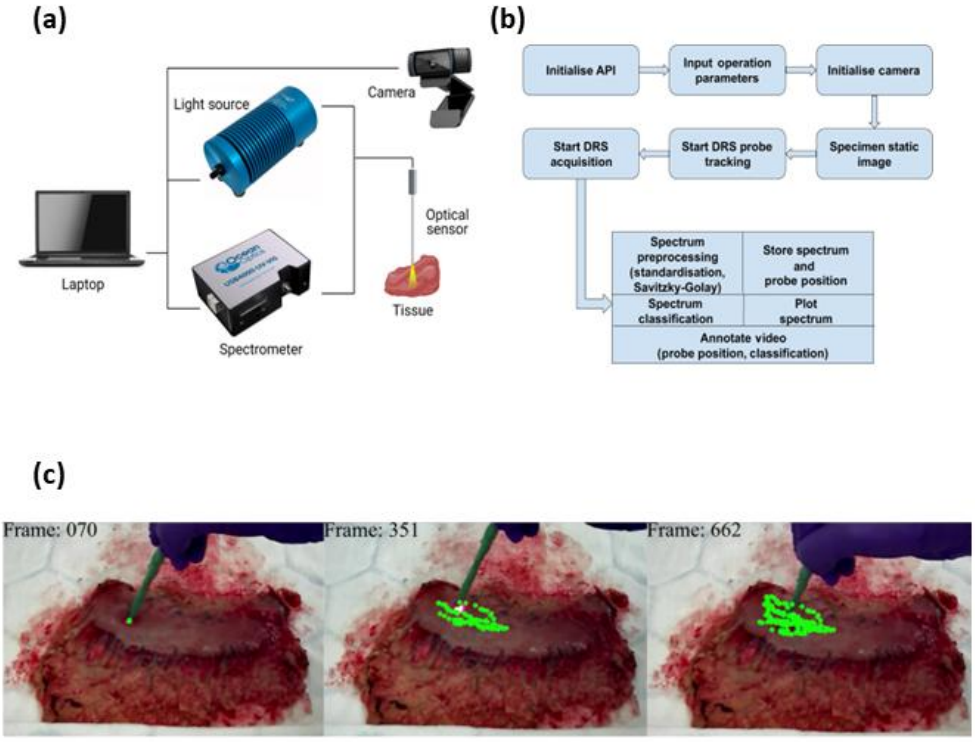

Figure 7. a) A schematic diagram of DRS instrumentation. B) Overall workflow for ex-vivo spectral acquisition. C) Real-time tracking with a DRS probe and classification at various frames during measurement of ex-vivo gastric specimens. *Reproduced with permission under the terms of the CC BY license. [171] Copyright 2022, The Authors published by SPIE under Creative Commons Attribution 4.0 Unported License.*

While DRS holds promise in distinguishing between healthy and diseased tissues, it lacks the ability to mark tissue sampling locations, a crucial factor for surgeons to determine the resection margins. To address this, Gkouzionis et al. developed a real-time tracking handheld system to assist in the classification of tumor and non-tumor tissues in GC and esophageal cancer patients. [171] The proposed DRS system comprised of a reflection probe connected to a tungsten halogen light source (360 to 2400 nm) around one light collection fiber, connected to a spectrometer, a schematic diagram of the set-up can be seen in **Figure 7**a. An overall workflow is illustrated in Figure 7b. To provide real-time tracking, they introduced a Kalman filter and green marker on suspected normal tissues, which is illustrated in Figure 7c. Live video feedback on ex-vivo tissue samples from 26 patients facilitated real-time visualization and spectral acquisition with a root mean square error of 1.18 ± 0.58 mm, 1.05 ± 0.28 mm in x and y dimensions respectively, and a maximum measure error of 1.76 mm. Additionally, the real-time tracking system had a diagnostic accuracy for classifying GC at 94%, highlighting its clinical value. Using various ML classifiers, XGB emerged as the most effective in achieving diagnostic accuracy, sensitivity, and specificity of 93.86 ± 0.66, 91.31% and 95.13% respectively. Nonetheless, there were limitations, particularly regarding the potential challenges of color marker tracking in an in-vivo setting due to uncontrollable background colors. Future enhancements involving deep learning

models and improved visual information, such as three-dimensional spectroscopic data could enhance the system's clinical applicability.

These results were further substantiated by Nazarian et al.'s study, where they employed a handheld reflection fiber probe on ex-vivo gastric and esophageal tissue samples. [172] Equipped with 6 peripheral illumination fibers, in combination with a visible and NIR spectrometer, spectral acquisition was performed on 34 patients. Optical tracking through a Kalman filter was implemented to ensure localization of biopsy sites on tissue specimens. To assess the performance, various supervised ML classifiers were utilized, with histopathological analysis serving as the ground truth. Notably, the XGB classifier exhibited the most favorable results for stomach tissue classification, achieving an overall diagnostic accuracy, sensitivity, and specificity of 93.86%, 91.31%, and 95.13% respectively. Furthermore, the classifier had an AUC of 0.974. All in all, the proposed DRS probe, in combination with a tracking system and ML, enabled real-time discrimination between normal and GC stomach tissues with an overall accuracy of 93.9%. Moreover, real-time classification system could provide live feedback on screen, indicating the type of tissue being sampled. Thus, the proposed DRS system holds great promise for intraoperative use to aid margin assessment during surgery with the usage of XGB as a classifier.

In summary, DRS is a swift and cost-effective tool for GC diagnosis, offering enhanced diagnostic precision. Its broad-spectrum approach and real-time tracking systems show promise for intraoperative use. However, DRS lacks tissue sampling location marking, a critical drawback for surgical planning. Despite these limitations, DRS, when integrated with advanced technologies, holds potential for precise diagnostic insights in clinical applications, notably in GC surgery.

2.2.5. Fluorescence Spectroscopy and Imaging

Fluorescence imaging and spectroscopy introduced earlier have also been applied in several compelling in-vitro studies for GC diagnosis and staging, gastrectomy or lymphadenectomy during surgery, and treatment. This section includes diagnostic methods using spectral analysis based on biochemical assessments conducted in-vitro. 5-ALA based PDD analysis is also conducted in-vitro to obtain results for biopsied GC samples in the following section. Fluorescence techniques coupled with laparoscopy prove effective for tumor removal, gastrectomy, or guide SNNS. Some note the spectral biochemical differences which can establish potential GC biomarkers. Some methods use label-free biomarker detection while most of the techniques use staining and exogenous fluorophores. Multiphoton microscopy (MPM) discussed in the end of this sub section relies on endogenous fluorophores.

The usage of PS as introduced by Loshchenov et al., increases the detection efficiency but impairs the objectivity due to photobleaching effect under light exposure. [92] As such, Yamashita et al. investigated the photobleaching effect of 5-ALA PDD for GC. [173] Biopsied tumor and non-tumor regions, were excited using a UV light source of 410 nm. The collected emission spectrum revealed a sharp peak at

630 nm and a broad peak ranging from 660 nm to 700 nm. The peak changes due to photobleaching reveal a quick decrease in the sharp peak at 630 nm and a slower decrease in the broad peak. Therefore, the study concluded that the average fluorescence height of the peak from 660 to 700 nm was effective in objectively differentiating tumorous and non-tumorous tissues due to its reduced influence on photobleaching.

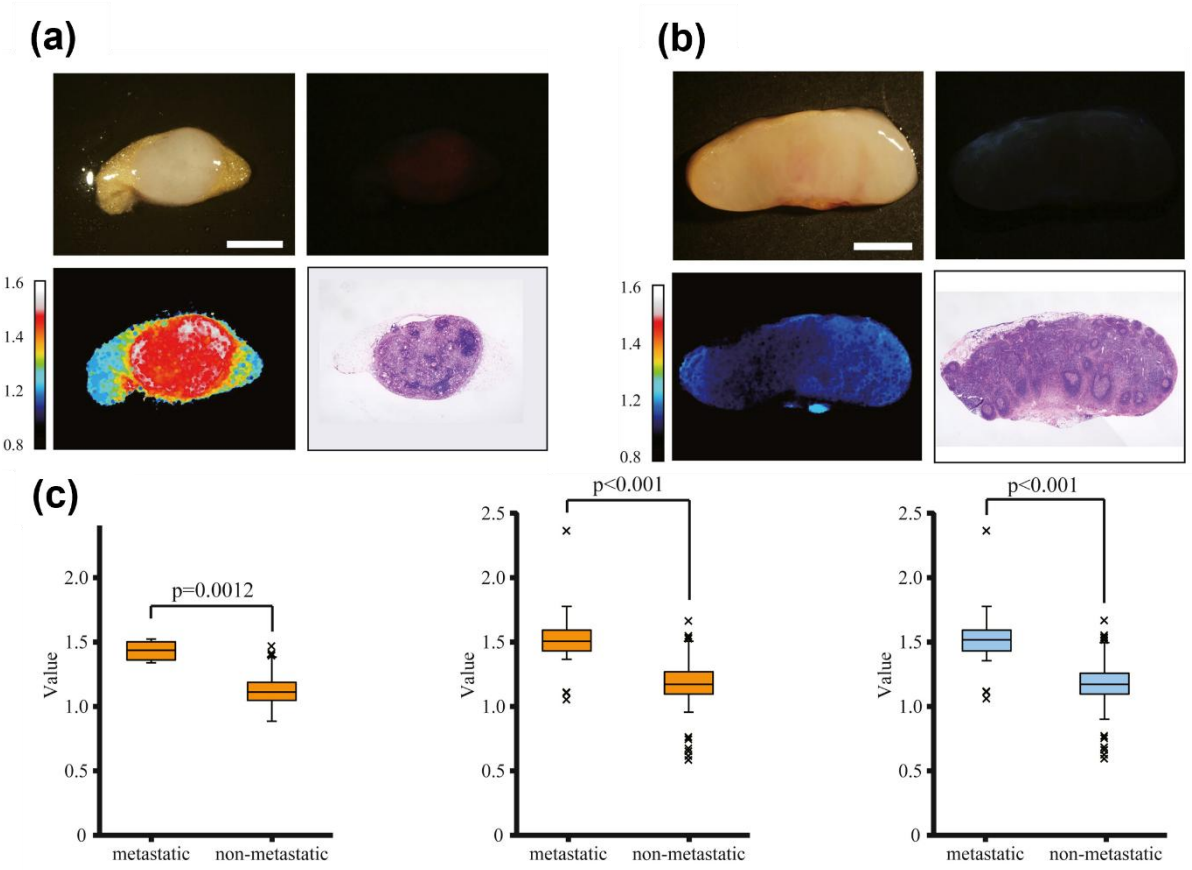

Figure 8. Illustrations capturing a) metastatic and b) non-metastatic lymph nodes. In a) and b), upper left: white light image, upper right: fluorescence image, lower left: ratioed ratio image, and lower right: H&E-stained microscopic image. A) and b) display that metastatic lymph nodes exhibited increased signal intensity in the ratioed ratio image, consistent with metastatic lesions detected by H&E images, along with red fluorescence in the fluorescence color image. C) Indicates the higher values of ratioed ratio images in metastatic as compared to non-metastatic lymph nodes for differentiated type, non-differentiated type and in total groups from left to right. *Reproduced with permission, [174] Copyright 2016, Elsevier.*

In a separate study, Koizumi et al. developed a novel imaging strategy for the detection of metastatic lymph nodes using fluorescence spectral imaging of excised lymph nodes in GC patients, while minimizing autofluorescence. [174] Fluorescence excitation was done with 405 nm laser and 436 nm laser for irradiation, facilitating the photo-oxidation from PPIX to PPP, resulting in spectral changes. Spectral images were obtained through a dichroic mirror longer than 458 nm and band pass filters for 635 nm or 675 nm, corresponding to PPIX and PPP. Ratio images (intensity at 675 nm/ intensity at 635 nm) were captured before and after irradiation. Double ratio images were then obtained by dividing the post-irradiation by the pre-irradiation ratio images, revealing elevated signal intensity in metastatic

lymph nodes compared to non-metastatic lymph nodes which were consistent with H&E-stained images as illustrated in **Figure 8**a-c. Examination of 662 lymph nodes from 30 patients resulted in 38 metastatic and 624 non metastatic lymph nodes. Through ROC analysis, diagnostic accuracy, sensitivity, and specificity of 90.8%, 91.9% and 90.8% respectively were achieved. This rapid lymph node diagnosis with reduced photooxidation effect could pave the way for less invasive intraoperative surgery. However, PPIX exhibits increased fluorescence even in cases of inflammation without metastasis posing challenges in diagnosis. Therefore, although 5-ALA- based diagnosis is vastly used for detecting malignant tumors and metastatic lymph nodes, the fluorescence from metabolite PPIX is consistently affected by the autofluorescence of tissue chromophores and decreased reliability in differentiating non-metastatic inflammation. [175]

Biomarkers for GC like proteins, amino acids, and lipids have been extensively studied through various mass spectroscopy, western blot, and other proteomics studies. Liliac et al. studied the synthesis and degradation of protein E-Cadherin in tumor grading using multispectral microscopy and fluorescence deconvolution microscopy. [176] Analyzing 18 patient tissue samples with poor to well differentiated tumor GC samples and 5 normal gastric mucosa, they utilized a Nikon 90i motorized microscope with a CMOS camera, multispectral camera, and LED fluorescent modules. 10 random images from each fluorescence-stained slide were captured through sequential scanning with selective filters to avoid fluorophore overlap. Subsequently, images were processed with deconvolution algorithms, revealing the presence of E-cadherin in the membrane, cytoplasm, Golgi vesicles and lysosomes. Notably, they also demonstrated a novel discovery of trafficking lysosome associated membrane glycoprotein 1-positive exosomes or vesicular bodies across the tumor cell membranes. Overall, all these E-cadherin metabolism pathways offer valuable considerations for future studies in histopathological samples or in-vivo diagnosis and treatment.

In addition to proteins, the exploration of potential of amino acid GC biomarkers has been a focus in various studies. An example is Wang et al.'s study, where they identified differences in spectral FPs from biopsy samples of 18 colorectal cancer patients and 18 GC patients, comparing them with normal tissues. They analyzed samples using native fluorescence (NFL). [177] NFL is a type of optical biopsy technique which uses RS or fluorescence Stokes shift spectroscopy (S^3) to identify differences in tissue samples. They employed a Perkin-Elmer luminescence spectrometer model LS-55 to detect emission spectra generated from excitation with wavelengths across ~280 nm to 700 nm. Key fluorophores analyzed included tryptophan, collagen, reduced nicotinamide adenine dinucleotide hydrate (NADH), flavin and porphyrins. Malignant tissues exhibited lower spectral intensity compared to normal tissues, attributed to reduced mucosal collagen fluorescence and increased blood absorption. From the NFL spectrum, the ratio of intensities at 340 nm and 440 nm surpassed 4.5 for malignant tissues and remained below 4.0 for normal tissues. Additionally, the stokes shift spectra of these tissues displayed reduced intensities in the tryptophan, collagen, NADH wavenumber regions, while exhibiting gradual increase

beyond normal spectra in the porphyrin wavenumber region. By using non-negative biochemical component analysis for NFL and S^3, changes in the key fluorophores with cancer and normal tissues could be identified. Tyrosine, tryptophan, and collagen have been studied as biomarkers using proteomics, showing higher levels in the serum or gastric juice of GC subjects as compared to control groups. [178,179]

In another application of fluorescence spectroscopy for biochemical analysis, introduced earlier in the in-vivo section, Angelova et al. also measured intrinsic autofluorescence and exogenous fluorescence in-vitro on excised gastrointestinal tract neoplasia tissues. [93] A spectrofluorometry system was used to measure the excitation and emission spectra, along with the excitation emission matrices (EEM), with excitation in the range 280 nm to 440 nm and emission in the range 300 nm to 800 nm. The EEM showed that amino acids like tryptophan and tyrosine were excited by 280-300 nm and emitted at 320-360 nm; proteins like elastin and collagen were excited by 320-360 nm and emitted at 400, 460-500 nm. The usage of these amino acids and proteins as biomarkers for GC has been validated with proteomics studies mentioned above. [178,179] Overall, autofluorescence in the tumor area was lower than in normal mucosa. This study demonstrated satisfactory results, better accuracy and visualization can be achieved with exogenous fluorophores like PPIX. While these studies highlight variations in spectral intensity, they lack quantitative assessments for the biochemicals. Hence, further improvements to spectral unmixing to obtain relative amounts that can be compared with the trend obtained with gold standard proteomics can be fruitful.

In the field of two-photon microscopy, Juvekar et al. developed an NIR emissive two-photon ratiometric probe for pH analysis in stomach tissues. [180] Comprising of a two-photon active hemicyanine core (HCC), the probe emitted double NIR bands dependent on the pH range. The fluorescent probe (HCC1) used for ex-vivo analysis on normal, adenoma and cancer tissue displayed changes in the optical output for small pH variations in the stomach tissue. Ratiometric two-photon microscopy images (I_{680}/I_{618}) indicated higher ratio values for non-cancerous lesions, representing a pH of ~7.4. In contrast, adenoma and cancerous tissues showed low ratio values for pH of 7.7 and 8.1 respectively. It was concluded that high-resolution images with minor pH changes could be obtained, and this can serve as a potential diagnostic tool for early stomach cancer.

Using a new persistent luminescence nanoparticle, Wang et al. introduced a novel methodology to detect lysosomes with minimal autofluorescence interference. [181] They synthesized Zn_2GeO_4:Mn (ZGO:Mn) persistent luminescence nanorods, whose length can be tuned by adjusting pH. Subsequently, the aptamer- guided ZGO:Mn bioprobes were applied to serum samples from gastric, lung, colorectal cancer patients and healthy donors. The results showed enhanced luminescent signals, particularly pronounced in cancer serum due to higher lysosome levels. The bioprobes used were able to retain luminescence for tens of minutes, eliminating serum autofluorescence. Moreover, the results

obtained were also consistent with clinical ELISA results, suggesting the potential clinical applicability of such nanoparticle-based detection.

Using indocyanine green (ICG) fluorescence to determine accurate tumor location has been a widespread practice in gastrectomy. [182] To further enhance sensitivity, specificity, and accuracy many studies have developed advanced fluorescent technologies. This is exemplified in Kim et al.'s study for the detection of sentinel lymph node for SNNS in 28 EGC cases using NIR ICG fluorescent method. [183] The lymph nodes were excised with the existing dual tracer method and then assessed using the multispectral fluorescence organoscope (Animascope) equipped with white light, a 635 nm laser, and an 808 nm laser. Fluorescent images were captured using a camera and results were compared with the traditional dual tracer method. Any value above 10% of the maximum fluorescence value was considered a sentinel node. Out of a total of 443 lymph nodes from 28 subjects, 184 sentinel nodes were identified using the dual tracer method. The NIR ICG method achieved a sensitivity of 98.9% and a specificity of 76%. Despite a relatively high false positive rate of 25.6% compared to the dual tracer method, this approach shows promise as a tool for sentinel node detection during SNNS, offering accurate and safer detection without radiation hazards.

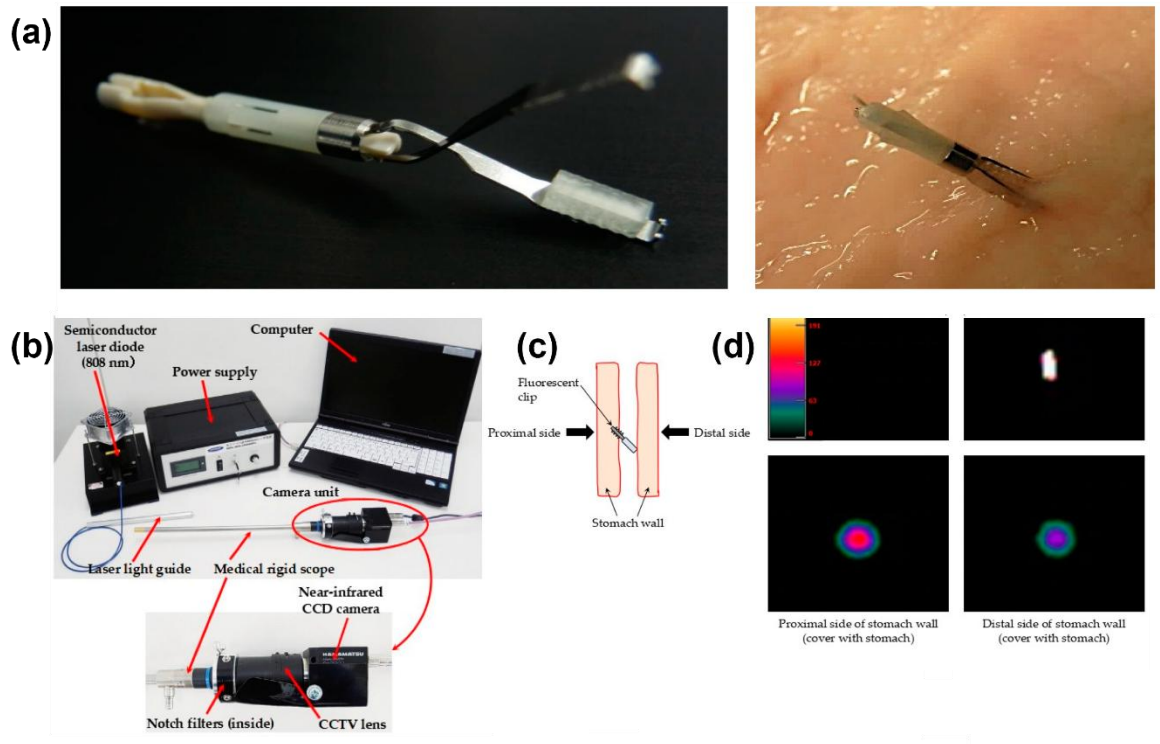

Figure 9. a) Image showing the fluorescent clip with the phosphor (left) and its attachment to the human stomach mucosa ex-vivo (right) b) Image representing different elements of the laparoscopic fluorescent detection system. c) representation of the detection method of the phosphor clip in the stomach d) Fluorescent images of the phosphor clip from the proximal and distal side. *Reproduced with permission under the terms of the CC BY 4.0 license. [184] Copyright 2019, The Authors published by MDPI, Basel, Switzerland*

Aimed at enhancing gastric tumor identification, Inada et al. developed a clip-based fluorescent detection system to improve the accuracy of tumor detection during laparoscopic surgery. [184] The glass

phosphor clips (Bi_2O_3-B_2O_3-based glass doped with Yb^{3+} and Nd^{3+}) were designed in three different shapes, selecting only the shape that exhibited the highest fluorescent intensity (measured with a power meter) upon irradiation with an 808 nm laser. This was then implanted in pig and human stomach mucosa in two ex-vivo experiments. The chosen glass phosphor shape, and its implantation to human mucosa is shown in **Figure 9**a. A CCD camera and CCTV lens were attached to a medical scope for detecting NIR signals around 1000 nm, as shown in Figure 9b. The fluorescence intensity observed in the clip increased with the rise in excitation light power. This phenomenon was effectively detected in experiments with pig and human mucosa from both the proximal and distal side (method of detection illustrated in Figure 9c), with the former exhibiting greater fluorescence intensity as represented in Figure 9d. Despite the presence of blood stains and a thicker wall (10mm) in freshly cut human stomach tissue, fluorescent intensity was detected. While this technique is in its preliminary stage and requires practical adjustments for a detection distance of 6-8 cm, it presents a promising tool for accurate laparoscopic navigation surgeries with tumor detection from outside the stomach. Further experimentation of this technique in tumor cases is needed to validate its efficacy.

In a study on different treatment mechanisms for GC, Liang et al. investigated the expression level of mRNA miR-124-5p in GC and its adjacent tissues using real-time fluorescence PCR. [185] The tissue samples were collected from 50 GC patients during surgery. The study also examined the effect of miR-124-5p on GC cell (SGC-803 and SGC7901) proliferation, metastasis and its correlation with migration and invasion enhancer 1 (MIEN1) using 3-(4,5-dimethylthiazol-2-yl)-2,5-diphenyltetrazolium bromide and scratch wound healing assay tests. The findings revealed that miR-124-5p expression was significantly lower in GC tissues as compared to adjacent tissues, and an increasing miR-124-5p level with higher GC stage. The cell studies demonstrated that metastasis and proliferation of SGC7901 was inhibited with the miR-124-5p, and SGC803 was promoted with the miR-124-5p inhibitor. Moreover, miR-124-5p negatively modulated the MIEN1 expression in both GC cells. Although suggesting miR-124-5p as a novel molecular target for GC treatment, the study's ex-vivo nature emphasizes the need for further investigation before considering human applications.

Multiphoton Microscopy (MPM)

Another fluorescence-based optical technique frequently used in the detection of GC is known as MPM imaging. MPM relies on the tissue's intrinsic fluorescent properties, providing label-free imaging based on intracellular two-photon excited fluorescence (TPEF) and second harmonic generation (SHG). MPM provides real-time 3D images proving to be highly valuable for imaging live biological tissues. This technique has been employed in numerous research studies for gastric tumor imaging, and comprehensive reviews by Wang et al. and Li et al. showcase its versatility. [186,187]

The application of this label-free imaging technique in the detection of GC was demonstrated for the first time by Wu et al. [188] They obtained 20 normal and 15 intestinal metaplasia (IM) gastric tissue

samples from 17 subjects through endoscopic biopsy and imaged them using a commercial laser scanning imaging system (Zeiss LSM 510 META) with an excitation laser of 800 nm. The identification of cancerous tissues was based on goblet cells with non-fluorescent mucin. Additionally, the population density of goblet cells was quantified, revealing a significantly higher number in IM tissue. This suggests that the proposed method could be used as a diagnostic feature for IM, overcoming the drawbacks of current gold standard techniques like histopathology which cannot be performed in-vivo, and WLE which lacks clear visibility for distinguishing between normal and cancerous tissues. While MPM-based endoscopy offers promising advantages for IM diagnosis, considerations include its small field of view (FoV) and low-resolution characteristics. Furthermore, the study does not demonstrate any in-vivo applications of the MPM.

Comparing MPM with current clinical usage for patients with T4 stage of GC (tumor invasion into the serosa or adjacent organs), Yan et al. tested the optical diagnostic features of serosal invasion using MPM, H&E staining and Masson's trichrome staining on 20 GC samples obtained using biopsy. [189] The findings showed significant differences in features such as collagen structure, size, and shape between the cells with and without serosal invasion. The collagen content in cells with invasion (0.36 ± 0.18) was significantly lower than the one without serosal invasion (0.79± 0.16). A blinded study of 60 patients was also performed to achieve a diagnostic accuracy of 93.33%, a sensitivity of 90% and a specificity of 96.67% compared with endoscopic ultrasonography. These promising results show the possibility of using MPM for real time optical diagnosis of T4 stage cancer.

Using collagen quantity along with the morphological changes to differentiate tumor and normal cells, He et al. optimized MPM imaging to have an excitation wavelength of 810 nm for the high contrast of TPEF and SHG simultaneously. [190] Two channels, one for collagen (393-414 nm) and another for tissue morphology (438-708 nm) were selected. They studied nuclear boundaries for sub cellular distinction and obtained collagen content from ratio of SHG pixels to all pixels. The nuclear area was significantly different in tumor and normal cells with 32.01 ± 2.89 and 58.41 ± 6.06 μm^2 respectively. The collagen content also showed significant difference with a high quantity of 0.087 ± 0.012 in normal and a much lower quantity of 0.020 ± 0.007 in cancerous mucosa, which was a consistent trend in many studies. As verified with histopathology, MPM could be used for differentiating tumor and normal tissues morphologically and quantitatively; and this could further be extended to cancer staging application. While this study recommends the integration of MPM with an endoscope for real-time in-vivo assessment, all the studies documented are done in-vitro and hence, further research is required before it can be translated in-vivo and real-time clinical applications.

Another advancement of MPM called spectral resolved MPM (SMPM) was developed by Li et al. SMPM was used on 7 patients (3 normal gastric mucosa, 3 intestinal-type adenocarcinoma and 1 neuroendocrine carcinoma) to obtain detailed structural and functional tissue information. [191] The

results showed a distinction between different sub-structures of gastric mucosa and different types of malignant GC tissues. In a follow-up study, the group also conducted the imaging of 12 specimens: 3 normal, 4 chronic gastritis erosion, 2 chronic gastritis IM and 3 intestinal-type adenocarcinoma using spectral and time-resolved MPM (STMPM). [192] The STMPM system is shown in **Figure 10**a. The results showed that based on the endogenous contrast of these tissues, the structural and biochemical properties of gastric mucosa obtained through STMPM were able to characterize different categories as depicted in Figure 10b, which also corresponded to H&E-stained images. Although this technique has great potential for clinical translation, the sample size of this study is very limited.

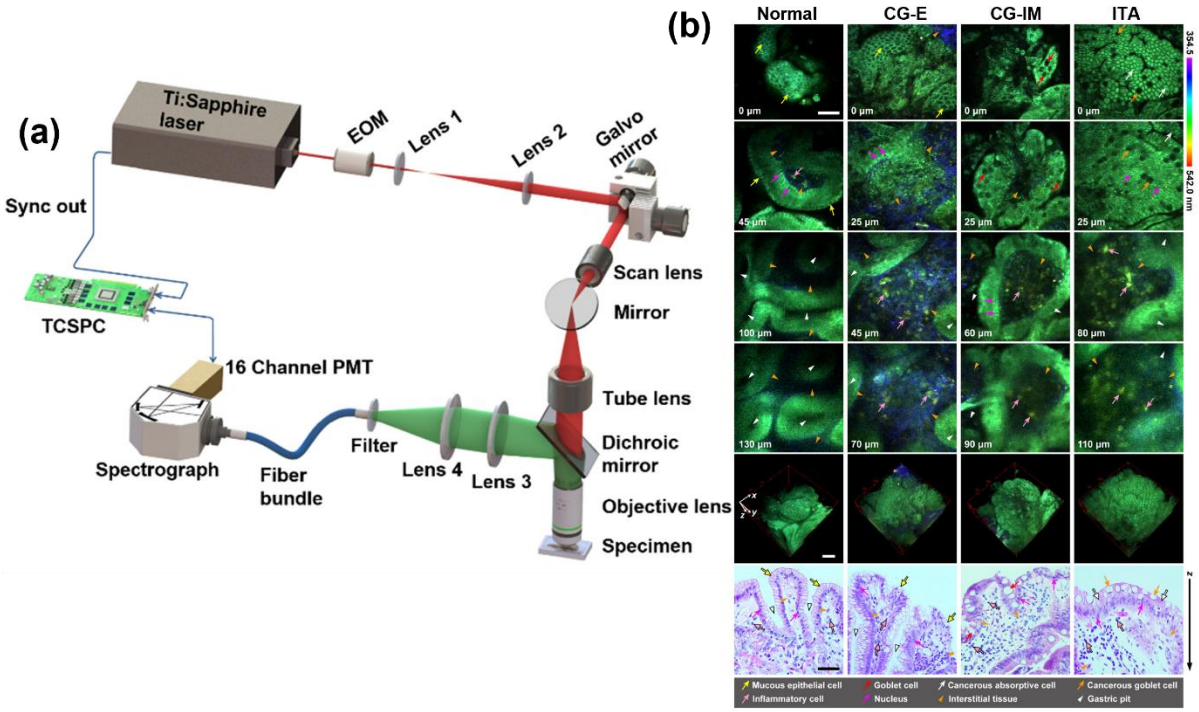

Figure 10. a) Experimental setup of the spectral and time-resolved multiphoton imaging system b) Spectral resolved MPM 3D images of normal, chronic gastritis- erosion (CG-E), chronic gastritis – intestinal metaplasia (CG-IM), intestinal adenocarcinoma (ITA) compared with the traditional H&E images (bottom). *Reproduced with permission [192] Copyright 2018, Optical Society of America under the terms of the OSA open access publishing Agreement.*

In another study, Li et al. studied the diagnosis of early-stage GC using fluorescence combined with HSI technology. [193] They used a hyperspectral microscopy imaging system to obtain fluorescence spectral images of 76 gastric tissue samples with 32 non-atrophic gastritis, 15 premalignant lesions and 29 diagnosed GC cases obtained through biopsy during a gastroscopic examination. For each patient, 116 frames (256 order grayscale) at every 2 nm interval between 450-680 nm range was acquired with a UV xenon light source with a central wavelength of 361 nm. The spectral differences from these categories were noticed in their results. They combined it with PLS-DA and SVM for a more reliable classification model. They conclude that the SVM model was significantly better than the PLS-DA with accuracy, specificity, and sensitivity above 94%.

Utilizing the same system, in a follow up study, they acquired spectral images of different gastric mucosal tissues, which were obtained from 120 patients (53 non-precancerous, 35 precancerous samples, and 32 GC samples) through biopsy during a gastroscopic examination on. [194] The spectra and its second derivative from a 10x10 pixel matrix for each tissue category were analyzed, resulting in spectral differences due to the abnormal metabolism of pyridoxal phosphate "Schiff" base, hematoporphyrin IX and Nicotinamide adenine dinucleotide phosphate (NADPH) concentration. These can therefore be used as biomarkers to distinguish the 3 categories. To improve the classification, they developed a deep learning 34-layer residual network (ResNet) which was trained with spatio-spectral images of the 10 x 10 pixels to get a classification accuracy of 96.5 %, specificities of 96.0%, 97.3%, and 96.7% and sensitivities of 97.0%, 96.3%, and 96.6% for non-precancerous, precancerous and GC groups, respectively.

Fluorescence spectroscopy studies mentioned above show promising advancements in the detection, staging, surgery, and treatment of GC. While staining-based fluorescence measurements such as ICG and PPIX demonstrate higher accuracy, their reliance on external fluorophores limits their safe application in clinical settings. The introduction of MPM as a label-free technique holds great promise for clinical fluorescence applications. However, all current studies are limited to ex-vivo or in-vitro settings and should advance into in-vivo clinical testing.

2.2.6. Optical Coherence Tomography (OCT)

A fundamental OCT system comprises of a low coherence light source and a beam splitter that splits light into two parts: one aimed at the sample under examination and the other at a mirror. [52] Much like ultrasound, this imaging technique directs waves towards the tissue of interest. These waves bounce off the tissue structure and the time delay of the resulting backscattered light is subsequently analyzed using an interferometer to determine the depth at which the reflection occurred. [195,196] Cross-sectional images are obtained through scanning incident light at different transverse positions. [197] Notably, OCT utilizes NIR light, which travels much faster than ultrasound. With a typical resolution of ~ 20 µm, much higher than ultrasound or magnetic resonance imaging, OCT provides high-resolution and image visualization in real-time as well as at video rate. [196] Thus, such capabilities enable early disease detection and precise monitoring without being invasive, making it an indispensable tool in medical diagnostics. Although preliminary studies on the in vivo detection of gastrointestinal cancer have been conducted using OCT, no in vivo studies specifically addressing GC detection have been reported. [198–201] Therefore, in this section, we will discuss the implementation of OCT in the context of GC detection using ex vivo methods.

Recent research has explored the potential of OCT images, in conjunction with ML algorithms, for identifying cancerous tissues. A study by Luo et al. employed a swept source optical coherence tomography (SS-OCT) in biopsied samples after a laparoscopic surgery to image 12 patients (5 GC and

7 colon cancer). [202] Their system employed a scanning light source emitting wavelengths at 1260 nm to 1360 nm at a repeat rate of 100 kHz, with a balance detector. The OCT images revealed distinct structural layers in the normal tissues, clearly differentiating the mucosa, submucosa and muscularis propria layer. In contrast, tumor tissues exhibited irregularities, indicating their heterogeneous nature. These findings were validated through histopathology, demonstrating that the variations in texture observed in OCT images corresponded with pathological sections. Therefore, this study highlighted the potential of OCT as a viable imaging modality for cancerous tissue characterization.

As the previous study was focused on using SS-OCT images to assess the heterogeneity of tumor tissues, Luo et al. expanded the scope by incorporating quantitative parameters derived from OCT images into a multi-faceted classification approach. [203] Their SS-OCT system was employed to obtain images of ex-vivo tissue samples from 14 patients (6 normal, 8 cancerous). Image analysis revealed distinct characteristics: cancerous tissue displayed heterogeneous texture and exhibited significant degeneration and fragmentation, whereas normal tissue appeared visibly smooth with homogeneous intensity distribution. From each OCT image, five quantitative parameters were extracted and utilized as feature vectors for five different types of classifiers: SVM, KNN, RF, logic regression and threshold classification. This multi-faceted approach successfully classified cancerous tissue from healthy tissue, achieving high specificity and sensitivity of approximately 90% or more. This promising outcome suggests that morphological feature analysis-based classification holds significant potential as a computer-aided diagnostic tool for GC.

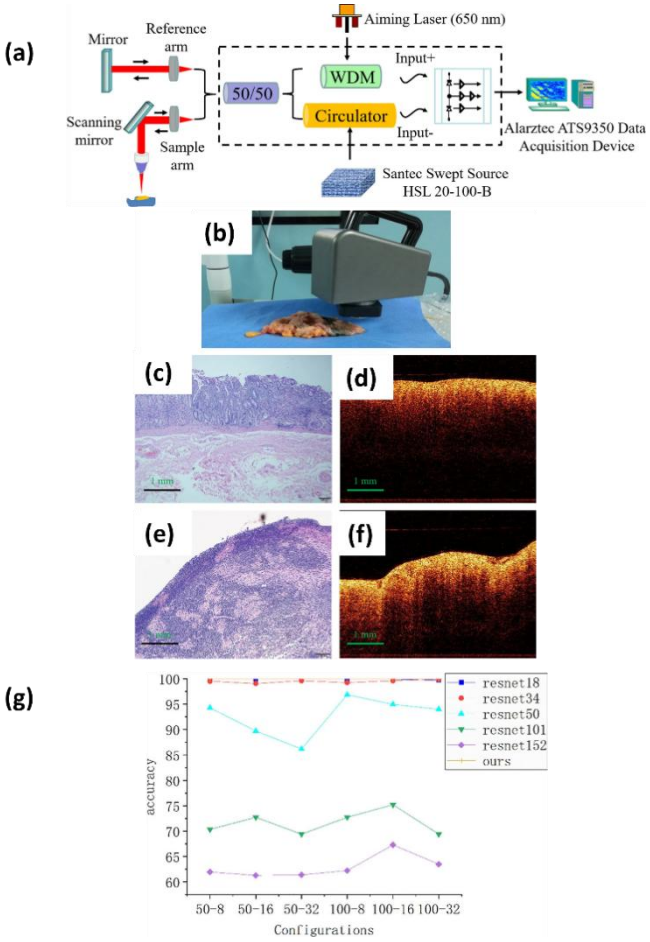

Figure 11. a) Illustration of SS-OCT system for the collection of gastric tissue images (WDM is the wavelength division multiplexing) b) Scan probe for the acquisition of gastric cancerous tissue sample c) Histological image of normal gastric tissue d) OCT image of normal gastric tissue e) Histological image of cancerous gastric tissue f) OCT image of cancerous gastric tissue g) A graph comparing accuracy between various model configurations. *Reproduced with permission* [204] *Copyright © 2022, The Author(s), under exclusive license to Springer-Verlag London Ltd., part of Springer Nature.*

Luo et al. also employed a deep learning approach based on a residual network architecture and an optimized version of ResNet18 network to classify GC OCT images. [204] The SS-OCT system used in this study can be seen in **Figure 11**a. OCT images of gastric tissues (5 normal, 6 cancerous) were captured after removal, an example of this set-up is illustrated in Figure 11b. Subsequently, tissue samples were subjected to standard pathological analysis shown in Figure 11c and e. The proposed technology revealed a smooth and uniform layer for normal tissue samples, while cancerous tissues exhibited a disordered pattern as depicted in Figure 11d and f. This shows a marked difference between normal and cancerous tissues. Compared to ResNet18, the proposed classification method achieved similar accuracy of 99.90% illustrated in Figure 11g. However, the proposed model outperforms the standard ResNet18 due to fewer parameters and shorter training time. Additionally, it surpassed five other classifiers, reinforcing their superiority as the optimal model for this study. Through its extensive comparisons with existing classification techniques, the study demonstrates the potential of OCT in clinical applications. Despite these advances, OCT imaging remains relatively limited in terms of clinical applicability when employed in-vivo. Further research is needed to advance the application,

particularly given its advantages of providing real-time imaging without the need for staining. Future studies could also focus on acquiring more clinical OCT images and exploring endoscopic OCT as a means of enhancing tissue examination. With continued development, OCT has the potential to revolutionize cancer diagnosis and treatment.

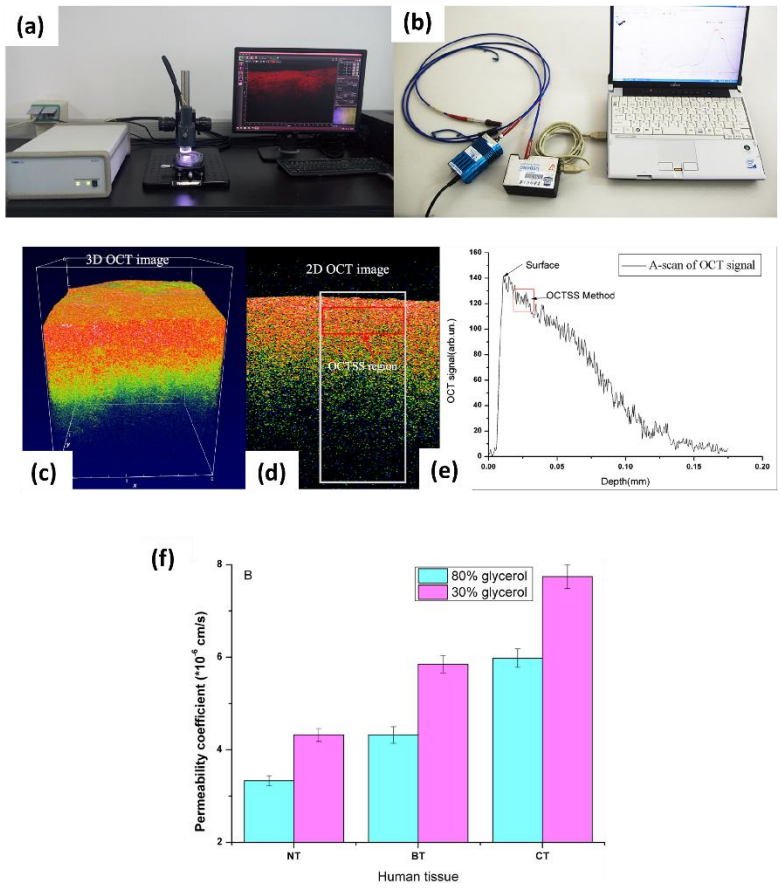

Figure 12. Images of a) OCT system b) Optical fiber spectrometer c) A typical 3D OCT image d) General 2D OCT image e) An average A-scans of OCT f) Permeability coefficients of 30% (pink) and 80% (blue) glycerol solution with EP in human normal gastric tissue (NT), benign gastric tissue (BT) and cancerous gastric tissue (CT). *Used with permission of IOP Publishing, Ltd, from Caiyun Li et al 2018 Laser Phys.* ***28*** *[205], Copyright 2018, permission conveyed through Copyright Clearance Center, Inc*

Li et al. conducted a captivating study that delved into the examination of gastric tissues from 12 patients in-vitro using both OCT and diffuse reflectance images. [205] Their spectral domain OCT system enables 2D and 3D imaging with a depth of about 7 mm and a line rate of 76 kHz. To acquire diffuse reflectance spectra, a tungsten halogen light source and a fiber optic probe were employed, measuring tissues in a quartz cuvette positioned 2 mm away from the probe. The overall set-up can be seen in **Figure 12**a, b. The study used glycerol at different concentrations (30% and 80%) as an optical clearing agent via electroporation, aiming to reduce optical scattering in samples. The permeability coefficient of glycerol within gastric tissue was calculated via OCT signal slope, through analyzing the slope change in OCT signal intensity caused by solution diffusion, illustrated in Figure 12c-e. From Figure 12f, permeability coefficients of glycerol with electroporation were larger than without electroporation. In 80% glycerol with electroporation, a 12%, 17%, and 20% increase was observed for normal, benign,

and cancerous gastric tissues respectively. At 30% glycerol with electroporation, coefficients increased by 18%, 22%, and 26% in normal, benign, and cancerous tissues. These findings indicate that electroporation significantly enhances glycerol permeability, improving imaging depth in gastric tissues. Using diffuse reflectance spectra, a consistent trend of cancerous > benign > normal tissues was observed for both 80% and 30% glycerol (with and without electroporation). A strong linear correlation ($R2 = 0.9745$) between permeability coefficient and diffuse reflectance reduction was identified. Thus, the findings indicated that OCT and diffuse reflectance spectra in combination with glycerol and electroporation could be used as a powerful tool for early diagnosis and monitoring of GC through the quantitative analysis of permeability coefficients and reflectance spectra. Despite this, it emphasizes the need to consider limitations and alternative explanations for correlations. Further exploration using ex-vivo experiments and drawing causal relationships for thorough result validation should be exercised with caution. Additionally, it is noteworthy that OCT can be significantly advanced alongside endoscopy for more effective in-vivo studies.

OCT shows promise in diagnosing GC through structural imaging, yet it has not been widely adopted in clinical practice. This limited adoption is due to technical challenges, difficulties in interpreting images and a lack of proven stratification and prediction capabilities. [206] Through incorporation of ML and deep learning approaches, along with extensive studies using OCT for GC diagnosis, accuracy and robustness of this technique could be significantly improved, paving way for its clinical acceptance.

2.2.7. Polarization Optical Spectroscopy (POS)

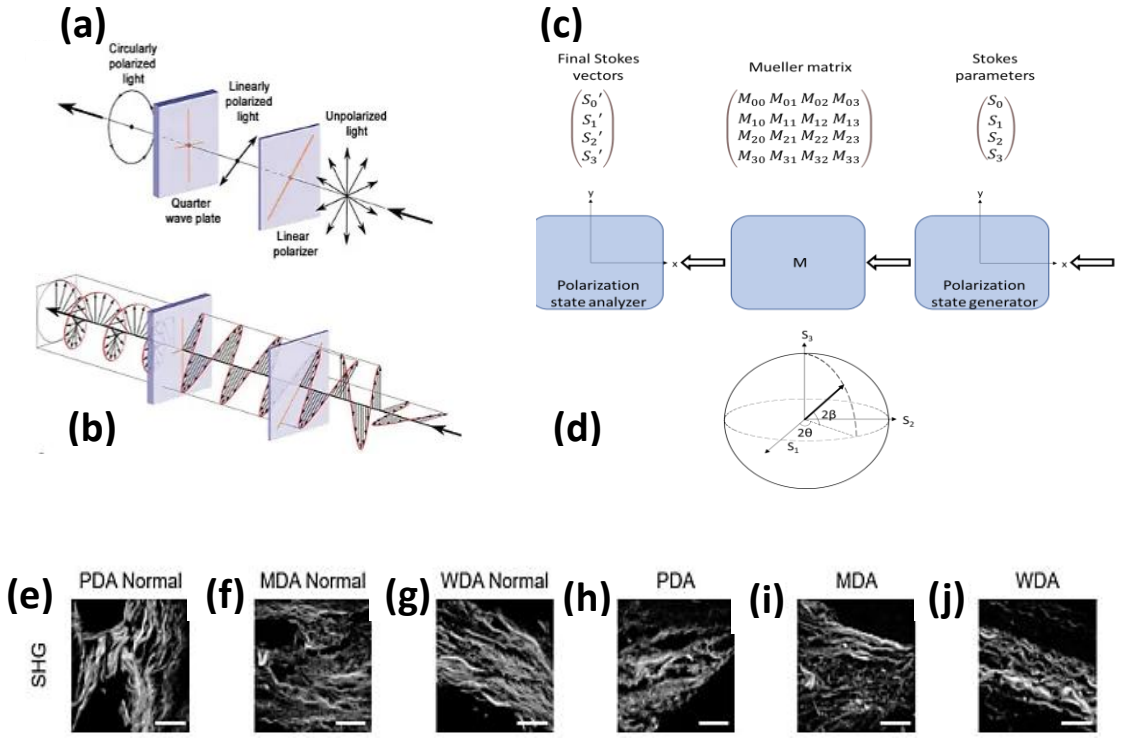

Figure 13 Diagrammatic representations of a) linearly and b) circularly polarized light; *Reproduced with permission under the terms of the CC BY 4.0 license [207] Copyright 2018, The Authors, Published by Oxford University Press;* c) illustration of the polarization state generator and analyzer for Mueller matrix probing; d) The Poincaré sphere is presented as a visualization tool for mapping polarization states. The azimuthal angle, denoted as 2θ, and ellipticity, denoted as 2β, are indicated. Additionally, the Stokes parameters (S1, S2, and S3) are represented as Cartesian coordinates. e-j) Polarization-in, polarization-out (PIPO) second harmonic generation microscope images of e) poorly differentiated adenocarcinoma (PDA), f) moderately differentiated adenocarcinoma (MDA), and g) well-differentiated adenocarcinoma (WDA) in normal gastric tissue from GC patients; and corresponding malignant tissues of h) PDA, i) MDA, and j) WDA. *Reproduced with permission [208] Copyright 2023, Optica Publishing Group under the terms of the OSA open access publishing Agreement.*

POS technologies have emerged as a cutting-edge tool in the realm of medical diagnostics, offering profound insights into the detection of GC. Morphological changes that occur when healthy tissues develop into cancer, such as increased nuclei density, altered cell distribution, and the enlargement of both cell size and nuclei, all of which can be observed in the presence of carcinogenicity, manifest as permanent alterations in tissue polarization properties like diattenuation, depolarization, and retardance. [209] These polarization changes serve as vital indicators of pathological transformations. By exploiting these distinct polarization properties, POS can be employed to observe and characterize these critical changes, providing a scientific basis for the early identification and diagnosis of GC. Polarimetry imaging provides the advantage of high sensitivity to small changes in cellular structures and good signal strength when compared to other optical technologies like fluorescence imaging. POS not only offers fast data acquisition but also characterization of tissue structural changes. However, it is important to note that polarimetry techniques are still in the process of maturation in clinical settings

for GC detection. Nevertheless, they are steadily gaining traction as promising tools for early identification and diagnosis.

The Stokes-Mueller formalism framework is fundamental to obtaining polarization properties. The polarization of light interacting with any optical system can be described by the real-valued 4×4 Mueller and the 4×1 Stokes matrices in the following equation:

$$\begin{pmatrix} S_0' \\ S_1' \\ S_2' \\ S_3' \end{pmatrix} = \begin{pmatrix} M_{00} & M_{01} & M_{02} & M_{03} \\ M_{10} & M_{11} & M_{12} & M_{13} \\ M_{20} & M_{21} & M_{22} & M_{23} \\ M_{30} & M_{31} & M_{32} & M_{33} \end{pmatrix} \begin{pmatrix} S_0 \\ S_1 \\ S_2 \\ S_3 \end{pmatrix} \quad (1)$$

The Stokes vectors (*S*) are transformed by the Mueller matrix into the final Stokes vectors *S'* upon interaction with sample. The Mueller matrix describes the various polarization states, giving the sample's polarimetric properties, even for non-depolarizing samples. Sample's polarimetric response can be obtained by decomposing the Mueller matrix into key polarimetric properties like diattenuation, retardance, and depolarization, despite the complexity of light-matter interactions. Diattenuation indicates changes in output intensity when modifying the constant input probing beam's polarization. Retardance values can be obtained from the phase shifts through birefringent mediums, whereas the depolarization parameter indicates the reduction in the degree of polarization of an incident beam when it interacts with the samples. **Figure 13**a-d illustrates the physics behind polarization optics technology.

Initial work by Qiu et al. in 2010 developed an endoscopic polarized scanning spectroscopy (EPSS) system for the rapid detection of dysplasia in Barrett's esophagus using optical scanning and multispectral imaging of the esophageal surface. [81] However, its applicability to larger and more complex regions, such as the stomach, remains unproven due to anatomical differences and limited clinical trials. This highlights the need for further research and technological refinement before it can be considered for clinical use, particularly in GC detection.

In 2014, Wang et al. conducted an ex-vivo study to investigate the effects of imaging wavelengths and the roles of circular and linear polarization properties in discriminating between normal and malignant gastric tissues. [210] Polarized visible light of wavelengths in the range of 470 to 632 nm were used to illuminate 46 malignant gastric tissue samples obtained from 40 patients. All images were taken with a commercial microscope with additional bandpass filters mounted. Tissue polarization parameters were derived from the Mueller matrix decomposition, revealing significant differences in parameters such as circular polarization, linear retardance, retardance, depolarization, and circular depolarization between healthy and GC samples. Furthermore, the wavelength of polarized light did not significantly impact tissue classification. These findings serve as a valuable foundation for developing a portable polarimetry

imaging system for in-vivo examination of gastric tissues, emphasizing the importance of linear and circular polarization parameters and wavelength selection in ongoing research for early GC diagnosis.

Tuniyazi et al. have advanced their earlier work by developing a novel fiber-based snapshot polarized light scattering spectroscopy (PLSS) endoscopic system for early GC detection . [211] This system employs a simplified dual-fiber design with a fixed multiorder retarder and linear polarizer, enabling spectral encoding of backscattered light along a single optical path. Compared to conventional PLSS setups that use multiple fibers and rotating polarizers, this compact design enhances mechanical stability, eliminates image misregistration, and increases signal fidelity by ensuring spatial overlap of illumination and collection areas. Notably, the authors introduced the weight of single scattered light (WSSL) as a novel diagnostic parameter, providing a fast, non-iterative means to differentiate normal from cancerous tissue. The system demonstrated high diagnostic accuracy (96%) in distinguishing ex vivo human GC tissues from healthy samples, validating both nuclear size inversion and WSSL-based detection approaches. This simplified, portable PLSS endoscope holds significant promise for clinical translation, especially for real-time, label-free, and cost-effective GC screening.

The most significant POS differences between cancerous and healthy gastric tissues were observed in the long wavelength visible light region (> 600 nm) as reported by Ilyov et al. [212] They explored different polarimetric parameters such as degree of polarization, ellipticity and azimuth angles, and Stokes vector elements using a standard polarimeter in reflectance mode with wavelengths in the range of (400 – 700 nm). Ex-vivo experiments measured using the polarimeter were validated against histological analyses. A clear difference between the healthy and cancerous regions for parameters such as azimuth and ellipticity angles, and Stokes parameters was observed. Higher ellipticity angle and polarization degree, along with a lower azimuth angle, were observed in malignant tissues. Stokes parameters S1 and S3 exhibited higher values in tumors. Error! Reference source not found. provides a summary of the polarimetric parameters that demonstrated significant differences between malignant and healthy gastric tissues. Notably, these parameters did not prove effective in distinguishing healthy tissues from benign tumors. Nevertheless, their work contributes to early GC detection research, as it was successful in detecting subtle changes in polarimetric values.

Table 1. Summary of polarization parameters that showed significant differences ($p < 0.05$) between healthy and malignant tissues. [212]

	Healthy Tissues	**Malignant Tissues**
Azimuth angle (θ°)	↑θ°	↓θ°
Degree of polarization (DOP)	↓ DOP	↑ DOP
Angle of ellipticity (ε°)	↓ε°	↑ε°
Stokes Parameter (S1)	↓ S1	↑ S1
Stokes Parameter (S2)	↑ S2	↓ S2
Stokes Parameter (S3)	↓ S3	↑ S3

Mueller microscopy is gaining popularity for its use in GC detection. Recently, Kim et al. developed a customized Mueller microscope in their attempt to generate quantitative optical metrics for characterizing the progression from healthy to cancerous gastric tissues by studying the inflammation profiles. [213] Unstained human gastric tissues with various pathological staging were used in their study. A polynomial regression model was developed to generate predicted images based on polarization parameters such as retardance, transmitted intensity, depolarization, and dichroism. The supervised ML regression model was trained on healthy, chronic gastritis and GC tissues. The main aim of their study was to develop a more streamlined and fast method to diagnose GC and other gastric conditions without the need for histopathological staining. Their results proved to be effective in screening for GC even for thick biopsy tissues, bypassing the time-consuming tissue section preparation. This revolutionary work not only reduced the time taken for diagnosis, but also the costs required.

Alterations in the collagen ultrastructure of GC and normal healthy gastric tissues can be discerned using polarization-resolved SHG (PSHG) microscopy. Jeon et al. observed statistically significant differences in the polarization parameters between healthy and GC tissues. [214] Their work not only able to distinguish between malignancy and healthy, but also distinguish the cancer staging. Significant changes in parameters like the cylindrical parameter (ρ), which is correlated to the collagen helical tilt of SHG emitters, *S*, and the triagonal parameter, which indicates the balance between the trigonal and cylindrical symmetries of the collagen, as well as the parameter κ, indicating the chirality of the collagen fibers, were observed. Figure 13e-j represents images depicting various types of GC differentiation acquired through the PSHG microscopy system. These changes reflect substantial alterations in collagen morphology at various stages of carcinogenicity. Their study also demonstrated that the PSHG parameter $|S|$ serves as the most reliable indicator for diagnosing GC and accurately determining staging status. This recent study represents progress toward clinical automated pathology, offering a faster alternative to traditional histopathological diagnosis methods, which can take days or even weeks to provide a definitive diagnosis.

POS technologies have shown great promise in early identification and diagnosis of GC. By utilizing distinct polarization properties, polarimetry techniques enable the observation and characterization of critical changes in tissue structure, offering high sensitivity and signal strength. Advancements in polarization optical methods highlight the increasing significance of these technologies in medical diagnostics. However, further refinement is necessary for their clinical application in detecting GC.

2.2.8. Other Techniques

Other optical techniques that have been explored for medical diagnostics of GC with various advantages including reduced to non-invasiveness, earlier detection and streamlined workflow are discussed in this section. HSI, THz imaging and SPR spectroscopy are some of the optical techniques that have shown great potential.

Hyperspectral Imaging (HSI)

HSI performs a combination of imaging and spectroscopic functions, providing spatial information as well as spectral information which is capable of revealing biological information. [215] A section of the sample is illuminated, and the dispersion is recorded by 2D detector arrays, providing spectral information. This is repeated for several sections across the sample, creating a dataset that is commonly referred to as a hyperspectral cube with spatial information in the *x* and *y* dimensions and spectral information in the *z* dimension. Variations of the setup have been developed to suit specific applications.

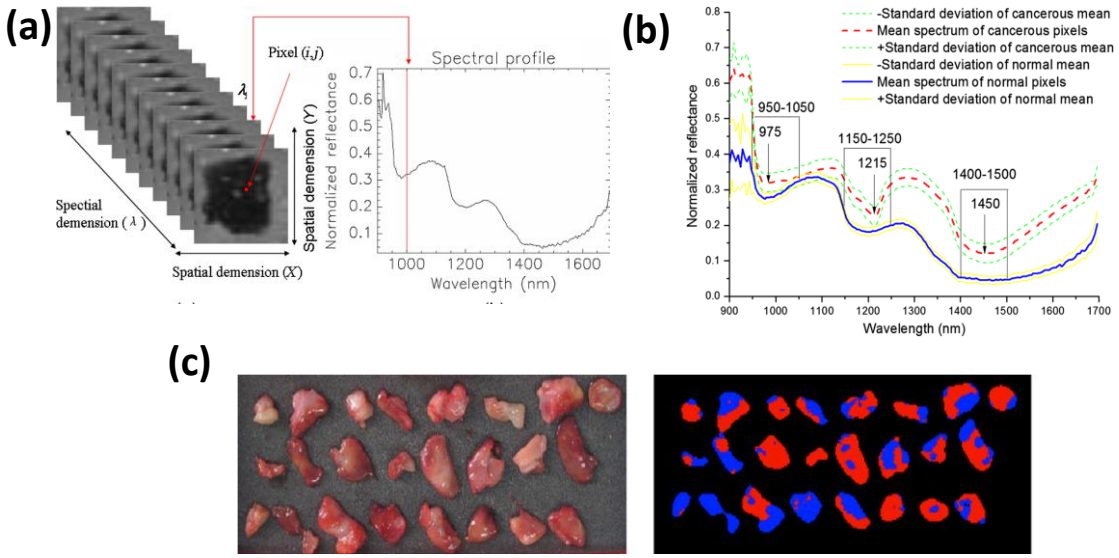

Figure 14. a) HSI data known as a hyperspectral cube consists of spatial and spectral dimension where the reflectance of a wavelength range is measured from a 2D surface. b) Standard deviation and mean of spectra from cancerous and normal gastric tissue samples are overlayed to identify difference in spectral features as annotated in the spectrum. c) Red, Blue, Green (RGB) image of gastric tissue samples and the corresponding (left) image with blue and red colored regions classified as normal and cancerous respectively based on SAM classification using HSI data (right). *Reproduced with permission under the terms of*

Findings from a study by Liu et al. were able to correlate changes in hyperspectral cube data with carcinogenesis in a large sample size. [216] They used a commercial HSI system (Hyperspec NIR XS-100, Headwall Photonics) with a spectral range of 900-1700 nm and spatial resolution of 0.8 mm/pixel. An overview of the study can be seen in **Figure 14**a. Samples of resected gastric mucosal tumors were obtained from 29 patients and hyperspectral cube data were acquired by the HSI setup. Analysis of the hyperspectral data showed that cancerous samples have a higher reflectance than normal samples, depicted in Figure 14b. This has been attributed to the difference in chemical structure and composition, specifically related to overtones and combinations of fundamental vibrations of C-H, N-H, O-H and S-H functional groups. Using PCA, the wavelengths 975, 1075, 1215, 1275, 1390, and 1450 nm were found to distinguish normal and cancerous tissue. The dataset was then processed and classified using PCA and spectral angle mapper (SAM) to extract characteristic spectral features for cancer and normal tissue differentiation, whereby conventional and classification images are depicted in Figure 14c. Additionally, the classification of hyperspectral data by SAM was able to identify regions as normal and cancer with 90% accuracy. To further improve this technology, the wavelengths with the characteristic spectral features for normal and cancer sample classification can be identified and data acquisition could be set to these wavelengths, reducing lengthy duration typically required for HSI.

Instead of examining the NIR region, Li et al. analyzed the hyperspectral data in the visible range (400-720 nm) using an in-house designed fluorescence HSI setup consisting of UV xenon light source and a CMOS detector. [194] Adjacent samples were collected from each of the 120 patients, where one sample was used for HSI, 116 hyperspectral data were acquired while the other was used for histopathology to classify non-precancerous (normal and non-atrophic gastritis), precancerous (atrophic gastritis and IM) and GC. Fluorescence intensity of IM and GC was similar in the HSI images. At 496 nm the intensity was weaker than precancerous and cancerous gastric tissue indicating metabolic abnormality of pyroxidal phosphate “Schiff” base. Also, in the 546 and 670 nm regions, the intensity was stronger in normal and atrophic gastritis tissue than IM and GC indicating abnormal phospholipid metabolism during carcinogenesis. The analysis of second derivative hyperspectral images, in the region of 466 nm and 546 nm related to NADPH and phospholipid, displayed that both intensities were lower in GC than in non-precancerous and precancerous lesions. An accuracy of 96.5% was achieved in tissue classification based on the hyperspectral data using CNN. This study was able to not only indicate the potential of HSI to accurately identify GC from normal tissue, but also discern differences in early stages of GC. By exploring different wavelength ranges, components that are significant to GC differentiation can be identified to develop a robust HSI method for GC detection, even before tissues become malignant.

Terahertz (THz) Imaging

THz imaging is another imaging modality that has been used in medical diagnostics. THz imaging exploits non-invasive spectral fingerprinting, relying on distinctive THz absorption and reflection patterns for precise tissue analysis. [217] In the setup, a THz laser source transmits pulses to a sample and a detector operating in the THz range collects the resultant signal, producing a THz image. Analysis of acquired THz images can be used to assess a sample's hydration levels and identify specific molecules present. Different types of THz imaging have been explored, a few of which with applications in GC diagnosis are discussed in this section.

THz imaging generates detailed images by distinguishing tissue regions based on water content, molecular composition, density variations, and structural details, providing comprehensive insights into biological samples. In the THz imaging setup described by Shi et al., a THz quantum cascade laser was used to emit a pulsatile signal of 3 THz with a 2D stepper to scan the sample and a CMOS detector. [42] Resected samples from 5 GC patients were assessed in this study. To account for sample-to-sample variation, 9 random points were imaged on each sampled tissue layer and the relative transmittance of each layer was calculated with respect to another layer. The images then showed that there was a significant difference in the relative transmittance of the mucosa and submucosal layers between normal and cancerous samples. It also showed that the transmittance of the submucosa is significantly different from the mucosa and muscular layers in normal samples while the transmittance of mucosa and submucosa in cancerous samples was similar.

THz time domain spectroscopy (THz-TDS) is a variation of THz imaging where specific molecules and deep structural changes are observed, instead of relative transmittance. Ji et al. used a conventional THz-TDS setup in reflection mode, where THz pulses are transmitted from an airtight box to the sample through a quartz window (**Figure 15**a). [218] GC lesion samples from 8 patients, 7 adenocarcinoma and 1 signet ring cell carcinoma were studied here. The examination of THz images in Figure 15b reveals reduced reflection intensity in the normal tissues near the tumor margin in comparison to the cancerous tissue. This difference is attributed to the lower refractive indices and absorption coefficients, underscoring the potential of THz-TDS for distinguishing between normal and cancer tissues. Additionally, the analysis indicates that THz images of adenocarcinoma samples exhibit clear differentiation, while the signet cell ring sample does not, suggesting potential sensitivity of THz-TDS to different cancer histopathology. Parts of the adjacent normal tissue in the resected samples exhibit

higher reflection intensity, likely originating from saline injected during resection, as depicted in Figure 15c.

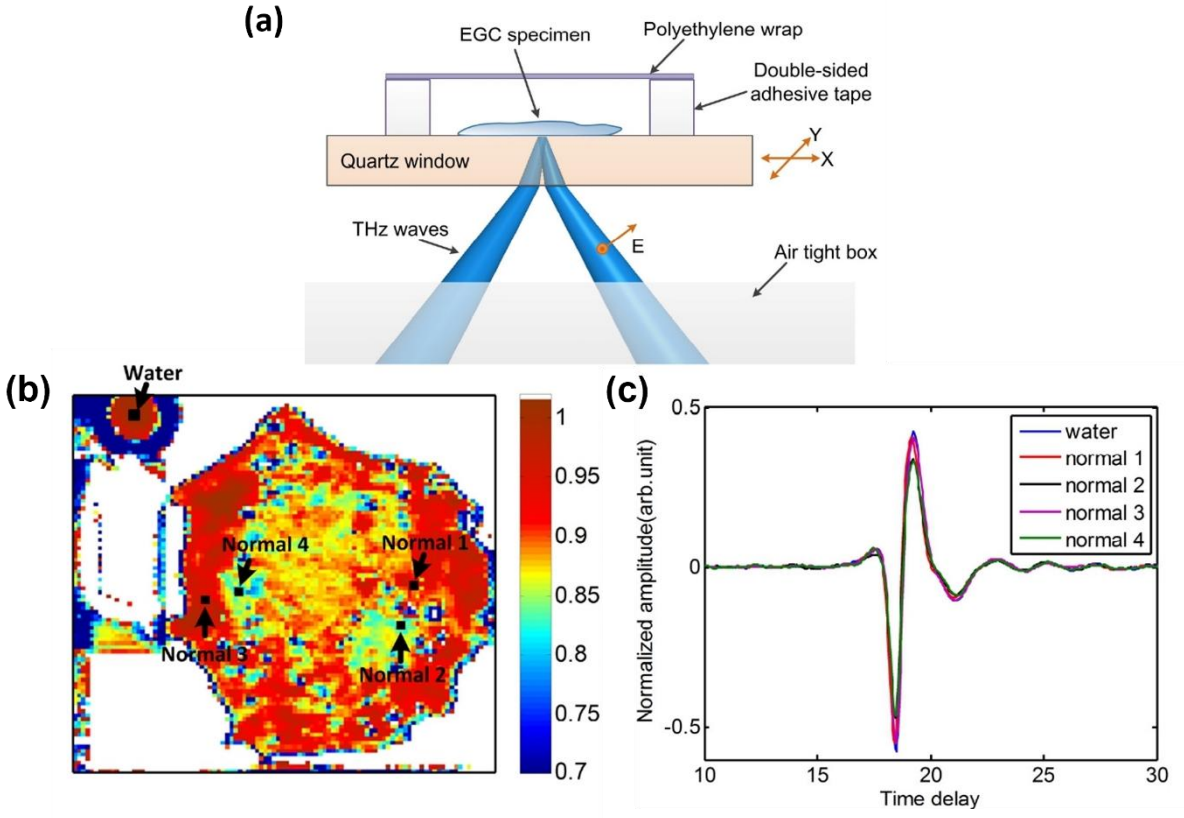

Figure 15. a) Terahertz time domain spectroscopy (THz-TDS) setup used in reflection mode, THz waves interacting with GC tissue samples through a quartz window. B) THz image acquired from a sample with 'Normal' and 'Water' regions marked out and c) their respective time domain spectra of the respective regions overlayed for comparison. *Reproduced with permission.* [218] *Copyright 2015, Optical Society of America.*

This limitation was also found in another study by Grigorev et al., where a similar THz-TDS setup was used. [219] Samples of GC lesions from 4 patients were analyzed and from the acquired THz images, it was found that the reflective index and absorption coefficient of cancer samples were generally higher than normal mucosa and serosa layers. This could be due to high cell density, cellular metabolic changes, abnormal protein density alterations and increased vasculature in cancerous tissue and is mainly attributed to higher water content in cancerous than in normal tissues. One of the distinctive features of THz imaging lies in its sensitivity to the phase of polar compounds. THz radiation is significantly absorbed in areas with high water content, resulting in a distinctive response. [217] Therefore, additional studies are needed to precisely define metrics that differentiate cancerous regions, including those injected with saline during resection procedures, from benign diseased areas. In contrast to Ji et al., Grigorev et al. could not differentiate between moderate and poorly differentiated adenocarcinoma samples. Given the cellular variations among GC types, a comprehensive study is necessary to identify distinct GC types using THz-TDS and explore potential differentiation.

In a multi-modal approach, Grigorev et al. used both THz-TDS and IR spectroscopy to analyze gastric tissue samples obtained from 4 GC patients. [219] In this study, the THz-TDS setup used in a previous study was replicated and similar conclusions were drawn, namely cancer cells were distinguishable due to increased water content, high cell density and increased vasculature. Samples from 2 of the patients were then selected for FTIR spectroscopy, one moderately differentiated adenocarcinoma and the other poorly differentiated adenocarcinoma. From the FTIR spectrum, changes in the peaks at 1650 cm^{-1} and 1550 cm^{-1} were observed which can be correlated to protein groups Amide 1 and Amide 2 respectively. The spectra were then analyzed using PCA which showed a clear separation between spectra obtained from cancer and normal tissues for both samples. Therefore, the combination of THz-TDS and IR spectroscopy can differentiate cancer tissues from normal. By performing FTIR spectroscopy on the same sample, the spectra can be analyzed for the presence of GC biomarkers, reducing the risk of a false positive.

Photoacoustic Imaging (PAI)

PAI utilizes the differential intrinsic optical absorption of chromophores in biological tissues. Chromophores like hemoglobin, lipids, and water have their own unique absorption spectra when subjected to nano-second pulse laser. The absorption of the laser by the chromophores generates heat that causes a temperature rise. Acoustic waves are generated through thermoelastic expansion and are detected by the transducers. Since sound scatters approximately 1000 times less than light, these acoustic signals can propagate further in biological samples with minimal attenuation. [220] This property of PAI makes it a promising high-resolution imaging or analytical tool for clinical applications, especially when compared to pure optical methods that suffer from significant optical scattering.

PAI is a relatively new clinical imaging technique, especially in the context of GC detection. Most research on PAI for GC is at the preclinical stage, primarily employing animal models. In the past decade, only one study has reported PAI for GC detection in human samples. Wu et al.'s recent work represents a notable advancement, transitioning from GC preclinical models to in-vitro testing. [221] They developed a dual-mode imaging system that utilizes both ultrasonic and photoacoustic technologies integrated within a gastroscopy system for real-time GC detection. 4 resected gastric tumor samples, 2 poorly differentiated and 2 moderately differentiated were used here. Each sample was divided into 2 parts, with 1 being used for histological analysis, and 1 for PAI. The sophisticated imaging system employed in this study comprises a 532 nm pulsed laser source, which was directed to an optical parametric oscillator to generate a wavelength of 808 nm. This laser output was precisely focused onto a customized multimode optical fiber, seamlessly integrated with an endoscope. Subsequently, the laser beam irradiated the gastric tissue directly, and the resulting acoustic signals were meticulously captured and recorded using a 2D-array transducer. The results of this experiment demonstrated that both submucosal and superficial GCs can be diagnosed with a detectable depth of 6.33 mm by analyzing angiogenesis morphology, achieving a resolution of 2.23 mm laterally and 0.17

mm vertically. The capability of the dual-mode imaging system, together with endoscopy developed here, sets a precedent for in-vivo clinical detection of GC, making it a promising diagnostic tool for early and rapid detection of GC.

Surface Plasmon Resonance (SPR) spectroscopy

SPR, also an optical modality used in medical applications works on the principle that when electrons on a metal surface are excited by an incident light, oscillation occurs, giving rise to plasmons, and depending on the refractive index of the material directly interfacing with the metal surface, the resonance angle changes. [222] By monitoring the changes in resonance angles, different materials are segregated. Various materials and shapes of metallic sensors have been developed for optimal performance.

Palladium platinum gold (PdPtAu) alloy spheres were designed by Su et al. with mesoporous surface to be used in conjunction with laser desorption/ionization mass spectrometry (LDI-MS). [223] In this study using PdPtAu-assisted LDI-MS, distinctive GC biomarkers were identified in liquid biopsy samples. The different trimetallic spheres synthesized were optimized to enhance signal strength and retain metabolites based on particle size, as confirmed through characterization studies including energy dispersive X-ray analysis, UV-vis spectroscopy, and size-exclusion chromatography and PdPtAu-3 alloy spheres had the best intended performance. 292 plasma samples collected from GC patients were analyzed by PdPtAu-3-assisted LDI-MS and verified by gastroscopic and histological assessments. Using the gold standard, 149 samples were categorized as GC (46, 42, 50, 11 for stage I, II, III, IV respectively), and the remaining 143 samples as normal which were used as controls. The spectra obtained in this study identified 12 spectral features forming a metabolic FP that effectively distinguishes GC from normal samples. These features correlated with 6 specific metabolites (dihydrothymine, 5-hydroxytryptophol, glyceraldehyde 3-phosphate, aconitic acid, 6-succinoaminopurine, cyclic N-acetylserotonin glucuronide). They achieved an impressive 92.0% sensitivity and specificity. Notably, when compared to other methods (organic matrix-assisted LDI-MS, liquid chromatography, and nuclear magnetic resonance), PdPtAu-3-assisted LDI-MS demonstrated the capability to diagnose GC without sample preparation and with larger sample volumes.

Other than metallic spheres, Zhang et al. explored multi walled nanotubes (MWNTs). [224] In this study, gold-silver (Au-Ag) alloy nanocomposites synthesized MWNTs, coated on glass carbon electrodes for the adsorption of VOCs as GC biomarkers. VOCs from normal GES-1 gastric mucosa and GC MGC-803 cell lines were analyzed using GC-MS, revealing changes in 8 VOCs. Three VOCs (formic acid propyl ester, 1,4-butanediol, dodecane,2,6,11-trimethyl) were exclusive to normal cells, two (3-octanone, butanone) to cancer cells, and three (4-Isopropoxybutanol, nonanol, 1-butanol,4-butoxy) showed higher levels in normal cells. Using MWNTs as an electrochemical biosensor, the exposure to cancer cell VOCs showed detection ranges of 0-0.0025% and 0-0.055% for 3-octanone and butanone, with detection limits of 0.3 and 0.5 ppb, respectively. Although this study identified VOCs specific to cancer cells, studies using samples from patients will be required to further assess its feasibility.

In a unique SPR biosensor design, Li et al. designed a surface plasmon coupled electrochemical luminescence (SPC-ECL) biosensor where electrodes were coated with bismuth nano-nest and MXene derivative quantum dots (Ti3CN QDs). [225] Characterization studies included transmission emission microscopy, IR spectroscopy, and UV-vis spectroscopy for the QDs, and surface electron microscopy for electrodeposited bismuth nano-nest. Ascitic fluid, which accumulates in the abdominal cavity of different GC patients, was collected to extract miRNA-421 samples. They were then further quantified using SPC-ECL with a detection range of 1 fm to 10 nm and a detection limit of 0.3 fm. Compared to other ECL sensors, the reported SPC-ECL exhibited a broader detection range and lower detection limit.

3. Conclusion

The landscape of GC diagnosis has seen significant advancements, bridging both basic and clinical research towards a patient centric clinical translation in ex-vivo lesion detection, targeted biopsies, and non-invasive biomarker identification. Despite these strides, significant gaps remain between sophisticated current endoscopic technology and disease biomarker identification, highlighting the need for integration to tailor modalities for reliable detection. This review explored a spectrum of biophotonics techniques, each offering unique merits and clinical potential for GC diagnosis. In this section, a summary and comparison of these techniques for both in-vivo and ex-vivo/ in-vitro detection is presented.

3.1 In-Vivo Detection

Narrow Band Imaging, NBI: NBI is a transformative tool in precision medicine for GC diagnostics, utilizing specific narrow bands of light for examining mucosal vascular patterns crucial for early lesion detection. Studies by Fujiwara, Kojima, and Kanesaka [26,59,226], as well as Horiuchi, Tang, and Wang, emphasize its superior diagnostic capabilities, especially with AI integration [14,34,36]. NBI is well-suited for early diagnosis and is currently one of the most deployable technologies in clinical practice. Improving imaging resolution and integrating AI for enhanced lesion identification could be the next step of advancements.

Confocal Laser Endomicroscopy, CLE: CLE enhances the yield of cancer cells in undifferentiated GC compared to traditional endoscopy and shows potential as a preliminary diagnostic tool before biopsy to ensure adequate tissue sampling. CLE is advancing towards routine clinical use and is promising for early-stage diagnosis. It has tremendous potential to be incorporated with the RS system for comprehensive GC diagnosis.

Raman Spectroscopy, RS: RS shows great promise for GC detection, capable of differentiating between lesioned and non-lesioned tissues using fingerprint biochemical spectra. Despite technical challenges in standardization and in-vivo validation, RS is advancing towards clinical application. [87,97,101] It holds significant potential for early diagnosis due to its molecular fingerprinting capabilities, but further in-vivo validation is required. Further, integration with high-accuracy prediction tools through machine learning approaches could potentially revolutionize this technique. The inherent limitation in the sensitivity of RS in detecting subtle biochemical changes at early stages of cancer growth needs to be addressed to translate this technology into a reliable and clinically viable diagnostic tool for GC detection.

Fluorescence Spectroscopy and Imaging: This method is effective for both ex-vivo (or in-vitro) and in-vivo detection of GC. Studies utilizing multiphoton microscopy (MPM) and advanced machine learning models have achieved high accuracy in distinguishing between non-atrophic gastritis,

premalignant lesions, and GC. [188,190,191] Challenges remain in standardization and signal interpretation when autofluorescence from multiple tissue components arises. Fiber-based confocal autofluorescence measurement system could offer identification of markers without the interference from undesired chromophores. This will help in differentiating from common endogenous auto-fluorescence agents that often camouflage the signal. The fluorescence measurement approach offers a cost effective and easy to implement technique and shows promise for early diagnosis and is advancing towards clinical deployment.

The diverse optical techniques explored in this review present unique advantages and challenges. The focus on in-vivo studies underscores the practical applications of these technologies, highlighting their pivotal role in improving diagnostic accuracy and expanding clinicians' toolkits. However, integrating these technologies into routine clinical practice requires overcoming numerous technical challenges, conducting comprehensive validation studies, and fostering interdisciplinary collaboration. The combination of biophotonics technologies offers a promising outlook for early GC detection and personalized treatment, with NBI, RS, Fluorescence Spectroscopy, and CLE emerging as highly promising clinical modalities.

3.2 In-Vitro/Ex-Vivo Detection

Surface-Enhanced Raman Spectroscopy, SERS: SERS enhances Raman signals using plasmonic metal nanoparticles, proving effective in detecting GC biomarkers in biofluids. Integration with microfluidic chips and lab-on-a-chip systems shows promise for clinical application. While SERS is promising for early diagnosis, it is currently confined to ex-vivo and in-vitro studies and requires further clinical validation. [90, 94] VEGF, CEA, mRNA, miR-106a, and PDGF-B are biomarkers detectable using SERS, which provides high sensitivity and specificity in identifying molecular changes linked to GC progression. In the context of SERS-based GC detection, a focused initiative should be aimed at creating stable substrates and targeted colloidal nanoparticles that offer high sensitivity. Creating SERS substrates with substantial Raman signal enhancement and minimal spatial signal variance (signal reproducibility) remains a significant challenge. Progress in establishing such cost-effective, yet dependable protocols for fabricating SERS substrates and exploring innovative nanomaterials for consistent signal enhancement should be thoroughly investigated.

Optical Coherence Tomography, OCT: It offers high-resolution, real-time imaging, surpassing traditional methods. Recent research, including quantitative parameters from SS-OCT images and deep learning approaches shows OCT's potential for high specificity and sensitivity in GC classification. Since OCT can be implemented in an endoscopic mode, it is well-suited for early diagnosis and is nearing clinical application, though further research is needed on developing customized OCT probe and improving measurement accuracy.

Diffuse Reflectance Spectroscopy, DRS: It is a valuable tool for ex-vivo/in-vitro, cost-effective cancer diagnosis, providing real-time insights into tissue composition and morphology. Studies by Gkouzionis and Nazarian highlight its potential for intraoperative use. [171,172] Unlike Raman, DRS is unable to give direct spectral biomarker information, and it requires spectral unmixing approaches. While DRS shows promise for early diagnosis, its clinical application is still in the developmental stage, requiring more extensive validation.

Fourier Transform Infrared Spectroscopy, FTIR: FTIR distinguishes healthy and cancerous gastric tissues, offering a non-invasive diagnostic tool. Studies like those by Akin Geyik and Li et al. demonstrate FTIR's potential, though further research is needed to enhance reliability and clinical utility. [154,159] FTIR is promising for early diagnosis, but it is still in the validation stage.

Polarization Optical Spectroscopy, POS: Advancements in POS offer a promising tool for early detection of GC. Techniques like PSHG microscopy provide valuable insights into collagen ultrastructure alterations and cancer staging, making them particularly useful for detecting subtle tissue changes indicative of early cancer. Although it is still in the early stages, combining polarization parameters with machine learning models could offer a rapid, non-invasive diagnostic method, improving early detection and treatment planning.

Other Techniques

HSI holds potential for distinguishing between normal and cancerous gastric tissues by capturing detailed spectral information across a wide range of wavelengths. This technology can identify subtle differences in tissue composition and structure, which are crucial for early diagnosis. Despite its promise, HSI remains in the early stages of clinical application and requires further validation through extensive clinical trials to confirm its efficacy and reliability. On the other hand, THz imaging shows great promise for non-invasive spectral fingerprinting and tissue differentiation, offering unique capabilities for detecting molecular and structural changes in tissues. However, THz imaging needs more research to address current limitations, such as resolution and depth of penetration, and to validate its effectiveness on a larger scale before it can be widely adopted in clinical settings. SPR is a promising technique for identifying GC biomarkers, particularly in liquid biopsies. It works by detecting changes in refractive index near the sensor surface, making it sensitive to molecular interactions. This technology is valuable for early cancer detection and monitoring in an in-vitro/ex-vivo setting. Challenges related to reproducibility in different metallic substrate designs highlight the need for optimization and standardization. Addressing these issues will enhance SPR's reliability and pave the way for its integration into routine clinical practice. For PAI, Wu et al. demonstrated the first proof of concept translation of the technique from preclinical models to in-vitro testing for GC detection. [221] Though this technique is in its infancy for GC detection, it has the great potential to be adopted for in-vivo studies in future as there are many reports of PAI imaging and spectroscopy integrated into fiber

optic probes. [227,228] The efficacy of fiber based PAI lies in its analytical abilities for vascular dynamics, including blood oxygenation saturation studies. Moreover, it shows potential for developing a multimodal spectroscopy system by integrating with OCT detection capabilities, which will augment well in detecting tissue morphological changes.

Table 2 summarizes and compares the pros and cons of each technology and the required technical advancements for early detection using in-vivo and in-vitro/ex-vivo methods.

Table 2. Table comparing the various biophotonics technologies for GC detection.

Technology	Category	Pros	Cons	Remarks	Potential improvement	Key disease differentiator
Narrow Band Imaging	In-vivo	Accuracy, enhanced mucosal pattern visualization, Potential for AI integration	Limited by imaging resolution	Highly relevant for early Detection and used in regular clinical practice	AI-integration, Improved system design, and potential adoption for multimodal detection	Enhances mucosal microvascular contrast using light absorbed by hemoglobin to detect vascular abnormalities.
Confocal Laser Endomicroscopy	In-vivo	Enhances cancer cell yield, real-time visualization	Limited generalizability due to signal variation and high cost, steep learning curve in data interpretation	Potential for early-stage detection, nearing routine clinical use	Simplify the instrumentation and operation, integrate for multi modal analysis	Abnormal cellular morphology, disrupted mucosal architecture, and distinct vascular patterns (tortuous and leaky vessels) indicative of GC.
Raman Spectroscopy	In-vivo/Ex-vivo	Unique molecular fingerprinting, high accuracy in prediction	Relative expensive system, challenges in standardization of measurement, poor signal-to-noise ratio in gastric cavity	Promising for early diagnosis, option for incorporating to multimodal system	Standardize procedures, improve signal collection efficiency in Raman probe, develop real time interpretation	Change in intensity at 1004 cm^{-1} (phenylalanine), 1335 cm^{-1}(nucleic acids), and 1655 cm^{-1} amide I from proteins) and other related peaks from amino acids/proteins for malignant tissues.
Diffuse Reflectance Spectroscopy	Ex-vivo	Simple, cost-effective real-time diagnostics	Limited spectral biomarker information,	Promising for early diagnosis in developmental stage	Improvement in sensitivity and specificity and potential	Alterations in changes in endogenous tissue absorbers and vascular profiles,

			needs spectral unmixing		integration to endoscopes	
Fluorescence Spectroscopy and Imaging	In-vivo and Ex-vivo	High accuracy, label-free imaging, cost effective real-time applications	Standardization challenges, signal interpretation in highly auto fluorescing medium	Promising for early diagnosis, advancing towards clinical deployment	Standardize protocols, enhance signal interpretation, integrate for multi modal detection for improving accuracy	Endogenous or exogenous (dyes, beads) fluorophores exhibiting difference fluorescence intensity for tumor cells and metastatic lymph nodes as compared to healthy regions.
Optical Coherence Tomography	Ex-vivo	High-resolution, real-time imaging, label free high specificity	Difficulties in image interpretation, minimal prediction capabilities	Advancing into in-vivo clinical application	Improve imaging speed and resolution, integrate with other modalities	Tissue morphological differentiation, where cancerous tissues exhibit heterogeneous textures and significant fragmentation, while normal tissues appear smooth and homogeneous.
Polarization Optical Spectroscopy	Ex-vivo	Rapid diagnosis, valuable insights into collagen ultrastructure	At very early stage of application, high cost due to its complex system design	Promising for early diagnosis and need more validation	Optimize parameters, robust system design and integrate into multimodal system	Morphological changes, such as increased nuclear density and enlarged cell sizes, which manifest as altered tissue polarization properties like diattenuation, depolarization, and retardance.
Surface-Enhanced Raman Spectroscopy	Ex-vivo	High sensitivity, multiplex detection, effective in detecting	Poor signal reproducibility,	Promising for early diagnosis, confined to ex-vivo studies,	Create highly reproducible substrates, standardize protocols	Elevated peak intensity are observed at 936 cm^{-1} (proteins), 1265 cm^{-1} 1445 cm^{-1} and 1745

		biomarkers in body fluids				cm^{-1} (lipids), 1335 cm^{-1} (nucleic acids), 1655 cm^{-1} (amide I from proteins), for malignant tissues.
Fourier Transform Infrared Spectroscopy	Ex-vivo	Non-destructive, distinguishes healthy and cancerous tissues using fingerprint spectra	Variation in spectral signatures due to biological variability, high background absorbance from complex samples	Promising for early diagnosis, pending validation	Improve spectral resolution, develop robust algorithms	Emergence of new band at 1210cm^{-1} in GC patients, variations in amide I (1600-1700cm^{-1}) and amide III bands (1285, 1265cm^{-1}). In red blood cells, GC patients exhibited higher peak-area ratios at A1653/A1543, A1543/A2958, A1106/A1166 and A1543/A1106.
Hyperspectral Imaging	Ex-vivo	Potential for distinguishing normal and cancerous tissues	Expensive system, at very early clinical application stage	Promising, but needs further validation both in hardware and software	System miniaturization, optimize imaging techniques, test in larger patient cohorts	Variation in intensity is observed in GC groups due to different structural and chemical composition, especially in the C-H, N-H, O-H, S-H functional groups and phospholipid groups.
Terahertz Imaging	Ex-vivo	Non-invasive spectral fingerprinting	Equipment cost, signal interference from water, data interpretation	Promising, but in early research stage	Improve imaging resolution, standardized protocols	Images are produced based on water content, molecular composition, density, and structural variations in the tissue regions. Refractive index

						and absorption coefficient changes were observed in tumor regions.
Surface Plasmon Resonance Spectroscopy	Ex-vivo	Label free, real-time detection, minimal sample preparation	Poor signal reproducibility, low sensitivity, non-specificity, and surface functionalizatio n challenges	Promising, but needs optimization	Improve substrate design, validate in clinical trials	Mainly used to enhance the signal with other spectroscopy techniques. Biopsy samples of tissues and abdominal fluid show spectral variations in cancerous and non-cancerous cases.
Photoacoustic Imaging	Ex-vivo	Structural and functional imaging, label free real-time imaging	High cost, susceptible to motion artifacts	Promising, however it is still in developmenta l stage for clinical applications	Integration with existing endoscopic and imaging systems, improvement on algorithms for real-time data analysis and artifact reduction	Malignant tissues exhibit stronger acoustic signals due to increased hemoglobin absorption from heightened vascularization, allowing differentiation based on optical absorption properties.

4. Future Perspectives

This review has discussed various optical technologies used for GC detection and diagnosis. GC detection depends on optical technologies that can help identify cancerous lesions or cells in gastric tissue, while diagnosis utilizes optical technologies to classify gastric tissue based on specific disease states. These capabilities have been found to be achievable both in-vivo (in real-time within patients) and ex-vivo (quickly at the bedside or in adjacent pathology labs). Both approaches are applicable in clinical settings, depending on the requirements. For instance, surgeons may prefer an in-vivo approach to assist in precisely removing a cancerous lesion without unnecessarily sacrificing healthy gastric tissue. Therefore, the selection of optical technology greatly depends on the specific clinical needs that need to be addressed.

The future of biophotonics in GC detection holds immense promise, leveraging various cutting-edge technologies like NBI, RS, fluorescence imaging, OCT, reflectance imaging etc., for in-vivo applications. One of the critical challenges in realizing a practically relevant clinical diagnosis of GC using biophotonics is the lack of sensitive yet inexpensive and portable optical components. Developing smaller, portable, and user-friendly devices is crucial. Compact instrumentation would allow for easier integration into clinical settings, enabling point-of-care diagnostics and improving patient accessibility. Developing miniaturized optical components using next generation flat optics components, an advancement from the conventional bulk optics components, with nanometer-micron sizes lenses and beam steering components will offer a unique advantage in system miniaturization while maintaining spectral resolution and sensitivity, especially for endoscopic configurations. [229] Flat optics components can be integrated easily into fiber probes by replacing conventional lens components and it will offer large field-of-view (FoV) while maintaining compactness and sensitivity. Further, advances in nanotechnology and microfabrication techniques could enable the development of miniature optical components essential for compact biophotonics systems. Emphasis on designing systems that operate on low power and are battery-powered would enhance their usability and will offer broader diagnostic capabilities in low resource settings.

Multi-modal detection by combining different biophotonics technologies to identify complementary subtle molecular and cellular changes associated with early-stage GC offer great promise. This could involve the integration of RS, fluorescence imaging, and OCT to detect biochemical and structural alterations in tissues, enabling more accurate diagnosis. This synergy allows for a more comprehensive analysis of tissue morphology, molecular composition, and biochemical alteration in tissues thereby minimizing false positives and negatives. Further, combining CLE or MPM with RS will enable real-time visualization of cellular and subcellular details in the gastric mucosa. Integrating these with spectroscopic techniques can guide targeted biopsies, improving the accuracy of tissue sampling. Functional imaging modalities, including PAI and DRS can effectively be combined to assess treatment efficacy and enable personalized treatment strategies based on real-time feedback.

Like the rest of medical technological advancements, the space of GC is riding the same AI wave. Referencing one of the world-renowned leaders in AI, Kai-Fu Lee, the world is transitioning from the age of discovery to implementation, and from the age of expertise to data. [230] Advancements in ML algorithms are essential for efficient and accurate analysis of biophotonics-generated data. AI can aid in pattern recognition, improving diagnostic accuracy, and aid in real-time decision-making. Developing robust quantitative analysis methods is crucial for translating raw optical data into clinically relevant information. Standardizing metrics and parameters for interpretation could enhance diagnostic consistency and reliability. This is evident in the reviewed studies, where various established ML methods have been used in interpreting the measured optical signals, with interpretation enabled by the pool of data researchers and clinicians have strived to collate (and correlate) over the years. Admittedly,

this pooling of data has happened in a pseudo-random manner thus far, with different countries, institutions, and individuals collating data in different ways, albeit still systematic and logical. Moreover, the multitude of different data types, arising from the variety of different techniques (such as the different optical technologies in the context of this review), renders this an even more problematic task. Although it will be infeasible to synchronize data collation across the globe, it is still practical to do so at the national or even regional level. Harmonizing the way data is collated is thus the next crucial step for GC detection and diagnosis to effectively ride the AI wave.

Cross-disciplinary research and collaboration among physicists, engineers, biologists, and clinicians is vital for driving innovation. Integrating expertise from diverse fields can accelerate the development and translation of biophotonics technologies into clinical practice for the detection and treatment monitoring of GC. In this regard for easier clinical adoption of technologies, researchers in the biophotonics field should work hand in hand with clinicians from the beginning of instrument development. Developed technologies should be deemed a "must-have" rather than a "nice-to-have," underlining their indispensable significance in various applications. Further, conducting extensive clinical trials and validation studies is crucial for establishing the efficacy, reliability, and safety of diagnostic tools for GC.

For any optical technology to have a meaningful clinical impact, widespread adoption is essential. This brings factors such as cost, usability, reliability, and robustness into focus, even though they may not always be prioritized during the early stages of research and development. While proving the technical capabilities of a novel optical technology is important, overlooking these practical considerations can undermine its long-term success. Developers must recognize that adoption is a critical element in the lifecycle of any technology. It is vital to understand and address the barriers that may hinder its use in real-world settings. A tailored approach that considers the diverse needs of various demographics will ensure technology delivers reliable and accessible results for all populations. Ultimately, successful adoption depends on how well these factors are integrated into the development process.

The future of biophotonics technologies for GC detection is highly promising, with ongoing research driving significant advancements in early detection and diagnostic accuracy. These innovations are expected to improve patient outcomes through more precise and timely interventions. Emerging biophotonics tools will likely become cost-effective and widely accessible, making their integration into clinical settings more feasible. Ultimately, these advancements hold the potential to revolutionize the diagnosis, management, and monitoring of GC, leading to substantial improvements in patient care.

Table 3: List of abbreviations in the review paper

1-dimensional convolutional neural network (1D-CNN)	Multi walled nanotubes (MWNT)
2-dimensional (2D)	Multiphoton microscopy (MPM)
2-dimensional infrared correlation spectroscopy (2D-COS)	Mxene derivative quantum dots (Ti3CN QDs)
4-mercaptobenzoic acid (4-MBA)	Narrow Band Imaging (NBI)
5-ALA (5-aminolevulinic acid)	Native fluorescence and stokes shift spectroscopy (s3) (NFL)
Advanced GC (AGC)	Near infrared (NIR)
Alpha-fetoprotein (AFP)	Negative predictive value (NPV)
Artificial intelligence (AI)	Nicotinamide adenine dinucleotide hydrate (NADH)
Attenuated total reflection-Fourier transform infrared (ATR-FTIR)	Nicotinamide adenine dinucleotide phosphate (NADPH)
Attenuated total reflection-Fourier transform mid-infrared (ATR-MIR)	Optical Coherence Tomography (OCT)
Area under curve (AUC)	Oxidative stress index (OSI)
Bismuth nano-nest (Bi NN)	Palladium platinum gold (PdPtAu)
Carbohydrate antigen (CA)	Partial least squares-discrimination analysis (PLS-DA)
Carcinoembryonic antigen (CEA)	Persistent luminescence nanoparticle (PLNP)
Characteristic ratio method (CRM)	Photodynamic diagnosis (PDD)
Charge-coupled device (CCD)	Photo-protoporphyrin (PPP)
Classification and Regression Tree (CART)	Photosensitizer (PS)
Clustered regularly interspaced short palindromic repeats (CRISPR)	Platelet-Derived Growth Factor-B (PDGF-B)
Computer-aided diagnosis (CAD)	Polarization-resolved second harmonic generation (PSHG)
Confocal laser endomicroscopy (CLE)	Polarization optical spectroscopy (POS)
Convolutional neural network (CNN)	Polarized light scattering spectroscopy (PLSS)
Degree of polarization (DOP)	Polymerase chain reaction (PCR)
Deoxyribonucleic acid (DNA)	Positive predictive value (PPV)
Diffuse reflectance spectroscopy (DRS)	Principal component analysis (PCA)
Digestive tract cancers (DTC)	Principal component analysis -Linear discriminant analysis (PCA-LDA)
Early Gastric cancer (EGC)	Probe-Based Confocal Laser Endomicroscopy (pCLE)
Enzyme linked immunosorbent assay (ELISA)	Protoporphyrin IX (PPIX)
Euclidean distance-based Raman spectroscopy (EDRS)	Quantitative real-time PCR (qRT-PCR)
Excitation emission matrices (EEM)	Raman spectroscopy (RS)
EXtreme gradient boosting (XGB)	Random forest (RF)
Field of view (FoV)	Receiver operating characteristics (ROC)
Fingerprint (FP)	Ribonucleic acid (RNA)
Fourier transform infrared spectroscopy (FTIR)	Red Blue Green (RGB)

Fourier transform near infrared spectroscopy (FT-NIR)	Spectral angle mapper (SAM)
Gastric cancer (GC)	Second harmonic generation (SHG)
Gold-silver alloy (Au-Ag)	Sentinel node navigation surgeries (SNNS)
Haematoxylin-eosin (H&E)	Small extracellular vesicles (sEVs)
Helicobacter pylori (H. Pylori)	Spectral and time-resolved MPM (STMPM)
Helium-Neon (He-Ne)	Spectral resolved MPM (SMPM)
Hemicyanine core (HCC)	Stimulated Raman scattering (SRS)
High wavenumber (HW)	Support vector machine (SVM)
High-grade intraepithelial neoplasia (HGIN)	Surface plasmon coupled electrochemical luminescence (SPC-ECL)
Hybridization chain reaction (HCR)	Surface Plasmon Resonance (SPR)
Hyperspectral Imaging (HSI)	Surface Enhanced Raman Spectroscopy (SERS)
Indocyanine green (ICG)	Swept source optical coherence tomography (SS-OCT)
Infrared (IR)	Terahertz (THz)
Interleukin 8 gene (IL-8)	Terahertz time domain spectroscopy (THz-TDS)
Intestinal metaplasia (IM)	Two-photon excited fluorescence (TPEF)
K-nearest neighbour (KNN)	U-shaped fully convolutional network (U-Net)
Laser desorption/ionization mass spectrometry (LDI-MS)	Ultraviolet (UV)
Limit of detection (LOD)	Vascular Endothelial Growth Factor (VEGF)
Linear discriminant analysis (LDA)	White light endoscopy (WLE)
Machine learning (ML)	Zinc selenide (ZnSe)
Magnifying narrow band imaging (M-NBI)	

Acknowledgements

This research was supported by the Agency for Science, Technology and Research (A*STAR), Singapore, 'Translational Biophotonics Innovation Platform' IAF-PP Grant No. H19H6a0025 and GAP-Funded Project No. I22D1AG016.

References

[1] T. I. A. for R. on Cancer (IARC), "Global Cancer Observatory," can be found under https://gco.iarc.fr/, **2024**.

[2] H. Sung, J. Ferlay, R. L. Siegel, M. Laversanne, I. Soerjomataram, A. Jemal, F. Bray, *CA: a cancer journal for clinicians* **2021**, *71*, 209.

[3] M. Ilic, I. Ilic, *World journal of gastroenterology* **2022**, *28*, 1187.

[4] E. Morgan, M. Arnold, M. C. Camargo, A. Gini, A. T. Kunzmann, T. Matsuda, F. Meheus, R. H. A. Verhoeven, J. Vignat, M. Laversanne, J. Ferlay, I. Soerjomataram, *eClinicalMedicine* **2022**, *47*, 101404.

[5] R. J. Huang, J. H. Hwang, *Gastrointestinal Endoscopy Clinics of North America* **2021**, *31*, 503.

[6] B. Gantuya, K. Oyuntsetseg, D. Bolor, Y. Erdene-Ochir, R. Sanduijav, D. Davaadorj, T. Tserentogtokh, T. Uchida, Y. Yamaoka, *Gastric Cancer* **2019**, *22*, 104.

[7] M. Nishitani, N. Yoshida, S. Tsuji, T. Masunaga, H. Hirai, S. Miyajima, A. Dejima, T. Nakashima, S. Wakita, K. Takemura, H. Minato, S. Kaneko, H. Doyama, *Endosc Int Open* **2019**, *07*, E1683.

[8] Á. Vincze, *Front. Surg.* **2023**, *10*, 1122454.

[9] H. Horiuchi, M. Kaise, H. Inomata, Y. Yoshida, M. Kato, H. Toyoizumi, K. Goda, H. Arakawa, M. Ikegami, R. Kushima, H. Tajiri, *Scandinavian Journal of Gastroenterology* **2013**, *48*, 626.

[10] Y. Horiuchi, J. Fujisaki, N. Yamamoto, T. Shimizu, M. Omae, A. Ishiyama, T. Yoshio, T. Hirasawa, Y. Yamamoto, T. Tsuchida, M. Igarashi, H. Takahashi, *Surg Endosc* **2017**, *31*, 1906.

[11] Y. Horiuchi, J. Fujisaki, N. Yamamoto, S. Yoshimizu, A. Ishiyama, T. Yoshio, T. Hirasawa, Y. Yamamoto, M. Nagahama, H. Takahashi, T. Tsuchida, *Gastric Cancer* **2018**, *21*, 988.

[12] Y. Horiuchi, Y. Tokai, N. Yamamoto, S. Yoshimizu, A. Ishiyama, T. Yoshio, T. Hirasawa, Y. Yamamoto, M. Nagahama, H. Takahashi, T. Tsuchida, J. Fujisaki, *Dig Dis Sci* **2020**, *65*, 591.

[13] Y. Horiuchi, K. Aoyama, Y. Tokai, T. Hirasawa, S. Yoshimizu, A. Ishiyama, T. Yoshio, T. Tsuchida, J. Fujisaki, T. Tada, *Dig Dis Sci* **2020**, *65*, 1355.

[14] Y. Horiuchi, T. Hirasawa, N. Ishizuka, Y. Tokai, K. Namikawa, S. Yoshimizu, A. Ishiyama, T. Yoshio, T. Tsuchida, J. Fujisaki, T. Tada, *Gastrointestinal Endoscopy* **2020**, *92*, 856.

[15] Y. Horiuchi, T. Hirasawa, N. Ishizuka, H. Hatamori, Y. Ikenoyama, J. Tokura, M. Ishioka, Y. Tokai, K. Namikawa, S. Yoshimizu, A. Ishiyama, T. Yoshio, T. Tsuchida, J. Fujisaki, *Gastric Cancer* **2021**, *24*, 417.

[16] H. Jiang, H.-M. Tu, Q. Qiao, K.-B. Xu, J. Li, X.-W. Qi, X.-S. Ge, *Asian Pacific Journal of Cancer Prevention* **2014**, *15*, 8917.

[17] H. Ikehara, H. Doyama, H. Nakanishi, W. Hatta, T. Gotoda, H. Ishikawa, K. Yao, *Gastrointestinal Endoscopy* **2019**, *90*, 440.

[18] H. Hu, L. Gong, D. Dong, L. Zhu, M. Wang, J. He, L. Shu, Y. Cai, S. Cai, W. Su, Y. Zhong, C. Li, Y. Zhu, M. Fang, L. Zhong, X. Yang, P. Zhou, J. Tian, *Gastrointestinal Endoscopy* **2021**, *93*, 1333.

[19] Y. Yoshifuku, Y. Sanomura, S. Oka, K. Kuroki, M. Kurihara, T. Mizumoto, Y. Urabe, T. Hiyama, S. Tanaka, K. Chayama, *Gastroenterology Research and Practice* **2017**, *2017*, 1.

[20] O. Dohi, N. Yagi, A. Majima, Y. Horii, T. Kitaichi, Y. Onozawa, K. Suzuki, A. Tomie, R. Kimura-Tsuchiya, T. Tsuji, N. Yamada, N. Bito, T. Okayama, N. Yoshida, K. Kamada, K. Katada, K. Uchiyama, T. Ishikawa, T. Takagi, O. Handa, H. Konishi, Y. Naito, A. Yanagisawa, Y. Itoh, *Gastric Cancer* **2017**, *20*, 297.

[21] O. Dohi, N. Yagi, Y. Naito, A. Fukui, Y. Gen, N. Iwai, T. Ueda, N. Yoshida, K. Kamada, K. Uchiyama, T. Takagi, H. Konishi, A. Yanagisawa, Y. Itoh, *Gastrointestinal Endoscopy* **2019**, *89*, 47.

[22] Z. Yang, S. Lei, Department of Gastroenterology, Renmin Hospital of Wuhan University, Wuhan, China, *Turk J Gastroenterol* **2019**, *30*, 549.

[23] H. Takahashi, Y. Miura, H. Osawa, T. Takezawa, Y. Ino, M. Okada, A. K. Lefor, H. Yamamoto, *Clin Endosc* **2019**, *52*, 273.

[24] T. Nakano, O. Dohi, Y. Naito, K. Terasaki, N. Iwai, T. Ueda, A. Majima, Y. Horii, Y. Yasuda-Onozawa, T. Kitaichi, R. Hirose, K. Inoue, N. Yoshida, K. Kamada, K. Uchiyama, O. Handa, T. Ishikawa, T. Takagi, H. Konishi, M. Kishimoto, Y. Itoh, *Dig Dis* **2021**, *39*, 156.

[25] K. Yao, T. Nagahama, T. Matsui, A. Iwashita, *Digestive Endoscopy* **2013**, *25*, 44.

[26] S. Fujiwara, K. Yao, T. Nagahama, K. Uchita, T. Kanemitsu, K. Tsurumi, N. Takatsu, T. Hisabe, H. Tanabe, A. Iwashita, T. Matsui, *Gastric Cancer* **2015**, *18*, 590.

[27] I. Asada-Hirayama, S. Kodashima, Y. Sakaguchi, S. Ono, K. Niimi, S. Mochizuki, Y. Tsuji, C. Minatsuki, S. Shichijo, K. Matsuzaka, T. Ushiku, M. Fukayama, N. Yamamichi, M. Fujishiro, K. Koike, *Endosc Int Open* **2016**, *04*, E690.

[28] T. Nagahama, K. Yao, N. Uedo, H. Doyama, T. Ueo, K. Uchita, H. Ishikawa, T. Kanesaka, Y. Takeda, K. Wada, K. Imamura, H. Arima, T. Shimokawa, *Endoscopy* **2018**, *50*, 566.

[29] N. Tamura, Y. Sakaguchi, W. Furutani, M. Matsui, S. Nagao, N. Sakuma, K. Fukagawa, Y. Miura, H. Mizutani, D. Ohki, Y. Kataoka, I. Saito, M. Ono, C. Minatsuki, Y. Tsuji, S. Ono, S. Kodashima, H. Abe, T. Ushiku, N. Yamamichi, K. Koike, M. Fujishiro, *Sci Rep* **2022**, *12*, 8349.

[30] L. Li, Y. Chen, Z. Shen, X. Zhang, J. Sang, Y. Ding, X. Yang, J. Li, M. Chen, C. Jin, C. Chen, C. Yu, *Gastric Cancer* **2020**, *23*, 126.

[31] H. Ueyama, Y. Kato, Y. Akazawa, N. Yatagai, H. Komori, T. Takeda, K. Matsumoto, K. Ueda, K. Matsumoto, M. Hojo, T. Yao, A. Nagahara, T. Tada, *Journal of Gastroenterology and Hepatology (Australia)* **2021**, *36*, 482.

[32] L. Wu, J. Wang, X. He, Y. Zhu, X. Jiang, Y. Chen, Y. Wang, L. Huang, R. Shang, Z. Dong, B. Chen, X. Tao, Q. Wu, H. Yu, *Gastrointestinal Endoscopy* **2022**, *95*, 92.

[33] X. He, L. Wu, Z. Dong, D. Gong, X. Jiang, H. Zhang, Y. Ai, Q. Tong, P. Lv, B. Lu, Q. Wu, J. Yuan, M. Xu, H. Yu, *Gastrointestinal Endoscopy* **2022**, *95*, 671.

[34] D. Tang, M. Ni, C. Zheng, X. Ding, N. Zhang, T. Yang, Q. Zhan, Y. Fu, W. Liu, D. Zhuang, Y. Lv, G. Xu, L. Wang, X. Zou, *Surgical Endoscopy* **2022**, *36*, 7800.

[35] J. Jin, Q. Zhang, B. Dong, T. Ma, X. Mei, X. Wang, S. Song, J. Peng, A. Wu, L. Dong, D. Kong, *Front. Oncol.* **2022**, *12*, 927868.

[36] L. Wang, Y. Yang, A. Yang, T. Li, *Biomed. Opt. Express* **2023**, *14*, 4677.

[37] T. Matsuoka, M. Yashiro, *World journal of gastroenterology* **2018**, *24*, 2818.

[38] W. Jelski, B. Mroczko, *International journal of molecular sciences* **2022**, *23*, 7588.

[39] R. Matthews, M. Choi, *Diagnostics* **2016**, *6*, 35.

[40] F. Chen, Y.-C. Ni, K.-E. Zheng, S.-H. Ju, J. Sun, X.-L. Ou, M.-H. Xu, H. Zhang, G. Marchal, *World Journal of Gastroenterology* **2003**, *9*, 1404.

[41] A. Malaj, F. Bilaj, A. Shahini, M. Miraka, *Contemporary Oncology/Współczesna Onkologia* **2017**, *21*, 168.

[42] H. Shi, T. Li, Z. Liu, J. Zhao, F. Qi, *Front. Bioeng. Biotechnol.* **2022**, *10*, 1052069.

[43] A. H. Wani, A. H. Parry, I. Feroz, N. A. Choh, *J Gastrointest Canc* **2021**, *52*, 606.

[44] A. Orăşeanu, M. C. Brisc, O. A. Maghiar, H. Popa, C. M. Brisc, S. F. Șolea, T. A. Maghiar, C. Brisc, *Diagnostics* **2023**, *13*, 3608.

[45] A. S. Borggreve, L. Goense, H. J. Brenkman, S. Mook, G. J. Meijer, F. J. Wessels, M. Verheij, E. P. Jansen, R. Van Hillegersberg, P. S. Van Rossum, others, *The British journal of radiology* **2019**, *92*, 20181044.

[46] X. Li, N.-R. Zheng, L.-H. Wang, Z.-W. Li, Z.-C. Liu, H. Fan, Y. Wang, J. Dai, X.-T. Ni, X. Wei, M.-W. Liu, K. Li, Z.-X. Li, T. Zhou, Y. Zhang, J.-Y. Zhang, G. Kadeerhan, S. Huang, W.-H. Wu, W.-D. Liu, X.-Z. Wu, L.-F. Zhang, J.-M. Xu, M. Gerhard, W.-C. You, K.-F. Pan, W.-Q. Li, J. Qin, *eBioMedicine* **2021**, *74*, 103714.

[47] M. Rostami-Nejad, M. Rezaei-Tavirani, V. Mansouri, Z. Akbari, S. Abdi, *Gastroenterol Hepatol Bed Bench* **2019**, *12*, S1.

[48] Y. Song, J. Wang, J. Sun, X. Chen, J. Shi, Z. Wu, D. Yu, F. Zhang, Z. Wang, *Genomics, Proteomics & Bioinformatics* **2020**, *18*, 679.

[49] S. Ge, X. Xia, C. Ding, B. Zhen, Q. Zhou, J. Feng, J. Yuan, R. Chen, Y. Li, Z. Ge, J. Ji, L. Zhang, J. Wang, Z. Li, Y. Lai, Y. Hu, Y. Li, Y. Li, J. Gao, L. Chen, J. Xu, C. Zhang, S. Y. Jung, J. M. Choi, A. Jain, M. Liu, L. Song, W. Liu, G. Guo, T. Gong, Y. Huang, Y. Qiu, W. Huang, T. Shi, W. Zhu, Y. Wang, F. He, L. Shen, J. Qin, *Nat Commun* **2018**, *9*, 1012.

[50] O. Repetto, R. Vettori, A. Steffan, R. Cannizzaro, V. De Re, *International Journal of Molecular Sciences* **2023**, *24*, 16931.

[51] B. J. Vakoc, D. Fukumura, R. K. Jain, B. E. Bouma, *Nat Rev Cancer* **2012**, *12*, 363.

[52] S. Coda, P. Siersema, G. Stamp, A. Thillainayagam, *Endosc Int Open* **2015**, *03*, E380.

[53] Q.-S. Wan, T. Wang, K.-H. Zhang, *Tumour Biol.* **2017**, *39*, 101042831771798.

[54] K. Liu, Q. Zhao, B. Li, X. Zhao, *Front. Bioeng. Biotechnol.* **2022**, *10*, 856591.

[55] P. Pal, A. P. Singh, N. D. Kanuri, R. Banerjee, *Transl Gastroenterol Hepatol* **2022**, *7*, 6.

[56] J.-H. Cho, S. R. Jeon, S.-Y. Jin, *World Journal of Clinical Cases* **2020**, *8*, 2902.

[57] J. Zhu, W. Li, J. Zhou, Y. Chen, C. Zhao, T. Zhang, W. Peng, X. Wang, *Clinics* **2017**, *72*, 438.

[58] A. Lamb, L. Chen, *J of Cellular Biochemistry* **2013**, *114*, 491.

[59] T. Kanesaka, N. Uedo, H. Doyama, N. Yoshida, T. Nagahama, K. Ohtsu, K. Uchita, K. Kojima, T. Ueo, H. Takahashi, H. Ueyama, Y. Akazawa, T. Shimokawa, K. Yao, *DEN Open* **2022**, *2*, e61.

[60] Y. Kim, H. Kim, M. Jung, S. Y. Rha, H. C. Chung, S. K. Lee, *Cancers* **2022**, *14*, 4319.

[61] Y.-W. Zhou, L.-Y. Zhang, S.-N. Ding, A.-L. Zhang, Y. Zhu, Y.-X. Chen, Q.-C. Zhang, L.-T. Sun, J.-R. Yu, *American Journal of Translational Research* **2022**, *14*, 55.

[62] W. Han, R. Kong, N. Wang, W. Bao, X. Mao, J. Lu, *Cancers* **2023**, *15*, 776.

[63] S. Tian, H. Huang, Y. Zhang, H. Shi, Y. Dong, W. Zhang, C. Bai, *Eur Respir Rev* **2023**, *32*, 220185.

[64] A. Fugazza, F. Gaiani, M. C. Carra, F. Brunetti, M. Lévy, I. Sobhani, D. Azoulay, F. Catena, G. L. de'Angelis, N. de'Angelis, *BioMed Research International* **2016**, *2016*, 1.

[65] K. K. Wang, D. L. Carr-Locke, S. K. Singh, H. Neumann, H. Bertani, J.-P. Galmiche, R. I. Arsenescu, F. Caillol, K. J. Chang, S. Chaussade, E. Coron, G. Costamagna, A. Dlugosz, S. Ian Gan, M. Giovannini, F. G. Gress, O. Haluszka, K. Y. Ho, M. Kahaleh, V. J. Konda, F. Prat, R. J. Shah, P. Sharma, A. Slivka, H. C. Wolfsen, A. Zfass, *United European gastroenterology journal* **2015**, *3*, 230.

[66] C. H. Park, H. Kim, J. H. Jo, K. Y. Hahn, J. Yoon, S. Y. Kim, Y. C. Lee, S. H. Noh, H. C. Chung, S. K. Lee, *J of Gastro and Hepatol* **2019**, *34*, 84.

[67] A. Capuano, E. Andreuzzi, E. Pivetta, R. Doliana, A. Favero, V. Canzonieri, S. Maiero, M. Fornasarig, R. Magris, R. Cannizzaro, M. Mongiat, P. Spessotto, *Front. Oncol.* **2019**, *9*, 513.

[68] M. Fornasarig, A. Capuano, S. Maiero, E. Pivetta, G. Guarnieri, V. Canzonieri, A. Zucchetto, M. Mongiat, R. Cannizzaro, P. Spessotto, *Sci Rep* **2021**, *11*, 21053.

[69] S. Gong, H.-B. Xue, Z.-Z. Ge, J. Dai, X.-B. Li, Y.-J. Zhao, Y. Zhang, Y.-J. Gao, Y. Song, *Medicine* **2015**, *94*, e1930.

[70] P. Spessotto, M. Fornasarig, E. Pivetta, S. Maiero, R. Magris, M. Mongiat, V. Canzonieri, P. De Paoli, A. De Paoli, A. Buonadonna, D. Serraino, C. Panato, C. Belluco, R. Cannizzaro, *Sci Rep* **2017**, *7*, 9819.

[71] G. H. Bok, S. R. Jeon, J. Y. Cho, J.-H. Cho, W. C. Lee, S. Y. Jin, I. H. Choi, H. G. Kim, T. H. Lee, E. J. Park, *Gastrointestinal Endoscopy* **2013**, *77*, 899.

[72] A. Canakis, S. S. Deliwala, J. Kadiyala, S. Bomman, J. Canakis, M. Bilal, *Annals of gastroenterology* **2022**, *35*, 496.

[73] J. Vaculová, R. Kroupa, Z. Kala, J. Dolina, T. Grolich, J. Vlažný, D. Said, L. Izakovičová Hollá, P. Bořilová Linhartová, V. Procházka, M. Joukal, P. Jabandžiev, O. Slabý, L. Kunovský, *Diagnostics* **2022**, *12*, 1616.

[74] J. Langer, D. Jimenez de Aberasturi, J. Aizpurua, R. A. Alvarez-Puebla, B. Auguié, J. J. Baumberg, G. C. Bazan, S. E. J. Bell, A. Boisen, A. G. Brolo, J. Choo, D. Cialla-May, V. Deckert, L. Fabris, K. Faulds, F. J. García de Abajo, R. Goodacre, D. Graham, A. J. Haes, C. L. Haynes, C. Huck, T. Itoh, M. Käll, J. Kneipp, N. A. Kotov, H. Kuang, E. C. Le Ru, H. K. Lee, J.-F. Li, X. Y. Ling, S. A. Maier, T. Mayerhöfer, M. Moskovits, K. Murakoshi, J.-M. Nam, S. Nie, Y. Ozaki, I. Pastoriza-Santos, J. Perez-Juste, J. Popp, A. Pucci, S. Reich, B. Ren, G. C. Schatz, T. Shegai, S. Schlücker, L.-L. Tay, K. G. Thomas, Z.-Q. Tian, R. P. Van Duyne, T. Vo-Dinh, Y. Wang, K. A. Willets, C. Xu, H. Xu, Y. Xu, Y. S. Yamamoto, B. Zhao, L. M. Liz-Marzán, *ACS Nano* **2020**, *14*, 28.

[75] H. P. S. Heng, C. Shu, W. Zheng, K. Lin, Z. Huang, *Transl Biophotonics* **2021**, *3*, e202000018.

[76] M. S. Bergholt, W. Zheng, K. Lin, J. Wang, H. Xu, J. Ren, K. Y. Ho, M. Teh, K. G. Yeoh, Z. Huang, *Anal. Chem.* **2015**, *87*, 960.

[77] M. S. Bergholt, K. Lin, J. Wang, W. Zheng, H. Xu, Q. Huang, J. Ren, K. Y. Ho, M. Teh, S. Srivastava, B. Wong, K. G. Yeoh, Z. Huang, *Journal of Biophotonics* **2016**, *9*, 333.

[78] M. S. Bergholt, W. Zheng, K. Lin, K. Y. Ho, M. Teh, K. G. Yeoh, J. B. Y. So, Z. Huang, *Technol Cancer Res Treat* **2011**, *10*, 103.

[79] M. S. Bergholt, W. Zheng, K. Y. Ho, M. Teh, K. G. Yeoh, J. B. Yan So, A. Shabbir, Z. Huang, *Gastroenterology* **2014**, *146*, 27.

[80] M. S. Bergholt, W. Zheng, K. Y. Ho, K. G. Yeoh, M. Teh, J. B. Y. So, Z. Huang, in *Optical Fibers and Sensors for Medical Diagnostics and Treatment Applications XIII*, SPIE, **2013**, pp. 64–69.

[81] L. Qiu, D. K. Pleskow, R. Chuttani, E. Vitkin, J. Leyden, N. Ozden, S. Itani, L. Guo, A. Sacks, J. D. Goldsmith, M. D. Modell, E. B. Hanlon, I. Itzkan, L. T. Perelman, *Nat Med* **2010**, *16*, 603.

[82] M. S. Bergholt, W. Zheng, K. Y. Ho, M. Teh, K. G. Yeoh, J. B. Y. So, A. Shabbir, Z. Huang, *Journal of Biophotonics* **2013**, *6*, 49.

[83] J. Wang, K. Lin, W. Zheng, K. Y. Ho, M. Teh, K. G. Yeoh, Z. Huang, *Anal Bioanal Chem* **2015**, *407*, 8303.

[84] S. Duraipandian, M. Sylvest Bergholt, W. Zheng, K. Yu Ho, M. Teh, K. Guan Yeoh, J. Bok Yan So, A. Shabbir, Z. Huang, *J. Biomed. Opt.* **2012**, *17*, 1.

[85] Z. Huang, M. S. Bergholt, W. Zheng, K. Y. Ho, K. G. Yeoh, M. Teh, J. B. Y. So, A. Shabbir, in *Optical Biopsy XI*, SPIE, **2013**, pp. 68–73.

[86] M. Li, H. He, G. Huang, B. Lin, H. Tian, K. Xia, C. Yuan, X. Zhan, Y. Zhang, W. Fu, *Front. Oncol.* **2021**, *11*, 665176.

[87] S. Luo, C. Chen, H. Mao, S. Jin, *J. Biomed. Opt* **2013**, *18*, 067004.

[88] M. S. Bergholt, W. Zheng, K. Y. Ho, K. G. Yeoh, M. Teh, J. B. Y. So, Z. Huang, in *Biomedical Vibrational Spectroscopy VI: Advances in Research and Industry*, SPIE, **2014**, pp. 108–112.

[89] J. Wang, K. Lin, W. Zheng, K. Y. Ho, M. Teh, K. G. Yeoh, Z. Huang, *Faraday Discuss.* **2016**, *187*, 377.

[90] K. Lin, J. Wang, W. Zheng, K. Y. Ho, M. Teh, K. G. Yeoh, Z. Huang, *Cancer Prevention Research* **2016**, *9*, 476.

[91] G. R. Fonda, *Electr. Eng.* **1938**, *57*, 677.

[92] M. Loshchenov, V. Levkin, N. Kalyagina, K. Linkov, S. Kharnas, K. Efendiev, P. Kharnas, V. Loschenov, *Lasers Med Sci* **2020**, *35*, 1721.

[93] L. Angelova, E. Borisova, A. Zhelyazkova, M. Keremedchiev, B. Vladimirov, L. Avramov, in *Biophotonics—Riga 2013*, SPIE, **2013**, pp. 42–52.

[94] H. Isomoto, A. Nanashima, T. Senoo, K. Ogiwara, M. Hashisako, K. Ohnita, N. Yamaguchi, M. Kunizaki, S. Hidaka, H. Fukuda, H. Ishii, K. Matsushima, H. Minami, Y. Akazawa, F. Takeshima, J. Fukuoka, T. Nagayasu, K. Nakao, *Photodiagnosis and Photodynamic Therapy* **2015**, *12*, 201.

[95] F. Cianchi, G. Indennitate, B. Paoli, M. Ortolani, G. Lami, N. Manetti, O. Tarantino, S. Messeri, C. Foppa, B. Badii, L. Novelli, I. Skalamera, T. Nelli, F. Coratti, G. Perigli, F. Staderini, *J Gastrointest Surg* **2020**, *24*, 2197.

[96] G. L. Baiocchi, S. Molfino, B. Molteni, L. Quarti, G. Arcangeli, S. Manenti, L. Arru, M. Botticini, F. Gheza, *Updates Surg* **2020**, *72*, 761.

[97] Z. Luan, Y. Qin, J. Dai, H. Wu, Y. Chen, X. Feng, G. Peng, *Gastroenterology Research and Practice* **2020**, *2020*, 1.

[98] X. Zhou, J. Dai, Y. Chen, G. Duan, Y. Liu, H. Zhang, H. Wu, G. Peng, *J. Biomed. Opt* **2016**, *21*, 105002.

[99] H. Ikeda, H. Ito, M. Hikita, N. Yamaguchi, N. Uragami, N. Yokoyama, Y. Hirota, M. Kushima, Y. Ajioka, H. Inoue, *WJGO* **2018**, *10*, 439.

[100] Y. Chen, J. Dai, X. Zhou, Y. Liu, W. Zhang, G. Peng, *PLoS ONE* **2014**, *9*, e93906.

[101] Z. Guleken, P. Jakubczyk, W. Paja, K. Pancerz, A. Wosiak, İ. Yaylım, G. İnal Gültekin, N. Tarhan, M. T. Hakan, D. Sönmez, D. Sarıbal, S. Arıkan, J. Depciuch, *Computer Methods and Programs in Biomedicine* **2023**, *234*, 107523.

[102] H. Cao, L. Zhu, L. Li, W. Wang, X. Niu, *Clinical and experimental medicine* **2023**, *23*, 2433.

[103] F. Feng, Y. Tian, G. Xu, Z. Liu, S. Liu, G. Zheng, M. Guo, X. Lian, D. Fan, H. Zhang, *BMC Cancer* **2017**, *17*, 737.

[104] H. Zhou, A. Dong, H. Xia, G. He, J. Cui, *Oncology Letters* **2018**, *16*, 1079.

[105] M. Bahreini, A. Hosseinzadegan, A. Rashidi, S. R. Miri, H. R. Mirzaei, P. Hajian, *Talanta* **2019**, *204*, 826.

[106] C. Li, S. Liu, Q. Zhang, D. Wan, R. Shen, Z. Wang, Y. Li, B. Hu, *Spectrochimica Acta Part A: Molecular and Biomolecular Spectroscopy* **2023**, *287*, 122049.

[107] K. Liu, B. Liu, Y. Zhang, Q. Wu, M. Zhong, L. Shang, Y. Wang, P. Liang, W. Wang, Q. Zhao, B. Li, *Computational and Structural Biotechnology Journal* **2023**, *21*, 802.

[108] W. Wang, B. Shi, C. He, S. Wu, L. Zhu, J. Jiang, L. Wang, L. Lin, J. Ye, H. Zhang, *Spectrochimica Acta Part A: Molecular and Biomolecular Spectroscopy* **2023**, *288*, 122163.

[109] Z. Liu, W. Su, J. Ao, M. Wang, Q. Jiang, J. He, H. Gao, S. Lei, J. Nie, X. Yan, X. Guo, P. Zhou, H. Hu, M. Ji, *Nat Commun* **2022**, *13*, 4050.

[110] Á. Fernández-Galiana, O. Bibikova, S. Vilms Pedersen, M. M. Stevens, *Advanced Materials* **2023**, 2210807.

[111] X. Li, T. Yang, S. Li, D. Wang, Y. Song, K. Yu, *J Raman Spectroscopy* **2016**, *47*, 917.

[112] H. Ma, X. Tang, Y. Liu, X. X. Han, C. He, H. Lu, B. Zhao, *Anal. Chem.* **2019**, *91*, 8767.

[113] T. Gong, C. M. Das, M.-J. Yin, T.-R. Lv, N. M. Singh, A. M. Soehartono, G. Singh, Q.-F. An, K.-T. Yong, *Coordination Chemistry Reviews* **2022**, *470*, 214711.

[114] G. C. Phan-Quang, X. Han, C. S. L. Koh, H. Y. F. Sim, C. L. Lay, S. X. Leong, Y. H. Lee, N. Pazos-Perez, R. A. Alvarez-Puebla, X. Y. Ling, *Acc. Chem. Res.* **2019**, *52*, 1844.

[115] A. Zhang, J. Chang, Y. Chen, Z. Huang, G. Alfranca, Q. Zhang, D. Cui, *Anal. Methods* **2019**, *11*, 5089.

[116] Y. Lu, B. Lei, Q. Zhao, X. Yang, Y. Wei, T. Xiao, S. Zhu, Y. Ouyang, H. Zhang, W. Cai, *ACS Omega* **2023**, *8*, 29836.

[117] Y. Wei, Y. Zhu, M. Wang, *Optik* **2016**, *127*, 7902.

[118] J. Chang, A. Zhang, Z. Huang, Y. Chen, Q. Zhang, D. Cui, *Talanta* **2019**, *198*, 45.

[119] M. Chen, S. Yao, Y. Yang, F. Jiang, Y. Yang, Y. Gu, Z. Wang, X. Cao, W. Wei, *Microchemical Journal* **2023**, *193*, 109106.

[120] X. Hou, M. Zhang, H. Qiao, *International journal of clinical and experimental pathology* **2015**, *8*, 13096.

[121] F. Macedo, K. Ladeira, A. Longatto-Filho, S. F. Martins, *J Gastric Cancer* **2017**, *17*, 1.

[122] X. Zhao, Z. Yu, K. Zang, *Journal of Oncology* **2022**, *2022*, 1.

[123] Y. Huang, Z. Liu, X. Qin, J. Liu, Y. Yang, W. Wei, *Analyst* **2023**, *148*, 3295.

[124] H. Pan, Y. Dong, L. Gong, J. Zhai, C. Song, Z. Ge, Y. Su, D. Zhu, J. Chao, S. Su, L. Wang, Y. Wan, C. Fan, *Biosensors and Bioelectronics* **2022**, *215*, 114553.

[125] S. Ge, M. Ran, Y. Mao, Y. Sun, X. Zhou, L. Li, X. Cao, *Analyst* **2021**, *146*, 5326.

[126] J. Zhang, C. Song, Y. Zhu, H. Gan, X. Fang, Q. Peng, J. Xiong, C. Dong, C. Han, L. Wang, *Biosensors and Bioelectronics* **2023**, *219*, 114836.

[127] D. Huang, X. Li, B. Shen, J. Li, X. Ding, X. Zhou, B. Guo, W. Cheng, S. Ding, *Sensors and Actuators B: Chemical* **2018**, *273*, 393.

[128] J. Jiao, C. Duan, L. Xue, Y. Liu, W. Sun, Y. Xiang, *Biosensors and Bioelectronics* **2020**, *167*, 112479.

[129] X. Cheng, Y. Yan, X. Chen, J. Duan, D. Zhang, T. Yang, X. Gou, M. Zhao, S. Ding, W. Cheng, *Sensors and Actuators B: Chemical* **2021**, *331*, 129458.

[130] Y. Gao, Y. Chen, J. Shang, S. Yu, S. He, R. Cui, F. Wang, *ACS Applied Materials & Interfaces* **2022**, *14*, 5080.

[131] Z. Wang, W. Li, Z. Gong, P. Sun, T. Zhou, X. Cao, *New J. Chem.* **2019**, *43*, 1733.

[132] A. Li, S. Dubey, M. L. Varney, B. J. Dave, R. K. Singh, *The Journal of Immunology* **2003**, *170*, 3369.

[133] D. Buschmann, B. Kirchner, S. Hermann, M. Märte, C. Wurmser, F. Brandes, S. Kotschote, M. Bonin, O. K. Steinlein, M. W. Pfaffl, *Journal of extracellular vesicles* **2018**, *7*, 1481321.

[134] R. Crescitelli, C. Lässer, J. Lötvall, *Nature Protocols* **2021**, *16*, 1548.

[135] E. Willms, C. Cabañas, I. Mäger, M. J. A. Wood, P. Vader, *Frontiers in immunology* **2018**, *9*, 738.

[136] G. Huang, G. Lin, Y. Zhu, W. Duan, D. Jin, *Lab on a Chip* **2020**, *20*, 2423.

[137] S. Thietart, P.-E. Rautou, *Journal of hepatology* **2020**, *73*, 1507.

[138] Z. Liu, T. Li, Z. Wang, J. Liu, S. Huang, B. H. Min, J. Y. An, K. M. Kim, S. Kim, Y. Chen, H. Liu, Y. Kim, D. T. W. Wong, T. J. Huang, Y.-H. Xie, *ACS Appl. Nano Mater.* **2022**, *5*, 12506.

[139] L. Guo, Y. Li, F. Huang, J. Dong, F. Li, X. Yang, S. Zhu, M. Yang, *J. Innov. Opt. Health Sci.* **2019**, *12*, 1950003.

[140] J. Lin, J. Wang, C. Xu, Y. Zeng, Y. Chen, L. Li, Z. Huang, B. Li, R. Chen, *J Raman Spectroscopy* **2017**, *48*, 16.

[141] X. Lin, Q. Wu, J. Lin, X. Liu, X. Jia, M. Peng, D. Lin, S. Qiu, S. Feng, *J Raman Spectroscopy* **2020**, *51*, 2245.

[142] Y. Chen, Y. Zhang, F. Pan, J. Liu, K. Wang, C. Zhang, S. Cheng, L. Lu, W. Zhang, Z. Zhang, X. Zhi, Q. Zhang, G. Alfranca, J. M. de la Fuente, D. Chen, D. Cui, *ACS Nano* **2016**, *10*, 8169.

[143] L. Huang, Y. Zhu, C. Xu, Y. Cai, Y. Yi, K. Li, X. Ren, D. Jiang, Y. Ge, X. Liu, W. Sun, Q. Zhang, Y. Wang, *ACS Sensors* **2022**, *7*, 1439.

[144] Y. Chen, S. Cheng, A. Zhang, J. Song, J. Chang, K. Wang, GuoGao, Y. Zhang, S. Li, H. Liu, G. Alfranca, M. A. Aslam, B. Chu, C. Wang, F. Pan, L. Ma, J. M. De La Fuente, J. Ni, D. Cui, *j biomed nanotechnol* **2018**, *14*, 1773.

[145] M. A. Aslam, C. Xue, M. Liu, K. Wang, D. Cui, *Engineering Letters* **2021**, *29*.

[146] N. Abidi, in *FTIR Microspectroscopy*, Springer International Publishing, Cham, **2021**, pp. 1–12.

[147] F. Faghihzadeh, N. M. Anaya, L. A. Schifman, V. Oyanedel-Craver, *Nanotechnol. Environ. Eng.* **2016**, *1*, 1.

[148] A. Fadlelmoula, D. Pinho, V. H. Carvalho, S. O. Catarino, G. Minas, *Micromachines* **2022**, *13*, 187.

[149] P. D. Lewis, K. E. Lewis, R. Ghosal, S. Bayliss, A. J. Lloyd, J. Wills, R. Godfrey, P. Kloer, L. A. Mur, *BMC Cancer* **2010**, *10*, 640.

[150] H. Chen, X. Li, S. Zhang, H. Yang, Q. Gao, F. Zhou, *Photodiagnosis and Photodynamic Therapy* **2022**, *40*, 103177.

[151] L. Li, J. Wu, L. Yang, H. Wang, Y. Xu, K. Shen, *Cancer Management and Research* **2021**, 2389.

[152] H. Tiernan, B. Byrne, S. G. Kazarian, *Spectrochimica Acta Part A: Molecular and Biomolecular Spectroscopy* **2020**, *241*, 118636.

[153] J. Grdadolnik, *Acta Chim. Slov.* **2002**, *49(3)*, 631.

[154] G. Akin Geyik, B. Peker Cengiz, F. Tugrul, S. N. Karuk Elmas, I. Yilmaz, F. N. Arslan, *Spectrochimica Acta Part A: Molecular and Biomolecular Spectroscopy* **2022**, *267*, 120619.

[155] M.-C. Popescu, R. Constantinescu, S. S. Padureanu, *Journal of Molecular Structure* **2020**, *1214*, 128211.

[156] S. Guo, G. Wei, W. Chen, C. Lei, C. Xu, Y. Guan, T. Ji, F. Wang, H. Liu, *Biomolecules* **2022**, *12*, 1815.

[157] Z. Guleken, H. Bulut, G. İ. Gültekin, S. Arıkan, İ. Yaylım, M. T. Hakan, D. Sönmez, N. Tarhan, J. Depciuch, *Talanta* **2021**, *231*, 122353.

[158] M. G. K, S. Barzegari, P. Hajian, H. Zham, H. R. Mirzaei, F. H. Shirazi, *Journal of Molecular Structure* **2021**, *1229*, 129493.

[159] Q. Li, R. Zhao, S. Shi, W. Li, *Analytical Letters* **2019**, *52*, 1914.

[160] Q. Li, W. Wang, X. Ling, J. G. Wu, *BioMed Research International* **2013**, *2013*, 1.

[161] H. Ullah, M. Zafar, Z. Batool, A. Nazir, G. Gilanie, J. Rehman, *Lasers in Engineering* **2023**, *54*, 89.

[162] W. Yi, D. Cui, Z. Li, L. Wu, A. Shen, J. Hu, *Spectrochimica Acta Part A: Molecular and Biomolecular Spectroscopy* **2013**, *101*, 127.

[163] H. Liu, Q. Su, D. Sheng, W. Zheng, X. Wang, *Journal of Molecular Structure* **2017**, *1130*, 33.

[164] L. Dong, X. Duan, L. Bin, J. Wang, Q. Gao, X. Sun, Y. Xu, *Spectrochimica Acta Part A: Molecular and Biomolecular Spectroscopy* **2023**, *289*, 122209.

[165] K.-Y. Su, W.-L. Lee, *Cancers* **2020**, *12*, 115.

[166] L. L. De Boer, T. M. Bydlon, F. Van Duijnhoven, M.-J. T. F. D. Vranken Peeters, C. E. Loo, G. A. O. Winter-Warnars, J. Sanders, H. J. C. M. Sterenborg, B. H. W. Hendriks, T. J. M. Ruers, *J Transl Med* **2018**, *16*, 367.

[167] Y. Zhu, T. Fearn, G. Mackenzie, B. Clark, J. M. Dunn, I. J. Bigio, S. G. Bown, L. B. Lovat, *J Biomed Opt* **2009**, *14*, 044022.

[168] G. Zonios, L. T. Perelman, V. Backman, R. Manoharan, M. Fitzmaurice, J. Van Dam, M. S. Feld, *Appl. Opt.* **1999**, *38*, 6628.

[169] L. L. De Boer, T. M. Bydlon, F. Van Duijnhoven, M.-J. T. F. D. Vranken Peeters, C. E. Loo, G. A. O. Winter-Warnars, J. Sanders, H. J. C. M. Sterenborg, B. H. W. Hendriks, T. J. M. Ruers, *J Transl Med* **2018**, *16*, 367.

[170] E. J. M. Baltussen, P. Snaebjornsson, S. G. B. De Koning, H. J. C. M. Sterenborg, A. G. J. Aalbers, N. Kok, G. L. Beets, *J. Biomed. Opt* **2017**, *22*, 1.

[171] I. Gkouzionis, S. Nazarian, M. Kawka, A. Darzi, N. Patel, C. J. Peters, D. S. Elson, *Journal of Biomedical Optics* **2022**, *27*, 025001.

[172] S. Nazarian, I. Gkouzionis, M. Kawka, M. Jamroziak, J. Lloyd, A. Darzi, N. Patel, D. S. Elson, C. J. Peters, *JAMA surgery* **2022**, *157*, e223899.

[173] T. Yamashita, H. Kinoshita, T. Sakaguchi, H. Isomoto, *Ann Transl Med* **2020**, *8*, 178.

[174] N. Koizumi, Y. Harada, M. Beika, T. Minamikawa, Y. Yamaoka, P. Dai, Y. Murayama, A. Yanagisawa, E. Otsuji, H. Tanaka, T. Takamatsu, *European Journal of Surgical Oncology (EJSO)* **2016**, *42*, 1236.

[175] T. Minamikawa, H. Matsuo, Y. Kato, Y. Harada, E. Otsuji, A. Yanagisawa, H. Tanaka, T. Takamatsu, *Sci Rep* **2016**, *6*, 25530.

[176] I. M. Liliac, B. S. Ungureanu, C. Mărgăritescu, V. M. Sacerdoțianu, A. Săftoiu, L. Mogoantă, E. Moraru, D. Pirici, *Biomedicines* **2022**, *10*, 349.

[177] L. Wang, Y. Zhou, C. Liu, L. Zhou, Y. He, Y. Pu, T. A. Nguyen, R. R. Alfano, in *Optical Biopsy XIII: Toward Real-Time Spectroscopic Imaging and Diagnosis*, SPIE, **2015**, pp. 138–144.

[178] J. Kinoshita, S. Fushida, S. Harada, I. Makino, K. Nakamura, K. Oyama, H. Fujita, I. Ninomiya, T. Fujimura, M. Kayahara, T. Ohta, *Oncology letters* **2010**, *1 6*, 989.

[179] T. Wiggins, S. Kumar, S. Markar, S. Antonowicz, G. Hanna, *Cancer Epidemiology, Biomarkers & Prevention* **2014**, *24*, 32.

[180] V. Juvekar, C. S. Lim, D. J. Lee, D. H. Song, C.-K. Noh, H. Kang, S. J. Shin, H. M. Kim, *ACS Appl. Bio Mater.* **2021**, *4*, 2135.

[181] J. Wang, Q. Ma, W. Zheng, H. Liu, C. Yin, F. Wang, X. Chen, Q. Yuan, W. Tan, *ACS Nano* **2017**, *11*, 8185.

[182] S. Nagano, Y. Ushimaru, R. Kawabata, A. Kitagawa, N. Ohara, Y. Miyake, H. Tomihara, S. Maeda, S. Noura, A. Miyamoto, K. Nishikawa, *World J Surg Onc* **2023**, *21*, 82.

[183] D.-W. Kim, B. Jeong, I. Shin, U. Kang, Y. Lee, Y. S. Park, S.-H. Ahn, D. J. Park, H.-H. Kim, *Surg Endosc* **2019**, *33*, 1235.

[184] S. Inada, H. Nakanishi, M. Oda, K. Mori, A. Ito, J. Hasegawa, K. Misawa, S. Fuchi, *Micromachines* **2019**, *10*, 81.

[185] F. Liang, H. Zhang, Y. Qiu, Q. Xu, K. Jian, L. Jiang, F. Wang, X. Lu, *Technol Cancer Res Treat* **2020**, *19*, 153303382097919.

[186] L. Li, D. Kang, Z. Huang, Z. Zhan, C. Feng, Y. Zhou, H. Tu, S. Zhuo, J. Chen, *BMC Cancer* **2019**, *19*, 295.

[187] X. Wang, D. Zhang, X. Zhang, Y. Xing, J. Wu, X. Sui, X. Huang, G. Chang, L. Li, *Technol Cancer Res Treat* **2022**, *21*, 153303382211332.

[188] G. Wu, J. Wei, Z. Zheng, J. Ye, S. Zeng, *Laser Physics Letters* **2014**, *11*, 065602.

[189] J. Yan, Y. Zheng, X. Zheng, Z. Liu, W. Liu, D. Chen, X. Dong, K. Li, X. Liu, G. Chen, J. Lu, J. Chen, S. Zhuo, G. Li, *Sci Rep* **2016**, *6*, 31004.

[190] K. He, L. Zhao, X. Huang, Y. Ding, L. Liu, X. Wang, M. Wang, Y. Zhang, Z. Fan, *Lasers Med Sci* **2018**, *33*, 871.

[191] H. Li, X. Xia, T. Chen, X. Li, W. Zheng, in *Optics in Health Care and Biomedical Optics VIII* , SPIE, Beijing, China, **2018**, p. 64.

[192] X. Li, H. Li, X. He, T. Chen, X. Xia, C. Yang, W. Zheng, *Biomed. Opt. Express* **2018**, *9*, 453.

[193] Y. Li, X. Xie, X. Yang, L. Guo, Z. Liu, X. Zhao, Y. Luo, W. Jia, F. Huang, S. Zhu, Z. Chen, X. Chen, Z. Wei, W. Zhang, *Journal of Biophotonics* **2019**, *12*, e201800324.

[194] Y. Li, L. Deng, X. Yang, Z. Liu, X. Zhao, F. Huang, S. Zhu, X. Chen, Z. Chen, W. Zhang, *Biomed. Opt. Express* **2019**, *10*, 4999.

[195] J. Fujimoto, W. Drexler, in *Optical Coherence Tomography: Technology and Applications*, Springer, **2008**, pp. 1–45.

[196] J. F. Bille, Ed., *High Resolution Imaging in Microscopy and Ophthalmology: New Frontiers in Biomedical Optics*, Springer International Publishing, Cham, **2019**.

[197] J. G. Fujimoto, *Nat Biotechnol* **2003**, *21*, 1361.

[198] P. Gong, K. Y. Foo, D. D. Lakhiani, R. Zilkens, H. M. Ismail, C. Yeomans, B. F. Dessauvagie, B. Latham, C. M. Saunders, B. F. Kennedy, *Optics & Laser Technology* **2023**, *166*, 109467.

[199] P. Kuppler, P. Strenge, B. Lange, S. Spahr-Hess, W. Draxinger, C. Hagel, D. Theisen-Kunde, R. Brinkmann, R. Huber, V. Tronnier, M. M. Bonsanto, *Journal of Neurosurgery* **2024**, 1.

[200] K. Yasuda, *Gastrointestinal Endoscopy* **2002**, *56*, S68.

[201] M. Polkowski, J. Palucki, E. Wronska, A. Szawlowski, A. Nasierowska-Guttmejer, E. Butruk, *Endoscopy* **2004**, *36*, 617.

[202] S. Luo, H. Liu, H. Zhao, X. An, H. Xie, L. Huo, in *2017 Conference on Lasers and Electro-Optics Pacific Rim (CLEO-PR)*, IEEE, Singapore, **2017**, pp. 1–3.

[203] S. Luo, Y. Fan, W. Chang, H. Liao, H. Kang, L. Huo, *Laser Phys. Lett.* **2019**, *16*, 095602.

[204] S. Luo, Y. Ran, L. Liu, H. Huang, X. Tang, Y. Fan, *Lasers Med Sci* **2022**, *37*, 2727.

[205] C. Li, H. Wei, Y. Zhao, G. Wu, H. Gu, Z. Guo, H. Yang, Y. He, S. Xie, *Laser Phys.* **2018**, *28*, 075604.

[206] C. Photiou, M. Kassinopoulos, C. Pitris, *Photonics* **2023**, *10*, 51.

[207] T. W. Cronin, *Current Zoology* **2018**, *64*, 513.

[208] H. Jeon, M. Harvey, R. Cisek, E. Bennett, D. Tokarz, *Biomed. Opt. Express* **2023**, *14*, 5376.

[209] A. I. Baba, C. Câtoi, in *Comparative Oncology*, The Publishing House Of The Romanian Academy, **2007**.

[210] W. Wang, L. G. Lim, S. Srivastava, J. S. B. Yan, A. Shabbir, Q. Liu, *J. Biomed. Opt* **2014**, *19*, 046020.

[211] A. Tuniyazi, T. Mu, X. Jiang, X. Lang, Q. Li, H. Yu, F. Han, J. Ban, B. Qin, *Laser & Photonics Reviews* **2024**, *18*, 2400486.

[212] S. Ilyov, D. Ivanov, T. Genova, V. Mircheva, L. Zaharieva, B. Kolev, B. Vladimirov, H. Valkov, N. Mazumder, K. Sindhoora, O. Semyachkina-Glushkovskaya, L. Avramov, E. Borisova, in *Journal of Physics: Conference Series*, IOP Publishing Ltd, **2021**.

[213] M. Kim, H. R. Lee, R. Ossikovski, A. Malfait-Jobart, D. Lamarque, T. Novikova, *Journal of the European Optical Society-Rapid Publications* **2022**, *18*, 287.

[214] H. Jeon, M. Harvey, R. Cisek, E. Bennett, D. Tokarz, *Biomedical Optics Express* **2023**, *14*, 5376.

[215] G. Lu, B. Fei, *J. Biomed. Opt* **2014**, *19*, 010901.

[216] N. Liu, Y. Guo, H. Jiang, W. Yi, *J. Biomed. Opt.* **2020**, *25*, 1.

[217] M. Danciu, T. Alexa-Stratulat, C. Stefanescu, G. Dodi, B. I. Tamba, C. T. Mihai, G. D. Stanciu, A. Luca, I. A. Spiridon, L. B. Ungureanu, V. Ianole, I. Ciortescu, C. Mihai, G. Stefanescu, I. Chirilă, R. Ciobanu, V. L. Drug, *Materials* **2019**, *12*, 1519.

[218] Y. B. Ji, C. H. Park, H. Kim, S.-H. Kim, G. M. Lee, S. K. Noh, T.-I. Jeon, J.-H. Son, Y.-M. Huh, S. Haam, S. J. Oh, S. K. Lee, J.-S. Suh, *Biomed. Opt. Express* **2015**, *6*, 1398.

[219] R. Grigorev, A. Kuzikova, P. Demchenko, A. Senyuk, A. Svechkova, A. Khamid, A. Zakharenko, M. Khodzitskiy, *Materials* **2019**, *13*, 85.

[220] B. Lengenfelder, F. Mehari, M. Hohmann, M. Heinlein, E. Chelales, M. J. Waldner, F. Klämpfl, Z. Zalevsky, M. Schmidt, *Sci Rep* **2019**, *9*, 1057.

[221] H. Wu, H. Song, Y. Huang, Z. Li, S. Wu, X. Zhang, H. Li, *Chinese Phys. B* **2020**, *29*, 064205.

[222] H. Nguyen, J. Park, S. Kang, M. Kim, *Sensors* **2015**, *15*, 10481.

[223] H. Su, X. Li, L. Huang, J. Cao, M. Zhang, V. Vedarethinam, W. Di, Z. Hu, K. Qian, *Advanced Materials* **2021**, *33*, 2007978.

[224] Y. Zhang, G. Gao, H. Liu, H. Fu, J. Fan, K. Wang, Y. Chen, B. Li, C. Zhang, X. Zhi, L. He, D. Cui, *Theranostics* **2014**, *4*, 154.

[225] Z. Li, P. Wang, Z. Liang, D. Wang, Y. Nie, Q. Ma, *Anal. Chem.* **2023**, *95*, 9706.

[226] T. Kojima, K. Yao, K. Ohtsu, C. Kuan, H. Tanabe, K. Imamura, T. Kanemitsu, M. Miyaoka, T. Nagahama, T. Ueki, A. Iwashita, *Gastric Cancer* **2022**, *25*, 761.

[227] Y. Pan, P. Lu, L. Cheng, Z. Li, D. Liu, J. Zhao, Y. Wang, L. Fu, C. Sima, D. Liu, *Photoacoustics* **2023**, *34*, 100573.

[228] J. Zhou, J. V. Jokerst, *Photoacoustics* **2020**, *20*, 100211.

[229] F. Capasso, *Nanophotonics* **2018**, *7*, 953.

[230] K.-F. Lee, *AI Superpowers: China, Silicon Valley, and the New World Order*, Harper Business, **2018**.